Title

Mechano-Genomic Analysis to Identify Flow-Mediated Vascular Transducers: A Multi-Scale Approach

Author

Roustaei, Mehrdad

Publication Date

2023

UNIVERSITY OF CALIFORNIA

Los Angeles

Mechano-Genomic Analysis to Identify Flow-Mediated Vascular Transducers: A Multi-Scale Approach

A dissertation submitted in partial satisfaction of the
requirements for the degree Doctor of Philosophy
in Bioengineering

by

Mehrdad Roustaei

2023

ABSTRACT OF THE DISSERTATION

Mechano-Genomic Analysis to Identify Flow-Mediated Vascular Transducers: A Multi-Scale Approach

by

Mehrdad Roustaei
Doctor of Philosophy in Bioengineering
University of California, Los Angeles, 2023
Professor Tzung Hsiai, Chair

Hemodynamic forces contribute to mechanotransduction and metabolomic pathways underlying microvascular development, remodeling, and atherogenesis. In micro-scale and developmental stages, microvascular adaptation, and remodeling in response to injury is modulated by spatiotemporal variations in wall shear stress (WSS); however, the underlying mechanisms and interplay leading to adaptation of microcirculation and remodeling at embryonic stage remain elusive. The understanding of the interplay between low Reynolds number (stokes flow) hemodynamic variations and microvascular adaptation provides translational implications in microvascular injury and repair for human diseases with associated vascular complications, such as diabetes and peripheral artery disease. In macro-scale and adult stage, disturbed flow and low WSS promote atherosclerosis which is mitigated as a result of exercise by changing the local

hemodynamics and activating metabolomic transducers underlying vascular protection in the disturbed flow-prone vasculature. We used embryonic zebrafish tail as a microcirculation model and mouse aorta as a atherosclerosis model to investigate the role of flow-mediated microvascular remodeling and atherosclerosis development at different scales.

In micro-scale, using computational fluid dynamics, we elucidated the interplay between WSS and vascular remodeling in zebrafish model of tail amputation and regeneration. The transgenic *Tg* (*fli1:eGFP; Gata1:ds-red*) zebrafish line was used to track the 3-D fluorescently-labeled vascular endothelium for post-image segmentation and reconstruction of fluid domain. Micro-particle image velocimetry was used to validate the blood flow. Following amputation to the dorsal aorta (DA) and posterior cardinal vein (PCV), vasoconstriction developed in the dorsal longitudinal anastomotic vessel (DLAV) along with increased WSS in the proximal segmental vessels (SV) from amputation. Angiogenesis ensued at the tips of the amputated DLAV and PCV where WSS was minimal. At 2 days post amputation (dpa), vasodilation occurred in a pair of SVs proximal to amputation, followed by increased blood flow and WSS, whereas in the SVs distal to amputation, WSS normalized to the baseline. At 3 dpa, the increase in blood flow in the arterial SV proximal to amputation promoted anastomosis with DLAV to form a loop with PCV. Thus, our *in-silico* modeling revealed the interplay between WSS and micro-vascular adaptation to changes in WSS and blood flow to restore micro-circulation following tail amputation.

In macro-scale, we simulated exercise-augmented pulsatile shear stress (PSS) to mitigate flow recirculation in the lesser curvature of the aortic arch. Ultrasound-based 4-

D+time moving boundary computational fluid dynamics analysis was performed on mouse aorta to simulate blood flow over several cardiac cycles. Exercise modulated the time-averaged shear stress (TAWSS) and oscillatory shear index (OSI), and upregulated SCD1 and attenuated well-known VCAM1 expression in the disturbed flow-prone aortic arch in Ldlr$^{-/-}$ mice on high-fat diet but not in Ldlr$^{-/-}$Scd1$^{EC-/-}$ mice. When human aortic endothelial cells (HAECs) were subjected to PSS ($\tau_{ave} = 50$ dyne·cm^{-2}, $\partial\tau/\partial t = 71$ dyne·cm^{-2}·s^{-1}, 1 Hz), untargeted metabolomic analysis revealed that Stearoyl-CoA Desaturase (SCD1) in the endoplasmic reticulum (ER) catalyzed the fatty acid metabolite, oleic acid (OA), to mitigate inflammatory mediators. Following 24 hours of exercise, wild-type C57BL/6J mice developed elevated SCD1-catalyzed lipid metabolites in the plasma, including OA and palmitoleic acid (PA). Exercise over a 2-week period increased endothelial SCD1 in the ER. SCD1 overexpression via recombinant adenovirus also mitigated ER stress. Single cell transcriptomic analysis of the mouse aorta revealed interconnection of Scd1 with mechanosensitive genes, namely Irs2, Acox1 and Adipor2 that modulate lipid metabolic pathways. We found inverse relation between Scd1 and Vcam1 gene expression indicating the atheroprotective metabolites generated through Scd1 pathway. Taken together, exercise modulates PSS (TAWSS and OSI) to activate SCD1 as a metabolomic transducer to ameliorate inflammation in the disturbed flow-prone vasculature.

The dissertation of Mehrdad Roustaei is approved.

Alison Marsden

Peyman Benharash

Yu-Chong Tai

Dino Di Carlo

Tzung Hsiai, Committee Chair

University of California, Los Angeles

2023

To my family, mentors, and friends

TABLE OF CONTENTS

LIST OF FIGURES

ACKNOWLEDGEMENTS

I would like to express my deepest gratitude to my supervisor, Dr. Tzung Hsiai, for his invaluable guidance, unwavering support, and encouragement throughout my PhD journey. Dr. Hsiai's expertise, insight, and encouragement have been instrumental in shaping my research ideas and driving me towards excellence. His constant dedication and commitment to my success have been truly inspirational, and I am deeply grateful for his mentorship.

I would also like to thank my labmates, whose support have been an essential part of my graduate experience. I have had the privilege of working alongside some of the brightest and most talented individuals, whose ideas and feedback have been instrumental in shaping my research. In particular, I would like to thank Dr. Yichen Ding, Dr. Susana Cavallero, Dr. Parinaz Abiri, Zhaoqiang Wang, and Jing Wang who have been my constant companions, confidants, and sounding boards. Their support and encouragement have made my time in the lab both productive and enjoyable.

I would like to extend my heartfelt thanks to my parents, Nasrin and Reza, whose encouragement and support have been the bedrock of my academic journey. Their sacrifices, love, and support have made it possible for me to pursue my dreams and achieve my goals. I am deeply grateful for everything they have done for me. I also want to thank my brother, Mehdi, for his love and support throughout my PhD journey.

Lastly, I would like to thank my friends, who have been a constant source of inspiration and support throughout my PhD journey. Their unwavering support, encouragement, and laughter have kept me sane during the toughest times and made the good times even sweeter. Thank you for being there for me, and for believing in me even when I didn't believe in myself.

Overall, I am deeply grateful to everyone who has played a role in my academic journey. Without your support, encouragement, and guidance, I would not have been able to achieve my goals and pursue my dreams.

VITA

Education

- **Master of Science in Mechanical Engineering** 2015-2018

  Department of Mechanical Engineering, Sharif University of Technology, Tehran, Iran

- **Bachelor of Science in Mechanical Engineering** 2011-2015

  Department of Mechanical Engineering, Amirkabir University of Technology, Tehran, Iran

Experience

- **Graduate Student Researcher, Teaching Associate** 2018-2023

  University of California, Los Angeles

- **Graduate Research Assistant, Teaching Assistant** 2015-2018

  Sharif University of Technology, Tehran

SELECTED PUBLICATIONS

1. Roustaei, M., In Baek, K., Wang, Z., Cavallero, S., Satta, S., Lai, A., O'Donnell, R., Vedula, V., Ding, Y., Marsden, A.L. and Hsiai, T.K., 2022. Computational simulations of the 4D micro-circulatory network in zebrafish tail amputation and regeneration. Journal of the Royal Society Interface, 19(187), p.20210898.
2. Cavallero, S.*, Roustaei, M.*, Satta, S., Cho, J., M., Phan, H., In Baek, K., Blazquez-Medela, A. M., Gonzalez-Ramos, S., Vu, K., Park, S., Yokota, T., Sumner, J., Mack, J., Sigmund, C., Reddy, S., Li, R., Hsiai, T., “Exercise Mitigates Flow Recirculation and Activates Mechanosensitive Transcriptome to Uncover Endothelial SCD1 -Catalyzed Anti-Inflammatory Metabolites”, *Journal of Clinical Investigation*, Submitted.
3. Roustaei, M., Nikmaneshi, M.R. and Firoozabadi, B., 2018. Simulation of Low Density Lipoprotein (LDL) permeation into multilayer coronary arterial wall: Interactive effects of wall shear stress and fluid-structure interaction in hypertension. Journal of biomechanics, 67, pp.114-122.
4. Perley, A., Roustaei, M., Aguilar-Rivera, M., Kunkel, D.C., Hsiai, T.K., Coleman, T.P. and Abiri, P., 2021. Miniaturized wireless gastric pacing via inductive power transfer with non-invasive monitoring using cutaneous Electrogastrography. Bioelectronic medicine, 7, pp.1-8.
5. Baek, K.I., Chang, S.S., Chang, C.C., Roustaei, M., Ding, Y., Wang, Y., Chen, J., O'donnell, R., Chen, H., Ashby, J.W. and Xu, X., 2022. Vascular Injury in the Zebrafish Tail Modulates Blood Flow and Peak Wall Shear Stress to Restore Embryonic Circular Network. Frontiers in Cardiovascular Medicine, 9.
6. Wang, Z., Ding, Y., Satta, S., Roustaei, M., Fei, P. and Hsiai, T.K., 2021. A hybrid of light-field and light-sheet imaging to study myocardial function and intracardiac blood flow during zebrafish development. PLOS Computational Biology, 17(7), p.e1009175.
7. Ding Y, Gudapati V, Lin R, Fei Y, Packard RR, Song S, Chang CC, Baek KI, Wang Z, Roustaei M, Kuang D. Saak transform-based machine learning for light-sheet imaging of cardiac trabeculation. IEEE Transactions on Biomedical Engineering. 2020 May 1;68(1):225-35.
8. Ding Y, Gudapati V, Lin R, Fei Y, Packard RR, Song S, Chang CC, Baek KI, Wang Z, Roustaei M, Kuang D. Saak transform-based machine learning for light-sheet imaging of cardiac trabeculation. IEEE Transactions on Biomedical Engineering. 2020 May 1;68(1):225-35.
9. Abiri, P., Abiri, A., Gudapati, V., Chang, C.C., Roustaei, M., Bourenane, H., Anwar, U., Markovic, D. and Hsiai, T.K., 2020. Wireless pacing using an asynchronous three-tiered inductive power transfer system. Annals of biomedical engineering, 48, pp.1368-1381.
10. Abiri, P., Duarte-Vogel, S., Chou, T.C., Abiri, A., Gudapati, V., Yousefi, A., Roustaei, M., Chang, C.C., Cui, Q., Hsu, J.J. and Bersohn, M., 2021. In Vivo intravascular pacing using a wireless microscale stimulator. Annals of Biomedical Engineering, pp.1-9.
11. Fang, Y., Zou, Y., Xu, J., Chen, G., Zhou, Y., Deng, W., Zhao, X., Roustaei, M., Hsiai, T.K. and Chen, J., 2021. Ambulatory cardiovascular monitoring via a machine-learning-assisted textile triboelectric sensor. Advanced Materials, 33(41), p.2104178.
12. Satta, S., Lai, A., Cavallero, S., Williamson, C., Chen, J., Blázquez-Medela, A.M., Roustaei, M., Dillon, B.J., Ashammakhi, N., Carlo, D.D. and Li, Z., 2021. Rapid Detection and Inhibition of SARS-CoV-2-Spike Mutation-Mediated Microthrombosis. Advanced Science, 8(23), p.2103266.
13. Abiri, P., Luo, Y., Huang, Z.Y., Cui, Q., Duarte-Vogel, S., Roustaei, M., Chang, C.C., Xiao, X., Packard, R., Cavallero, S. and Ebrahimi, R., 2022. 3-Dimensional electrical impedance spectroscopy for in situ endoluminal mapping of metabolically active plaques. Sensors and Actuators B: Chemical, 354, p.131152.

CHAPTER 1: COMPUTATIONAL SIMULATIONS OF THE 4-D MICRO-CIRCULATORY NETWORK IN ZEBRAFISH TAIL AMPUTATION AND REGENERATION

Abstract

Wall shear stress (WSS) contributes to mechanotransduction underlying micro-vascular development and regeneration. Using computational fluid dynamics, we elucidated the interplay between WSS and vascular remodeling in zebrafish model of tail amputation and regeneration. The transgenic *Tg* (*fli1:eGFP; Gata1:ds-red*) zebrafish line was used to track the 3-D fluorescently-labeled vascular endothelium for post-image segmentation and reconstruction of fluid domain. Micro-particle image velocimetry was used to validate the blood flow. Following amputation to the dorsal aorta (DA) and posterior cardinal vein (PCV), vasoconstriction developed in the dorsal longitudinal anastomotic vessel (DLAV) along with increased WSS in the proximal segmental vessels (SV) from amputation. Angiogenesis ensued at the tips of the amputated DLAV and PCV where WSS was minimal. At 2 days post amputation (dpa), vasodilation occurred in a pair of SVs proximal to amputation, followed by increased blood flow and WSS, whereas in the SVs distal to amputation, WSS normalized to the baseline. At 3 dpa, the increase in blood flow in the arterial SV proximal to amputation promoted anastomosis with DLAV to form a loop with PCV. Thus, our *in-silico* modeling revealed the interplay between WSS and micro-vascular adaptation to changes in WSS and blood flow to restore micro-circulation following tail amputation.

1.1 Introduction

Biomechanical forces modulate vascular morphological adaptation during development [1, 2]. While mechanotransduction mechanisms underlying arterial inflammatory responses and oxidative stress are well-elucidated in the macro-scale in association with high Reynolds number flow [3], much less is known about the interplay between hemodynamic forces and vascular remodeling in the micro-scale in association with low Reynolds number flow [4, 5]. While endothelial dysfunction in the microvasculature is well-recognized in myocardial ischemia, diabetes, and peripheral artery diseases (PAD) [6-8], investigation into vascular injury-mediated changes in hemodynamic forces and adaptive vascular remodeling in the microvasculature remained an experimental challenge.

Zebrafish (*Danio Rerio*) embryos are transparent for light microscope imaging and genetically tractable for studying shear stress-mediated myocardial and vascular development [9]. We previously established 4-D light-sheet fluorescent microscopy (LSFM) to study the development of cardiac trabeculation during zebrafish cardiac morphogenesis [10, 11]. Combining LSFM and computational fluid dynamics (CFD), we have provided biomechanical insights into wall shear stress (WSS)-mediated endocardial trabeculation and outflow tract valvulogenesis in embryonic zebrafish [12-14]. Thus, we sought to use the transgenic zebrafish *Tg(fli1:eGFP; Gata1:ds-red)* line, in which enhanced green fluorescent protein-labeled endothelium allows for segmentation of 3-D vasculature and *ds-red*-labeled blood cells (mainly erythrocytes) for CFD reconstruction and micro particle image velocimetry (PIV).

Wall shear stress (WSS) intimately regulates mechanotransduction underlying vascular development, repair, and homeostasis [15, 16]. The spatial and temporal variations in fluid shear stress in the segmental vessels (SVs) of zebrafish embryos modulate the transformation of arterial to venous vessels, leading to a balanced distribution of arterial and venous SVs during vascular development [17]. In this context, the zebrafish microvascular network can be considered as an circuit analogy model consisting of the dorsal aorta (DA), segmental vessels (SVs), and the posterior cardinal vein (PCV). This model allows for simulating the microvascular response to blood cell partitioning in each SV, leading to uniform flow distribution [18, 19]. However, this zero-dimensional resistance modeling neglects bidirectional flow in the dorsal longitudinal anastomotic vessel (DLAV) network, vascular remodeling, including constriction and dilation, and angiogenesis of the DLAV and posterior cardinal vein (PCV) to form a new loop following tail amputation. Zero-dimensional modeling approaches also overlook the local variations in vessel diameter in association with the hemodynamic resistance in the microvasculature. For this reason, our CFD modeling sought to account for hemodynamic resistance for accurate estimation of WSS and luminal interaction.

We hereby demonstrate a 3-D CFD model encompassing 4 time-lapse stages of vessel regeneration following tail amputation, and subsequent loop formation between DA and PCV. We employed *eGFP*-labeled vascular endothelium by sub-micron confocal imaging and *ds-Red*-labeled blood cells to reconstruct the computational model and to predict the interplay between hemodynamic changes vascular morphological remodeling. We discovered a coordinated vascular adaptation to tail amputation that disconnected the DA from the PCV, followed by DLAV vasoconstriction at 1 day post amputation (dpa), and

SV dilation at 2 dpa, coupled with the rise and fall of WSS and the hemodynamic changes in flow rates. At 3 dpa, flow rate in the arterial SV proximal to amputation continued to rise and merged with DLAV to form a new loop with PCV. Thus, elucidating the interplay between shear forces and luminal remodeling provides new biomechanical insights into the micro-scale hemodynamics, with translational implications in vascular injury and repair under low Reynolds number flow in diabetes and peripheral artery disease.

1.2 Materials and Methods

Zebrafish (*Danio Rerio*) has the capacity to regenerate following distal tail amputation, providing a genetically tractable model to study changes in microcirculation in response to vascular development, injury, and regeneration [20-22]. We performed tail amputation on embryonic zebrafish to assess the dynamic changes in wall shear stress (WSS) and in flow rates in response to microvascular adaptation and remodeling proximal to the amputation site. The investigation of hemodynamic changes and morphological remodeling was established by imaging the transgenic *Tg(fli1:eGFP; Gata1:ds-red)* zebrafish embryos from 4 to 7 days post fertilization (dpf) (Figure 1.1 a-c), followed by post-imaging segmentation (Figure 1.1 d, e), and 3-D computational fluid dynamics (CFD) simulation (Figure 1.1 g, h). The enhanced green fluorescent protein (*eGFP*)-labeled endothelial cells expressed vascular endothelial growth factor (VEGF) receptor, denoted as *fli1*, and the *ds-red*-labeled blood cells (mostly erythrocytes and other blood lineages) allowed for tracking their movement. Thus, sequential analyses from stitching of the 3-D confocal imaging to computational modeling to particle imaging velocity (PIV) validated the hemodynamic changes proximal to the amputation site, vascular constriction and dilation, and new vessel formation (angiogenesis) in response to tail amputation (Figure 1.1).

1.3 Transgenic Zebrafish Model

The transgenic *Tg(fli1:eGFP; Gata1:ds-red)* embryos were rinsed with fresh standard E3 medium and cultivated at 28.5°C for 4 days after fertilization. Standard E3 medium was supplemented with 0.05% methylene blue (Sigma Aldrich, MO) to prevent fungal outbreak and 0.003% phenylthiourea (PTU, Sigma Aldrich, MO) to reduce melanogenesis. At 4 days post fertilization (dpf), embryos were randomly selected for immobilization with neutralized tricaine (Sigma Aldrich, MO) to undergo tail amputation. Zebrafish responses to anesthesia were monitored by the movement of the caudal fin. The tail was amputated at $\sim 100\ \mu m$ from the distal end. Following amputation, embryos were returned to fresh E3 medium and maintained for 3 days.

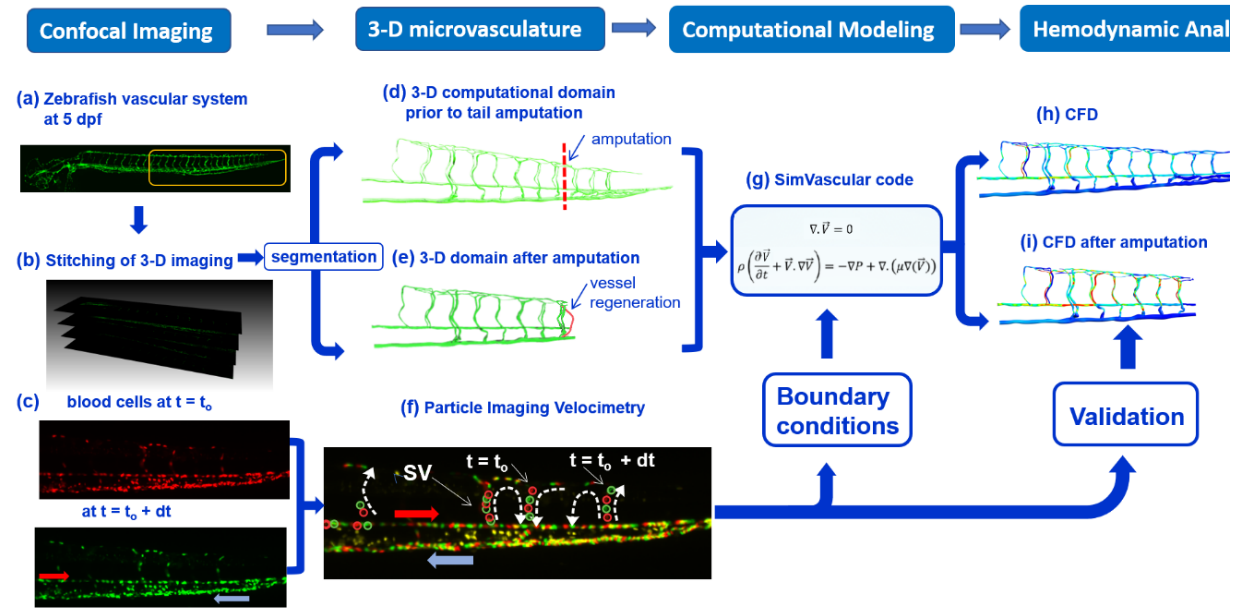

Figure 1.1. A pipeline of post-imaging segmentation, simulation, and validation for computational fluid dynamics (CFD). (a) Confocal microscopy was used to image the vascular system from a transgenic Tg (fli:eGFP) zebrafish embryo at 5 days post fertilization (dpf) . The vasculature was visualized via the enhanced green fluorescent protein (eGFP)-labeled endothelial cells that express VEGF receptor, fli1. (b) Stitching of the 3-D confocal images provided reconstruction of the vasculature for post-imaging segmentation. (c) The ds-red labeled blood cells (gata1:ds-red) in the zebrafish tail microvasculature were monitored at two different time points. The motion of ds-red-labeled blood cells allowed for quantitative assessment of the blood flow at t = to and t = to + dt in the microvascular network. Following segmentation, 3-D computational domain was reconstructed (d) prior to and (e) after tail amputation. (f) Particle image velocimetry (PIV) was performed to track the individually ds-red-labeled blood cells in the segmental vessels (SV) from t = to to t = to + dt. (g) SimVascular open-source blood flow modeling software was employed to solve the Navier-Stokes equations for incompressible flows, and boundary conditions were derived from PIV. (h) CFD analyses revealed wall shear stress prior to and after tail amputation. The magnitude of velocity in SVs was validated by PIV.

1.4 Post-amputation Imaging of Blood Flow and Microvasculature

The images of blood cells (*Gata1:ds-Red*) transport were captured by the inverted microscope (Olympus, IX70) and digital CCD camera (QIclick, Teledyne Qimaging, Canada). We performed time-lapsed imaging from 4 dpf to 7 dpf or 0 to 3 7dpa for both the amputated and control fish (amputation = 7; control = 5). The acquired images revealed the motion of erythrocytes in the microvasculature throughout multiple cardiac cycles.

The transgenic zebrafish *Tg(fli1:eGFP; Gata1:ds-red)* line was employed to capture *GFP*-labeled endothelium lining of the microvasculature undergoing remodeling following amputation from 4 to 7 dpf. The confocal-imaging system (Leica TCS-SP8-SMD) provided the isotropic submicron resolution in 3 dimensions (~500 nm in-plane and in *z* direction) for segmentation of the 3-D microvasculature. To reach this resolution, we stitched the high magnification ($64x$ objective lens) images at 4-7 dpf or 0-3 dpa, and we used 5 dpf for segmentation of the tail microvascular network.

We used our in-house light-sheet for the time-lapse imaging of zebrafish tail to assess the vascular remodeling in response to amputation. Our system utilized a continuous-wave laser (Laserglow Technologies, Canada) for planar illumination and a detection module including a set of filters and scientific CMOS (sCMOS, ORCA-Flash4.0, Hamamatsu, Japan). Our system provides a resolution of $2\mu m$ that was adequate for the measurement of microvascular diameter variation after amputation. [23]

1.5 Segmentation of Microvascular Network

We used the 3-D *GFP*-labeled images of endothelial lining to reconstruct the computational domain in SimVascular (Figure 1.1b) [24]. The pathline of each vessel was produced by connecting the points in the center of the lumen along the vessel in the 3-D image stack. For each vessel, the cross-section was calculated by interpolation of the manually specified points on the wall/lumen interface ($1D \rightarrow 2D$). Linking the cross-section areas along the vessel path with a spline function, we reconstructed each vessel in the network ($2D \rightarrow 3D$). Overall, we generated the vascular network for 21 segmental vessels (SVs), 20 dorsal longitudinal anastomotic vessels (DLAVs), dorsal aorta (DA), posterior cardinal vein (PCV), and capillary venous plexus (Figure 1.1 1d, e).

We implemented the post-amputation remodeling in microvasculature on the 3-D reconstructed computational domain (Figure 1.3 a-c). At 1 dpa, we removed 8 SVs (6 SVs for amputation and 2 SVs for vasoconstriction) from the zebrafish tail microvascular network distal to the heart to model the microvascular response to amputation followed by vasoconstriction at the DLAV (1 dpa). At 2 dpa, 2 SVs were added back to the microcirculation network where vasodilation was implemented (see Figure 1.3 d, e). We employed the time-lapse light-sheet fluorescent microscopy images to measure the average length and diameter of the regenerated vessel. The arterial SVs proximal to amputation was connected to the PCV to model loop formation at 3 dpa (Figure 1.3 c).

1.6 Particle Image Velocimetry for the Boundary Conditions and Validation

We developed and implemented our PIV code on *ds-Red*-labeled blood cells. To determine the boundary conditions for the inlet (DA) and to validate the results, we measured the velocity in DA and individual SVs. Our custom-written PIV algorithm was able to correlate with the intensity distribution of *ds-Red*-labeled erythrocytes in different time frames. A 2-D continuous polynomial function was fitted to the correlation distribution, and the position of the maximum correlation was determined from the polynomial function between two timeframes. At 20 frames per second, the computed erythrocyte position allowed for estimating the velocity in DA and SVs (Figure 1.1 c, f).

1.7 3-D Computational Modeling

A stabilized 3-D finite element method (FEM) was applied for CFD analysis to simulate the blood flow in the microvascular network using SimVascular's svFSI solver [24]. The Navier-Stokes equations were solved in svFSI with an incompressible flow assumption to quantify hemodynamic changes in response to tail amputation and vascular regeneration from 0 to 3 dpa (4-7 dpf) (Figure 1.1 g). In the setting of low Reynolds number ($Re = \frac{\rho V D}{\mu} \cong 5 \times 10^{-4} \ll 1$, where D is defined as the vessel diameter) in the microvascular network, viscous forces dominate over inertial forces, and the diameters and lengths of the vessels governed the pressure distribution and flow rates. Due to the low Reynolds number ($Re_{cell} = \frac{\rho V D_{cell}}{\mu} \cong 10^{-5} \ll 1$, where D is defined as the erythrocyte diameter), the pathway of the *ds-Red*-labeled erythrocytes followed the streamline of blood flow. Unlike the anucleate red blood cells in the mammalian circulation, zebrafish erythrocytes contain nuclei, and are thus, less deformable.

Despite the time-dependent nature of blood flow in zebrafish microcirculation, the Womersley number (ratio of transient inertial force to viscous force: $\alpha = \sqrt{\frac{\omega \rho D^2}{\mu}} \cong 5 \times 10^{-3} \ll 1$) was small, and the time-dependent terms in the Navier-Stokes equations were neglected in our continuum modeling [24].

We calculated the inlet velocity into DA during a cardiac cycle using the PIV code, and the time-averaged magnitude of V_{ave} = 238 μm·s^{-1} was applied as the inlet boundary conditions. Given the small Womersley number ($\alpha \ll 1$), a fully developed parabolic flow was considered in the inlet of DA (red arrow in Figure 1.1 f). A zero-pressure boundary condition was applied at the outlet of PCV (blue arrow in Figure 1.1 f). A non-slip boundary condition was assumed on the vessel walls.

To incorporate non-Newtonian effects of flow in the micro-circulation, we used a non-Newtonian viscosity model of the form:

$$\mu = \mu_0 \, \dot{\gamma}^{n-1} \qquad (1)$$

where μ is blood viscosity, $\dot{\gamma}$ the shear rate, μ_0 the consistency index, and n the power-law index. We employed $\mu_0 = 1.05 \times 10^{-3} \; Pa.s^n$ and $n = 1.09$ for the power-law equation [25]. We fitted the parameters and implemented this model into a Carreau-Yasuda model in svFSI [26]. We further analyzed the non-Newtonian effects on the flow rates and wall shear stress (WSS) in SVs by performing a parametric study based on the power-law index (n).

1.8 Results

1.9 Segmentation of 3-D microvasculature

Following 3-D stitching of the confocal images from the intact and amputated zebrafish tail, we performed segmentation of the microvascular network (Figure 1.2 a-b). Next, 3-D computational domain was reconstructed to simulate hemodynamic changes in response to tail amputation and vascular regeneration. The square box indicates the region of interest (ROI) for vascular segmentation and simulation (Figure 1.2 a). A representative 3-D computational domain was acquired from the segmentation process (Figure 1.2 c-d). The pressure drop across the venous plexus was deemed to be negligible due to both the short vessel length and low hemodynamic resistance. These considerations allowed for connecting the venous SV with the PCV for segmentation through the largest venous plexus.

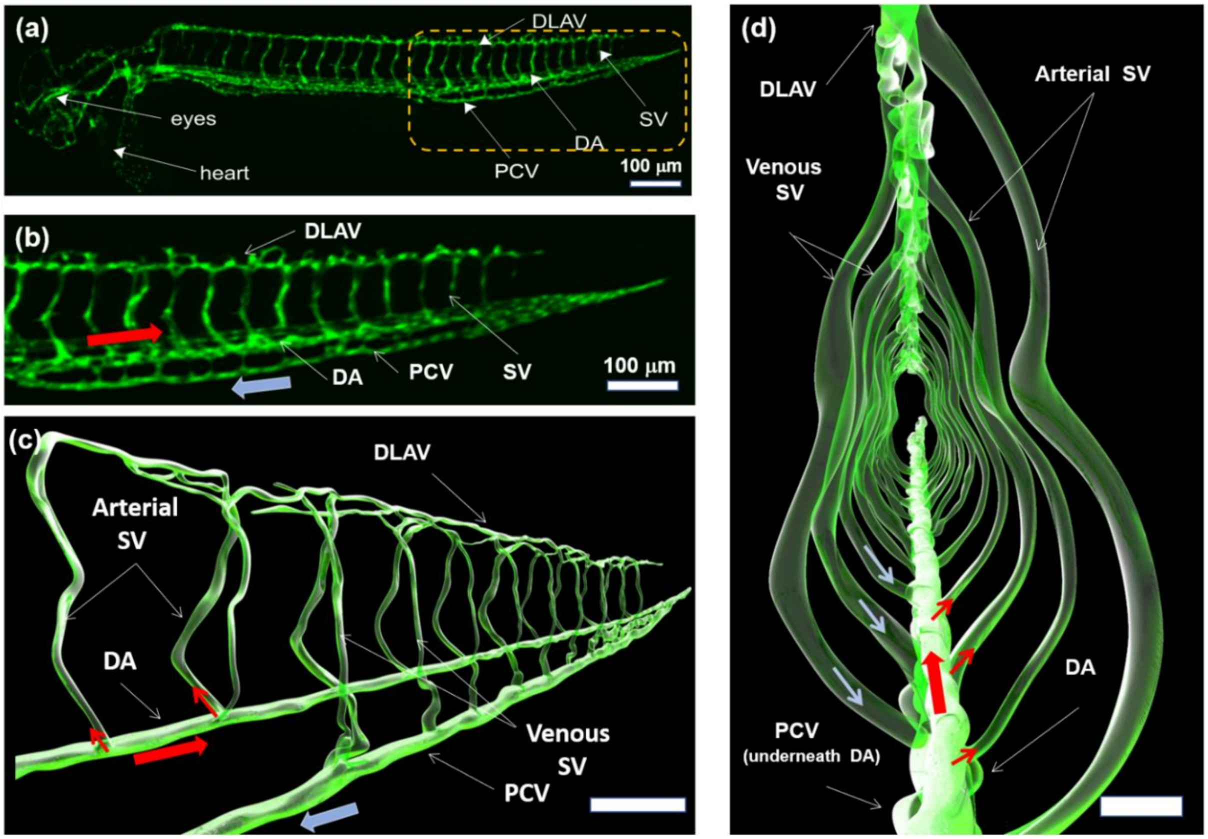

Figure 1.2. Segmentation of microvascular network I 3-D using confocal images (a) Transgenic Tg(*fli1:GFP*) zebrafish line was used to visualize the 3-D vascular network. The dashed rectangle (yellow) indicates the tail region from which vascular network was reconstructed for CFD simulation. (b) Magnification of the tail region depicts the flow direction in the DA in relation to PCV. (c) Representative segmentation of the 3-D vasculature recapitulates DA, SV, DLAV, and PCV. (d) Magnification of the yellow rectangle reveals the cross-section of the trail region where the vascular connectivity occurs between DLAV and PCV and between DA and SVs. Note that arterial SVs branch off from the DA, whereas venous SVs drain into PCV. CFD: computational fluid dynamics, DA: dorsal aorta, SV: segmental vessels, DLAV: dorsal longitudinal anastomotic vessel, and PCV: posterior cardinal vein.

While DLAVs are commonly assumed to be a single straight vessel for unidirectional flow, bidirectional flow occurs in the DLAVs in parallel. For this reason, a parallel pattern was proposed for the DLAVs according to their interconnection in the reconstructed vascular network (Figure 1.3 b and Figure S2.1). Thus, we demonstrate a pair of DLAVs in parallel, intersecting with the arterial and venous SV (in blue and red) to regulate the blood flow between SVs.

1.10 Vascular Remodeling Proximal to Tail Amputation Site

Confocal images revealed remodeling of the vessels and changes in blood flow from 0 to 3 days post-amputation (Figure 1.3). At 0-1 dpa, DLAVs underwent vasoconstriction, accompanied by a reduction in blood flow in the SVs proximal to the amputation site while both DLAV and PCV started to form a new connection toward the tail region (Figure S2.1) [27]. At 0-1 dpa, SVs proximal to the amputation site (SV # a+1, a+2, where *a* denotes the number of SVs that were removed after amputation) underwent statistically significant vasodilation (SV # a+1 and SV # a+2, $p < 0.0001$, n=61), whereas the diameter variations in the SVs distal from the amputation site (SV # > a+3) remained statistically unchanged (SV # a+3 to # a+6, $p > 0.05$, n= 61) (Figure 1.3 d-e). At 2 dpa, the DLAV proximal to SV# a+1 started to form a new loop with PCV (Figure 1.3). At 3 dpa, vasodilation in SV # a+1 and # a+2 attenuated in conjunction with the complete loop formation between DLAV and PCV, allowing for vascular regeneration to restore blood flow in the tail (Figure 1.3 c). Thus, we unveil micro-circular remodeling proximal to the tail amputation site, where the diameters of DLAV reduced at 1 dpa, followed by increased diameters in arterial SV # a+1 and # a+2, with concomitant angiogenesis in DLAV and PCV to form a new loop at 2 dpa, followed by normalization of SV diameter when a new loop connected the arterial and venous circulation.

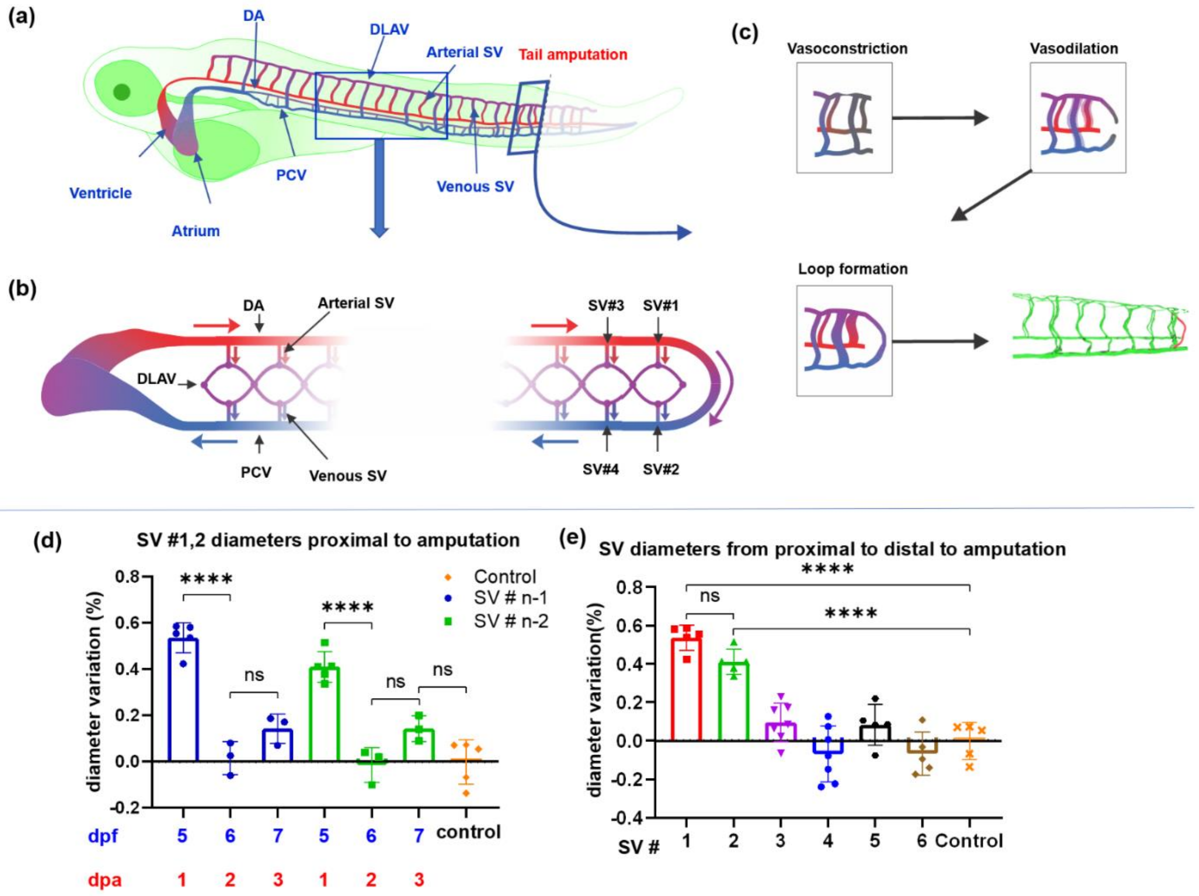

Figure 1.3. Zebrafish embryonic cardiovascular circulatory system in response to tail amputation and regeneration. (a) Arterial circulation is denoted in red and venous in blue. Two regions were magnified to reveal vascular network; namely, top view and tail amputation. (b) The top view reveals that DA originates from the ventricle, and PCV returns to the atrium. Arterial SV connect with DLAV, which drain to PCV via venous SV. (c) The tail amputation site (side view) illustrates SVs undergoing vasoconstriction, vasodilation, and loop formation proximal to amputation at 1, 2, 3 dpa. The proximal SVs were numbered from #1 to #6. (d) The changes in proximal SV diameters were compared from 0 dpa to 3 dpa. Both SV#1 and SV#2 underwent significant changes in diameter due to vasoconstriction at 1 dpa and vasodilation at 2 dpa ($p < 0.05$ vs. control, n=5). The changes at 3 dpa were statistically insignificant. (e) Changes in diameters were significant to the proximal SV#1 and SV#2 as compared to the distal SV#3-6. ns: not significant, DA: dorsal aorta, SV: segmental vessels, DLAV: dorsal longitudinal anastomotic vessel, and PCV: posterior cardinal vein, dpa: days post amputation.

1.11 Particle Image Velocimetry to Validate CFD

To validate our CFD model for low Reynolds number flow in the tail region, we performed particle image velocimetry (PIV) to obtain the mean velocity of blood flow in the SVs from proximal to distal to the amputation site. CFD simulation revealed velocity ranging from 130 to 550 $\mu m \cdot s^{-1}$, which was comparable to that obtained by PIV (Figure 1.4 e). The CFD results deviated from those of PIV by ~8%, and the velocity magnitude of the most distal SV #15 was significantly higher than that of the proximal SVs, indicating a good agreement with the experimental data.

1.12 Changes in the Hemodynamic Parameters Prior to Tail Amputation

Results from the 3-D CFD simulations included wall shear stress (WSS), pressure gradients, velocity profiles, and flow rates in the individual SVs. Our model verified the unique pattern of blood flow that recirculates between two SVs in parallel. The blood velocity and flow rate in DA decreased toward the tail region where arterial blood flow drains into the SVs and DLAV. Thus, this compartmental increase in hemodynamic resistance in both the SVs and DLAVs toward the tail region results in a decrease in flow rate in the DA.

Our 3-D simulations further demonstrated the bidirectional flow in the DLAVs in parallel (see Figure 1.3 b). The flow direction in each DLAV was regulated by the pressure difference between the arterial and venous SVs corresponding to the diameter distribution in SVs under Stokes flow ($Re \cong 10^{-3}$). As a result, the combination of DLAVs in parallel and SVs of various diameters modulated the flow rates and WSS (Figure 1.6 d). The flow rate in each SV was primarily regulated by the changes in diameters of the arterial and venous SVs and the interconnecting DLAV (Figure 1.4 d, f). Taken together, our *in-silico* model predicted that small changes in the arterial SV diameter and its branching vessels regulate the direction of blood flow in the micro-circular network.

1.13 Changes in WSS in Response to Tail Amputation and Regeneration

We compared changes in flow rates and WSS in the vascular network from 4 dpf (pre-amputation) to 7 dpf (3 dpa - loop formation) (Figure 1.4). Next, we compared the changes in the area-averaged WSS (mean WSS) and flow rates in SVs following tail amputation (Figure 1.6 b-c). At 0 to 1 dpa, we used the transgenic Tg (*fli1:eGFP*) zebrafish line where vascular endothelial growth factor (VEGF) receptors expressed in the vascular endothelial cells were encoded with the enhanced green fluorescent protein. We were able to visualize the DLAVs proximal to the amputation site undergoing vasoconstriction, restricting blood flow, along with a reduction in WSS in SVs #7-8 (Figure S2.2). Our simulation further showed that WSS increased following tail amputation in the rest of SVs between 0 to 1 dpa (Figure 1.6 a-e). This increase was preferentially higher in the arterial SVs (i.e., SV #9, 12) than in the venous SVs (i.e. SV #10, 11) as the former experienced the pressure variation upstream from the DLAV (Figure 1.6 e). At 0 - 1 dpa, the eGFP-labeled images revealed that DLAV and PCV formed 75% of the new vessel length while proximal SVs (SV #7, 8) developed a relatively low WSS due to DLAV vasoconstriction and the average WSS in the rest of the SVs was elevated comparing to unamputated fish (Figure 1.6 a-e).

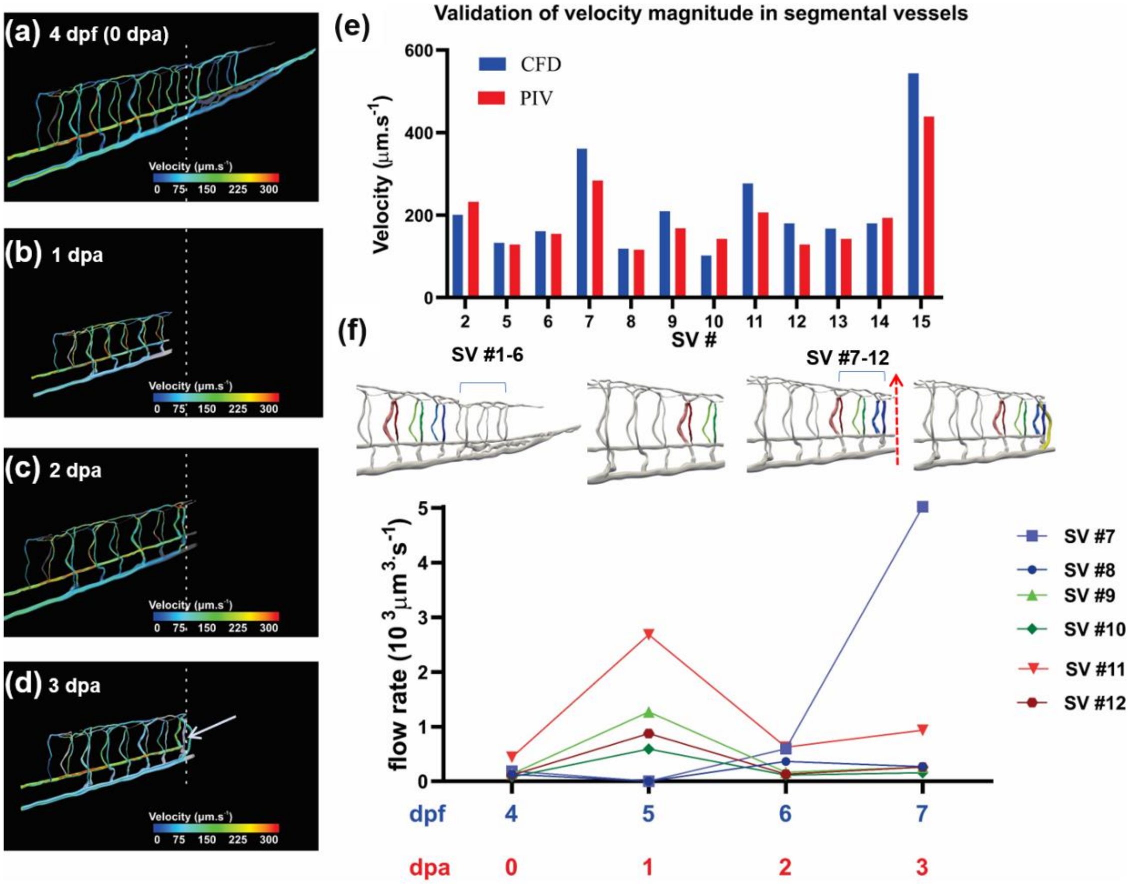

Figure 1.4. Computational Fluid Dynamics (CFD) simulates changes in hemodynamic responses to tail injury and regeneration. Velocity streamlines in the computational domain were color-coded by the velocity magnitude (a) at 4 days post fertilization (dpf) prior to tail amputation or 0 days post amputation (dpa), (b) 1 dpa, (c) 2 dpa, and (d) 3 dpa. Arrow indicates vascular repair with a loop formation. (e) Variations in velocity from the proximal to distal segmental vessels (SV) were compared between CFD and particle imaging velocimetry (PIV) prior to tail amputation. (f) The dynamic changes in flow rates developed from the proximal to distal SVs before (4 dpf or 0 dpa) and after tail amputation (5-7 dpf or 1-3 dpa). Note that flow rate in SV #7 increased at 3 dpa when DLAV formed a loop with PCV.

Simulation of blood flow at 2 dpa predicted that vasodilation of the proximal SVs (SV #7-8), and subsequent new loop connecting DLAV with PCV resulted in a proximal increase in flow rates and normalization in WSS in vascular network to the range prior to amputation (Figure 1.6 c, e). However, WSS and flow rates in the distal SVs decreased at 2 dpa to forestall further SV dilation (Figure 1.6 c, e). Our simulation also predicted that vasodilation increased the flow rate ($Q = \int \vec{V}.d\vec{A}$, where Q is flow rate, V is velocity and A is cross sectional area) proximal to the amputation site (SV #7-8) while the reduction in WSS further attenuated SV dilation ($WSS = \mu \frac{\partial V}{\partial r}_{r=R}$, where μ is viscosity, and r is the radius). Thus, our model demonstrates that SV dilation mediated a reduction in WSS (Figure 1.6 f and Figure 1.6 e).

The CFD model captured the loop formation of the regenerated vessel occurring distal to the arterial SV proximal to the amputation site (SV# 7). This SV supplied the arterial flow to DLAV, which underwent angiogenesis to form a new loop with PCV (Figure 1.4 d**,** Figure 1.6 d). This flow path (DA→SV #7→DLAV→regenerated vessel→PCV) decreased the blood supply to the rest of the SVs and DLAVs, leading to the DA→PCV loop formation, and an increase in flow rates and WSS in the arterial SV proximal to amputation (Figure 1.4 d, f and Figure 1.6 d, e). However, the blood flow to the venous SV proximal to the amputation site was reduced by the new loop between DLAV and PCV, resulting in a reduced WSS (Figure 1.4 d, f and Figure 1.6 d, e). Overall, CFD simulation demonstrated the changes in flow rate and WSS in response to the variation in SV diameters and flow rates needed to restore micro-circulation following tail amputation and regeneration.

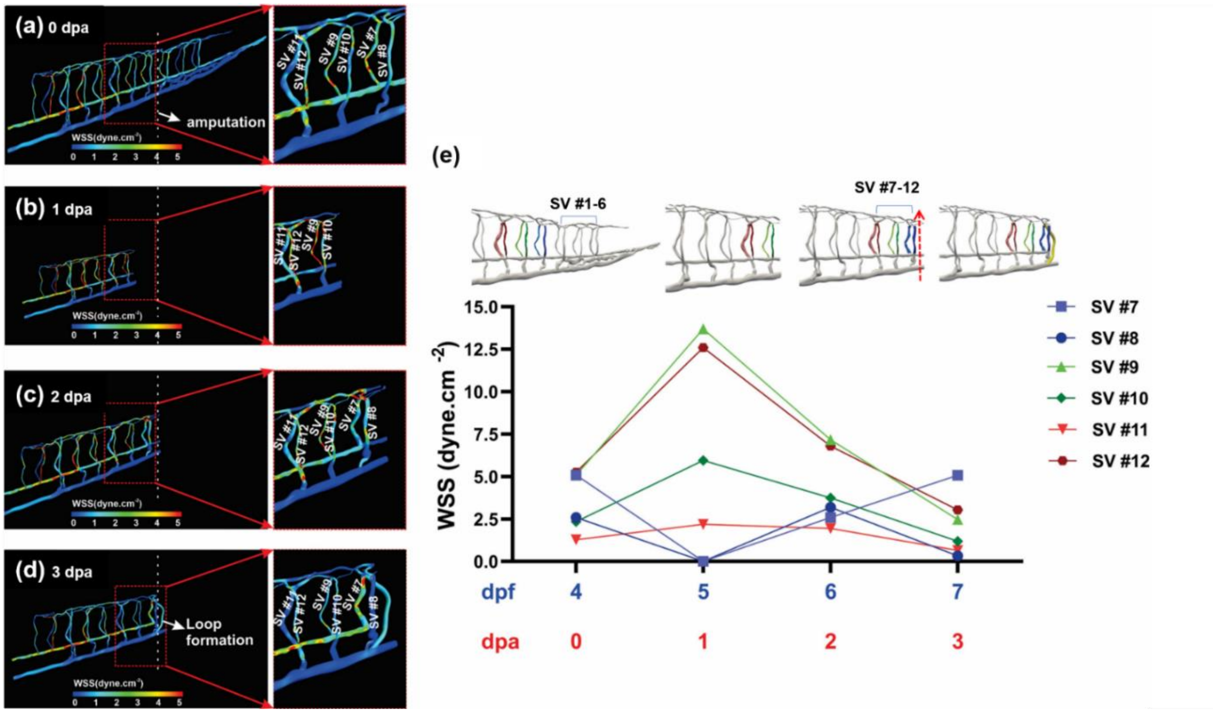

Figure 1.5. Computational fluid dynamics (CFD) simulated changes in wall shear stress (WSS) in response to tail amputation and regeneration. (a) Relatively high WSS developed in the distal arterial segmental vessels (SV) at 4 days post fertilization (dpf) prior to tail amputation. (b) An increase in WSS occurred in the proximal SV following tail amputation at 1-2 days post amputation (dpa). (c) An increase in WSS developed in the dorsal longitudinal anastomotic vessel (DLAV) and arterial SV proximal to amputation site, along with a reduction in WSS in the rest of SVs at 2 dpa. (d) A reduction in WSS developed in distal SVs in response to a loop formation connecting DLAV with posterior cardinal vein (PCV) at 3 dpa. (e) The mean WSS from the distal SV were compared prior to and post tail amputation, followed by loop formation at 3 dpa.

1.14 The Non-Newtonian Effects on the Flow Rates and Wall Shear Stress

From the power law model, we assessed the effects of non-Newtonian index on the microcirculation. We normalized the results according to the reported value for non-Newtonian index ($n = 1.09$). The normalized mean WSS in SVs were compared with different non-Newtonian indexes (Figure 1.6 a, c). Our parametric study indicates a non-linear effect of non-Newtonian index on WSS, with $n = 1.09$ indicating a maximum WSS condition (Figure 1.6 c). Similarly, the flow rates in SV exhibited a comparable trend (Figure 1.6 b), and the overall circulation of blood was independent of the non-Newtonian behavior.

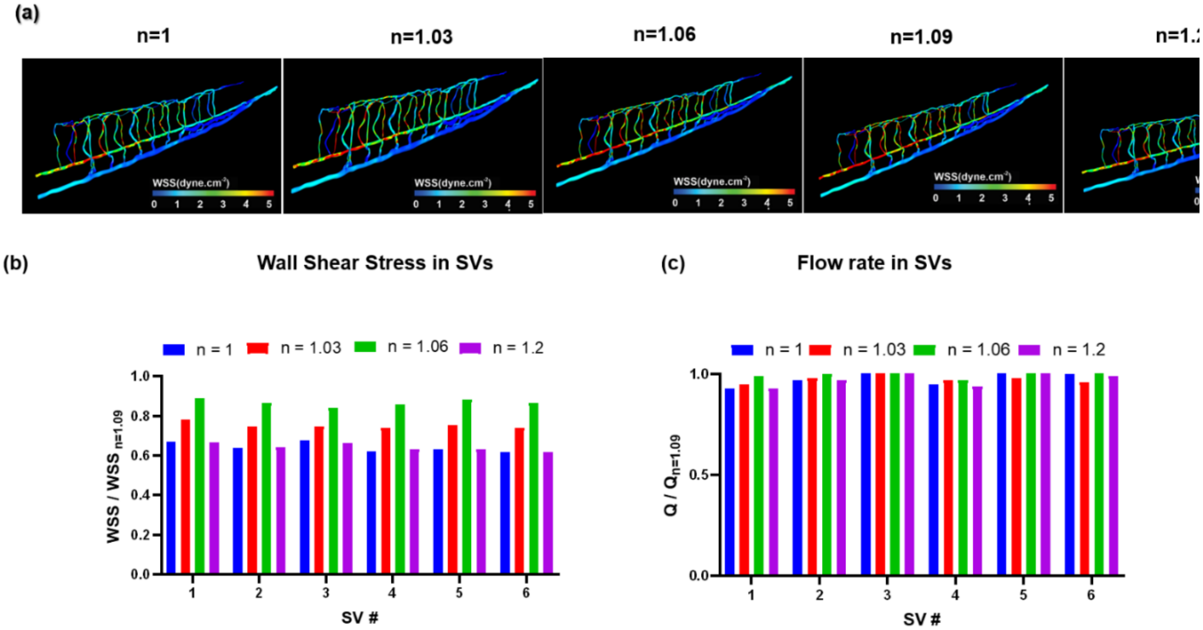

Figure 1.6. The effects of non-Newtonian Index (n) from 1 to n =1.2. (a) The non-dimensionalization was performed using the experimental index at n =1.09. Variations in WSS and flow rates were non-linear. The highest value for WSS was obtained using standard value n=1.09. (a) Dimensionless wall shear stress and (b) flow rates were compared from proximal to distal SVs.

We compared WSS contours for values of n from 1 to 1.2 (Figure 1.6 a). The overall blood flow to the microvasculature was not altered by varying the non-Newtonian model indices.

1.15 Discussion

Fluid shear stress imparts both metabolic and mechanical effects on vascular endothelial function [3]. During development, hemodynamic forces such as shear stress are intimately linked with cardiac morphogenesis [28]. We have demonstrated that peristaltic contraction of the embryonic heart tube produces time-varying shear stress ($\partial\tau/\partial t$) and pressure gradients (∇P) across the atrioventricular canal in a transgenic zebrafish *Tg*(*fli-1:eGFP; Gata1:ds-red*) model of cardiovascular development [1]. The advent of the zebrafish genetic system has enabled the application of *fli1* promoter to drive expression of enhanced green fluorescent protein (eGFP) in all vasculature throughout embryogenesis [29]; thereby, allowing for 3-D visualization for CFD simulation. By integrating 3-D reconstruction of confocal images with CFD simulation, we unraveled the interplay between wall shear stress (WSS) and microvascular adaptation in response to tail amputation and vascular regeneration. Tail amputation resulted in disconnection between DA and PCV, that triggered a well-coordinated DLAV vasoconstriction, accompanied with the initial decrease in WSS and flow rate in the SVs proximal to the amputation site. Simultaneously, an increase in WSS and flow rate in the SVs distal to amputation site developed due to bypass of the blood from DA during 0-1 dpa. WSS normalized to baseline in the SVs during vasodilation at 2dpa when DLAV and PCV formed a new loop at 3 dpa, whereas flow rates in arterial SV merged with DLAV and continued to rise. Thus, our data provide the new hemodynamic insights in micro-circular network injury and repair at low Reynolds numbers.

Hemodynamic shear forces are well-recognized to modulate endothelial homeostasis [30, 31], migration [32], vascular development and regeneration [33]. At a steady state, shear stress (τ) is characterized as dynamic viscosity (μ) of a fluid multiplied by its shear rate ($\dot{\gamma}$), defined as the tangential velocity gradient [3]: $\tau = \mu \cdot \dot{\gamma} = \mu \frac{\partial u_x}{\partial y}$. The zebrafish system allows for genetic manipulations of viscosity to alter shear stress [12, 22, 34]. We previously reported that injection of *Gata*-1a oligonucleotide morpholino (MO) to inhibit erythropoiesis resulted in a decrease in viscosity-dependent shear stress, and subsequent impaired vascular regeneration following tail amputation [35]. After *TNNT-2* MO injection to inhibit myocardial contraction and blood flow, zebrafish embryos also failed to develop tail regeneration at 3 dpa, whereas injection of *erythropoietin (Epo)* mRNA activates erythrocytosis to increase viscosity, resulting in restored vascular regeneration [35]. Thus, the rise and fall of WSS in adaptation to vascular remodeling in SV and DLAV proximal to the amputation site occurred during the formation of a new loop connecting between DLAV and PCV.

Our computational modeling was developed from the dynamic adaptation of vessel morphology to tail injury and vascular regeneration in the micro-scale under low Reynolds numbers. Choi *et al*. studied the variation in WSS in an embryonic zebrafish tail using an circuit analogy model [19], and they demonstrated changes in WSS in the microvascular network by partially occluding the blood flow in SVs. Chang *et al.* further proposed to incorporate the hemodynamic resistance of individual blood cells in the SVs toward the tail region [18]. However, this zero-dimensional resistance modeling did not capture vascular remodeling-associated changes in flow rates and WSS. Given the complex geometrical features of the zebrafish micro-circulation, the variations in vessel diameter are pivotal for determining hemodynamics. For this reason, our CFD model addressed vasoconstriction and vasodilation, and vascular regeneration in the microvascular network, demonstrating a spatiotemporal-dependent modeling of vascular injury and repair *in vivo*.

Spatial and temporal variations in WSS modulate vascular endothelial function and homeostasis. WSS in the microcirculation regulate the canonical Wnt/β-catenin signaling pathway for vascular development [22, 36], and WSS-activated Notch signaling modulates endothelial loop formation and endocardial trabeculation [12, 20, 35]. We have previously developed light-sheet imaging methods to study the development of trabeculation for zebrafish ventricles [10, 11]. Combining light-sheet microscopy and computational fluid dynamics (CFD), we assessed the role of wall shear stress (WSS) in formation of trabeculation and outflow tract valvulogenesis in embryonic zebrafish [12-14]. In this CFD modeling of vascular injury and repair, we further demonstrate the integration of CFD with genetic zebrafish system to uncover microvascular mechanics.

Blood effective viscosity provides the rheological basis to compute wall shear stress underlying cardiovascular morphogenesis. During development, blood viscosity regulates fluid shear stress to impart mechano-signal transduction to initiate cardiac trabeculation and outflow tract formation [12, 28]. However, the minute amount of zebrafish blood renders measurements of blood viscosity experimentally challenging [37]. We previously reported the capillary pressure-driven principle to develop microfluidic channels for measuring the small-scale blood viscosity [25], allowing for establishing a power-law non-Newtonian model to predict the transient rise and fall of viscosity during embryonic development. In this context, we further analyzed the non-Newtonian effects on the flow rates and wall shear stress in SVs by performing a parametric study based on the power-law index (n) Figure 1.6). From the power law model, we normalized the results according to the reported value for non-Newtonian index ($n = 1.09$) [25]. Our results indicate that despite local variations in WSS, the blood flow in micro=circulation was not significantly altered by variation of the non-Newtonian index. Overall, we unraveled the interplay between vascular remodeling and WSS in the face of tail amputation. Our CFD simulation was corroborated with micro-PIV. The results of the study provide translational implications in micro-vascular injury and repair for human diseases with associated vascular complications, such as diabetes and PAD.

1.16 Supporting Information

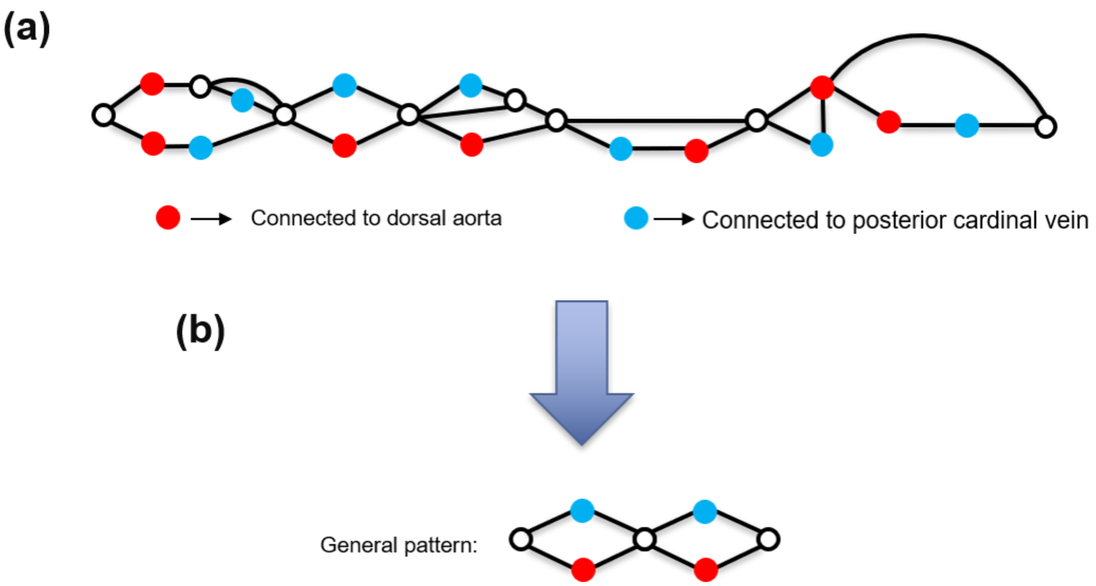

Figure S1.1. (a) The top-view from dorsal longitudinal anastomotic vessel (DLAV) network. The pattern of connectivity between arterial and venous segmental vessels (SVs) was used to simulate the embryonic zebrafish micro-circulation. (b) The propose generalized pattern of connectivity in DLAV network. Note that the red circles denote the connection between arterial SV and DLAV, and the blues circles denote the connection between venous SV and DLAV.

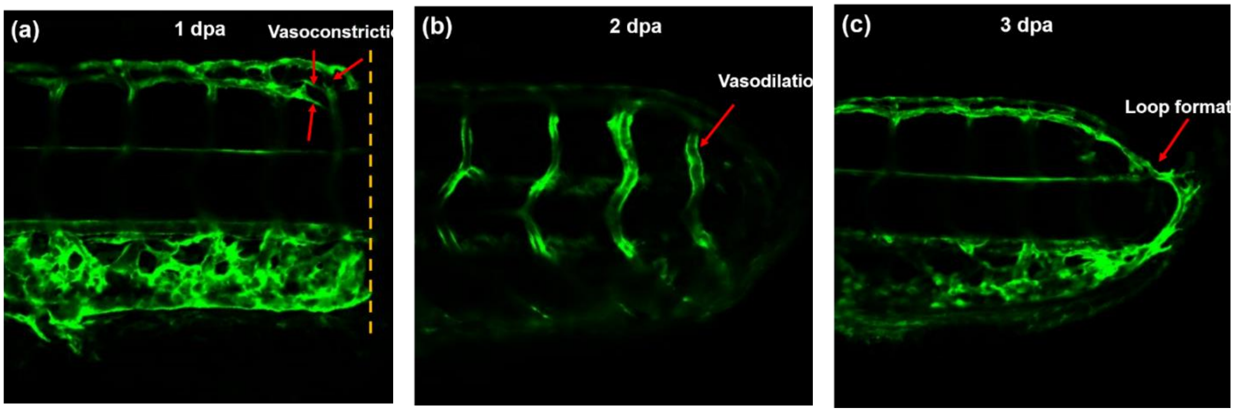

Figure S1.2. Confocal images of green-fluorescent protein (GFP)-labeled endothelial cells post amputation. (a) Vasoconstriction proximal to amputation at DLAV-SV connection at 1 days post amputation (dpa). (b) Vasodilation in the SVs proximal to amputation at 2 dpa. (c) Regeneration of new vessel from the tips of arterial SV and PCV at 2 dpa.

CHAPTER 2: EXERCISE MITIGATES FLOW RECIRCULATION AND ACTIVATES MECHANOSENSITIVE TRANSCRIPTOME TO UNCOVER ENDOTHELIAL SCD1-CATALYZED ANTI-INFLAMMATORY METABOLITES

2.1 Abstract

Exercise modulates vascular plasticity in multiple organ systems; however, the metabolomic transducers underlying exercise and vascular protection in the disturbed flow-prone vasculature remain under-investigated. We simulated exercise-augmented pulsatile shear stress (PSS) to mitigate flow recirculation in the lesser curvature of the aortic arch. Ultrasound-based 4-D+time moving boundary computational fluid dynamics analysis was performed on mouse aorta to simulate blood flow over several cardiac cycles. Exercise modulated the time-averaged shear stress (TAWSS) and oscillatory shear index (OSI), and upregulated SCD1 and attenuated well-known VCAM1 expression in the disturbed flow-prone aortic arch in Ldlr-/- mice on high-fat diet but not in Ldlr$^{-/-}$ Scd1$^{EC-/-}$ mice. When human aortic endothelial cells (HAECs) were subjected to PSS (τ_{ave} = 50 dyne·cm−2, $\partial\tau/\partial$t = 71 dyne·cm^{-2}·s^{-1}, 1 Hz), untargeted metabolomic analysis revealed that Stearoyl-CoA Desaturase (SCD1) in the endoplasmic reticulum (ER) catalyzed the fatty acid metabolite, oleic acid (OA), to mitigate inflammatory mediators. Following 24 hours of exercise, wild-type C57BL/6J mice developed elevated SCD1-catalyzed lipid metabolites in the plasma, including OA and palmitoleic acid (PA). Exercise over a 2-week period increased endothelial SCD1 in the ER. SCD1 overexpression via recombinant adenovirus also mitigated ER stress. Single cell transcriptomic analysis of the mouse aorta revealed interconnection of Scd1 with mechanosensitive genes, namely Irs2, Acox1 and Adipor2 that modulate lipid metabolic pathways. We found inverse relation between Scd1 and Vcam1 gene expression indicating the atheroprotective metabolites generated through Scd1 pathway. Taken together, exercise modulates PSS (TAWSS and OSI) to activate SCD1 as a metabolomic transducer to ameliorate inflammation in the disturbed flow-prone vasculature.

2.2 Introduction

Physical exercise augments blood flow in the cardiovascular system and modulates molecular transducers to ameliorate metabolic disorders [38]. During exercise, increased cardiac contractility and heart rate enhance PSS to improve endothelial cell plasticity [39], to mitigate atherosclerosis [40, 41], and to delay cognitive aging and neurodegeneration [42-45]. PSS is unidirectional and axially aligned with the flow direction in the straight regions of the vasculature, and PSS is known to activate antioxidants, including superoxide dismutase (SOD), and to attenuate proinflammatory cytokines, adhesion molecules, and NADPH oxidase system [46-49]. In contrast, disturbed flow, including oscillatory shear stress (OSS), is characterized as bidirectional and axially misaligned at the bifurcating regions or the lesser curvature of the aortic arch. OSS is well-recognized to induce oxidative stress and inflammatory response [46, 50-52]. However, the specific exercise-activated metabolomic transducers that mitigate inflammation and atherosclerosis in the disturbed flow-prone vasculature are not completely elucidated [53].

Several mechano-sensitive molecular transducers have been reported to regulate fatty acid (FA) uptake and transport in the vascular endothelium, including vascular endothelial growth factor B (VEGFB) [54, 55] and peroxisome proliferator activated receptor gamma (PPARγ) [56]. PPARγ is a member of the nuclear receptor superfamily, participating in the regulation of blood pressure, hypertension, hyperlipidemia, and insulin sensitivity [57-59]. While laminar shear stress upregulates SCD1 in human aortic endothelium through a PPARγ-dependent mechanism *in vitro* [60], we investigated whether physical exercise activates PPARγ-SCD1 pathway to promote vascular protective metabolites in the disturbed flow-exposed aortic arch.

SCD1 is a key transmembrane enzyme in the ER, catalyzing the conversion of saturated long-chain fatty acids (SFA) to Δ9-monounsaturated fatty acids (MUFA). The principal metabolite of SCD1 is oleic acid, which is formed by desaturation of stearic acid. The ratio of stearic acid to oleic acid is implicated in the regulation of cell growth and differentiation through its effect on cell membrane fluidity and signal transduction [61]. In this context, we performed *in silico* analysis to simulate exercise-augmented PSS to mitigate flow recirculation or disturbed flow in the lesser curvature of aortic arch. Our unbiased and untargeted metabolomic analyses uncovered that PSS activates endothelial SCD1 to catalyze the production of OA as a protective lipid metabolite, as evidenced by the attenuation of NF-κB-mediated inflammatory mediators and ER stress. To demonstrate SCD1 activation in the disturbed flow-prone aortic arch, we further developed mice with endothelial-specific SCD1 deletion (*Ldlr* $^{-/-}$ *Scd1* $^{EC-/-}$) to undergo supervised exercise in a voluntary wheel running system. We demonstrated that exercise modulates PSS (TAWSS, and OSI) and activates endothelial SCD1 as a metabolomic transducer to catalyze lipid metabolites that ameliorate inflammation and atherosclerosis in the disturbed flow-exposed vasculature.

Computational fluid dynamics (CFD) has been receiving increasing attention over the past few decades for analysis of blood flow in cardiovascular system. The flow-meditated cardiovascular diseases such as atherosclerosis and hypertension can be better understood and addressed using a comprehensive hemodynamic analysis. The recent advancements in small imaging technologies (micro-CT, ultrasound, micro-MRI) have enabled the researchers to perform time-lapse imaging and track the changes in terms of boundary conditions for the model 1. Micro-CT and MRI provides a high resolution for reconstructing the aortic geometry 1-5. However, the imaging cost is usually prohibitive given the number of mice usually required for providing statistical significance. In addition, these imaging modalities do not accurately estimate flow parameters to validate the simulation. 4-D MRI is known to underestimate wall shear stress and micro-CT, as an invasive technique, might not be the optimal option for acquiring boundary conditions for a CFD model 4, 6. In addition, the effect of wall motion as a result of heart contractility and also vessel deformation plays a crucial role in WSS profiles in the aorta. Hereby, we present an ultrasound-based computational pipeline that generates the computational domain based on 2-D B-mode images. We extract 3-D+time information from 2-D+time images and apply the deformation filed on the lumen/wall interface to obtain the moving boundary domain for CFD analysis. The pulse wave doppler is utilized to estimate the inlet boundary conditions and to validate the velocity profile downstream. Therefore, our computational pipeline provides an efficient, validated, and cheap way to analyze blood flow in mouse aortic arch.

2.3 Materials and Methods

2.3.1 Mice Lines

Male and female C57BL/6J mice from Jackson (Strain 000664) were used for the exercise studies. The endothelial dominant-negative *Pparγ* (EC-DN-*Pparγ*) mice line was kindly provided by Curt D. Sigmund at the University of Iowa [62]. These mice express a human dominant negative *Pparγ* variant with the human V290 mutation under the control of the endothelial-specific *Cdh5* promoter.

Mice carrying the *Ldlr*^{tm1Her} mutation were obtained from Jackson Laboratories (Strain 002207) to generate *Ldlr*$^{tm1Her/tm1Her}$ (*Ldlr* $^{-/-}$) mice. To study SCD1-mediated arterial inflammation, we crossed *Ldlr* $^{-/-}$ with mice carrying a conditional mutation of the *Scd1* gene (*Scd1*$^{flox/flox}$) generated by James Ntambi lab at the University of Wisconsin Madison [63, 64]. The endothelial deletion of *Scd1* gene was achieved by Cre recombination with

Cdh5Cre+ mice*,* in which the *Cdh5* promoter (also known as *VE-Cadherin*) drives the constitutive expression of *Cre* in endothelial cells. *Cdh5Cre* mice were obtained from the laboratory of Luisa Iruela-Arispe [65]. *Ldlr*$^{-/-}$, *Scd1*$^{flox/flox}$, *Cdh5*^{Cre} mice (subsequently called *Ldlr*$^{-/-}$, *Scd1*$^{\mathrm{EC}-/-}$) were generated through appropriate breeding schemes and PCR genotyping in tail DNA. Littermates *Ldlr*$^{-/-}$, *Scd1*$^{flox/flox}$ (or *Ldlr*$^{-/-}$ for simplicity) were used as controls. All mice were maintained on a C57BL/6J genetic background to reduce genetic variability.

2.3.2 Induction of Atherosclerosis

Mice at 6-8 weeks of age were used for all our studies. Mice were fed a high fat diet (HFD, Teklad TD.88137, Envigo, Indianapolis, IN) for 4 weeks. The formulation is highly enriched in saturated fatty acids (>60% of total fatty acids) and contains 42% kilocalories from fat. The diet was supplied as soft pellets and replaced every 2-3 days to ensure freshness. After 2 weeks, some animals were transferred to individual exercise cages and continued receiving HFD for 2 more weeks (Figure 2.8 A).

2.3.3 Voluntary Wheel Exercise Studies

The wild-type C57BL/6J mice fed a regular rodent chow versus *Ldlr*$^{-/-}$ and *Ldlr*$^{-/-}$ *Scd1*$^{\mathrm{EC}-/-}$ mice on HFD were assigned to exercise. They were transferred to individual polycarbonate cages with a stainless-steel running wheel. Each wheel had an automated counter to record the distance and speed at which each animal ran in either direction (BIO-ACTIVW-SOFT from Bioseb, Pinellas Park, FL, USA). Spontaneous wheel running was monitored continuously over 2 weeks. Animals received food and water *ad libitum* during the data collection period. Mice in the no exercise group were housed in regular static cages in the same testing room to minimize environmental variations.

2.3.4 Quantification of Arterial Strain and Wall Shear Stress after Exercise

We used the B-mode images of the aortic arch to simulate the time-dependent 3-D model, and reconstructed a 3-D model of the lumen structure by resolving the vessel wall curvature along the centerline of the aorta and its branches using our customized script (Matlab). To obtain the boundary conditions for our in-silico analysis of exercise-augmented PSS, we interrogated the mouse aortic arch via an ultrasound transducer (Vevo 3100, FUJIFILM VisualSonics) (Figure 2.1 a)**.** ECG-gated PW Doppler was acquired for the inlet boundary condition of the time-dependent flow of the aortic arch. This inlet condition was calibrated for the exercise model as previously reported [66, 67]. The three-element Windkessel model was implemented at the 4 outlets of the model computational domain; namely, brachiocephalic, left common carotid, left subclavian artery, and descending aorta [68].

Time-averaged Wall shear stress ($TAWSS = \frac{1}{T}\int_0^T |WSS|\, dt$) contours, oscillatory shear index ($OSI = \frac{1}{2}\left(1 - \frac{\left|\int_0^T WSS\, dt\right|}{\int_0^T |WSS|\, dt}\right)$) and velocity profiles for a time-dependent model were acquired by solving the Navier-Stokes equations using the using SimVascular's svFSI solver [69].

$$\rho\left(\frac{\partial \vec{V}}{\partial t} + \vec{V}.\nabla\vec{V}\right) = -\nabla P + \mu\nabla^2\vec{V}$$

$$\nabla.\vec{V} = 0$$

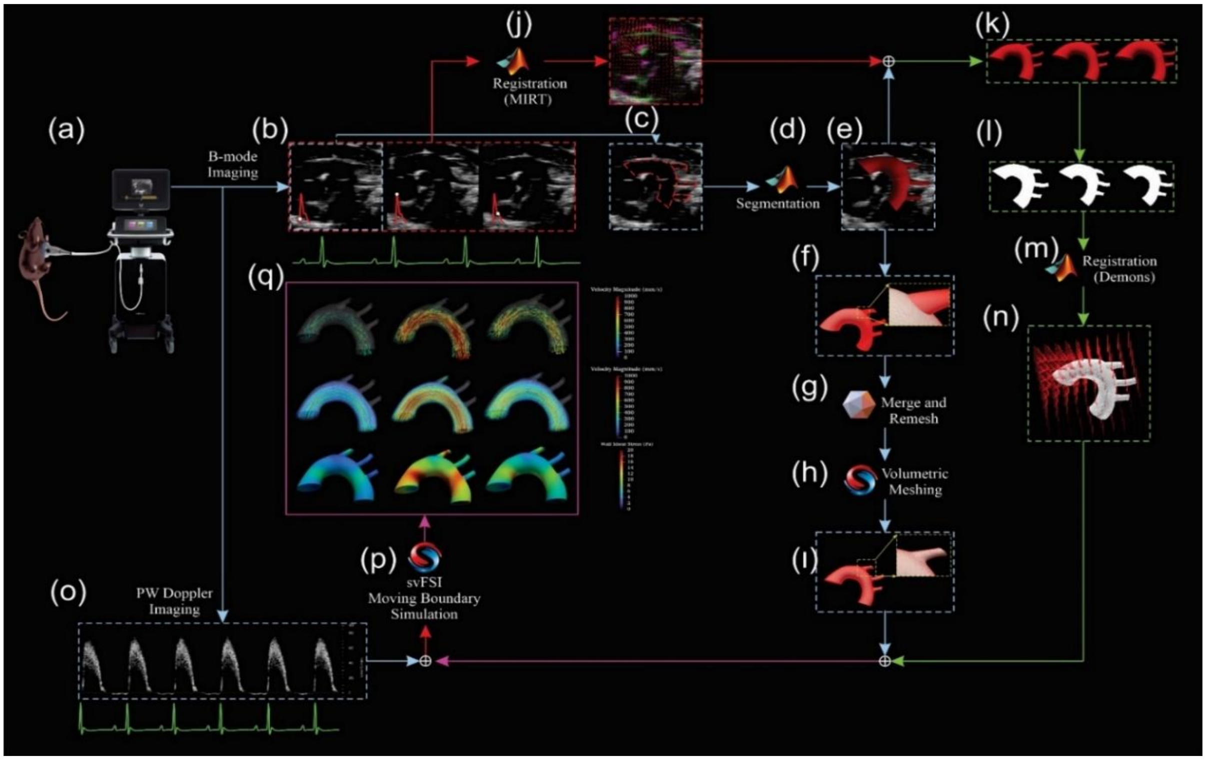

Figure 2.1. Computational pipeline to generate 3-D+time moving boundary CFD model from 2-D+time B-mode ultrasound images. (a) A schematic of the Vevo 3100 machine to perform ultrasound imaging on mouse cardiovascular system (b) time-dependent B-mode images of the aortic arch synchronized with ECG (c) lumen/wall interface for aorta and the branches (d) segmentation was performed by our customized matlab script (e) computational domain structure of the first frame in 3-D extracted by revolving lumen/wall interface around centerline of each vessel followed by surface meshing using our developed Matlab script. (f) mesh misalignment at the branching point (g) Meshmixer was used for combining and aligning the surface meshes of aorta and branches from the first frame followed by remeshing and scaling (h) volumetric meshing was performed in SimVascular (i) the output surface and volumetric mesh with aligned edges and nodes generated from the first frame (j) registration was performed using medical image registration toolbox on 2-D B-mode images (k) misaligned surface meshes generated for all of the frame over a cardiac cycle by applying registration-acquired deformation on the original lumen/wall interface followed by (l) time-dependent

misaligned surface meshes were converted into 3-D+time binary image (m-n) deformable image registration (Demons) was applied on the 3-D+time binary images to calculate deformation field in 3-D+time (n) the deformation was applied on the surface and volumetric meshes from i to generate moving boundary vessel structure with aligned mesh (o) pulse wave doppler signal at aortic root was used as inlet boundary condition (p) the generated mesh and boundary conditions were inputted to svFSI code to perform CFD simulation (q) representative results of 3-D+time moving boundary simulation: velocity vectors colored and scaled by velocity magnitude (top), velocity-colored streamlines (middle), wall shear stress contour (bottom).

2.3.5 A Dynamic Flow System to Simulate PSS Profiles

A dynamic flow channel was used to recapitulate hemodynamics of human carotid arterial bifurcations [70]. The flow system was designed to generate well-defined flow profiles across the width of the parallel flow chamber at various temporal gradients ($\partial\tau/\partial t$), frequencies, and amplitudes. Metabolite samples were collected from HAEC monolayers exposed to pulsatile shear stress (PSS, TAWSS = 50 $\text{dyne}\cdot\text{cm}^{-2}$ accompanied by $\partial\tau/\partial t = 71\ \text{dyne}\cdot\text{cm}^{-2}\cdot\text{s}^{-1}$ at 1 Hz) or static conditions for 4 h. Cells were trypsinized, fixed in 4% PFA, and immediately stored at -80°C before submission for metabolomic analysis.

2.3.6 SCD1 overexpression via adenovirus

The replication defective adenovirus Ad5/F35 was designed using the licensed Vector Builder software. The vector pAd5/F35[Exp]-mCherry-Cd144>mSCD1[NM_009127.4] contains the Cdh5 promoter to confer EC specificity, mCherry as a reporter to allow for visualization of targeted ECs, and the sequence of mouse *Sdc1* [NM_009127.4]. The adenovirus was generated by standard laboratory procedures in BSL2 biosafety cabinets using 293A cells. On the day of transfection, recombinant adenoviral plasmids were digested by the restriction enzyme PacI. The cells were transfected with Lipofectamine-DNA mix (Thermo Fisher Scientific) according to the manufacturer instructions.

Lipofectamine-DNA mix was added to the culture flasks, which were returned to CO_2 incubator at 37°C. The virus was left to infect the cells and then purified through a centrifugation process. Control adenovirus was (pAd5/F35[Exp]-mCherry-Cd144).

2.3.7 Metabolomic Analysis

The metabolomic analyses in mouse plasma samples or endothelial cell lysates were performed at the West Coast Metabolomics Center at the University of California Davis, CA. Gas chromatography time-of-flight mass spectrometry (GC-TOF-MS) untargeted analysis identified 170 known metabolites and 290 unknown compounds. Metabolites were reported with retention index, quantification mass, and full mass spectra. Relative quantification was assessed by peak height. Targeted assays for selected fatty acid metabolites were performed for absolute quantification using stable isotope-labeled internal standards.

The data analysis was performed using MetaboAnalyst 5.0 (Research Resource Identifier RRID:SCR_015539). Before performing PCA, the concentrations of subjected metabolites were corrected using the Pareto scaling method to normalize the measurements of different metabolites on the close scale. The *x*-axis in the figures was depicted as the first principal component (PC1) representing the space with the largest variance in data, whereas the *y*-axis was depicted as the second principal component (PC2) representing the space with the second largest variance. The ovals are 95% inertia ellipses.

2.3.8 Single Cell RNA Sequencing

The complete aorta was perfused with cold PBS, isolated and dissected to eliminate the surrounding periaortic fat. After mincing with scissors, a single cell suspension was obtained through enzymatic digestion with elastase (Worthington, Lakewood, NJ, USA) and liberase ((Roche, Basel, Switzerland) at 37°C. The preparation was passed through a 70 □m filter and treated with Red Blood Cell lysis buffer (Abcam, Waltham, MA, USA). Single cells were resuspended in PBS containing 0.04% BSA, counted and assessed for viability using Trypan Blue. Single cell RNA Sequencing was performed using the 10X Genomics Chromium platform at the UCLA Technology Center for Genomics and Bioinformatics. Raw sequencing data was demultiplexed and aligned using the Cell Ranger software from 10X Genomics, and we obtained the gene expression count matrix from Cell Ranger for downstream analyses. We sequenced ~ 20,000 cells from the aorta. Quality control and data processing were performed in the Seurat package. PCA was used to reduce the number of features during the clustering stage. We used the modularity optimization algorithms implemented in Seurat to classify cells into clusters, and to identify the cell-type in each cluster using the cell-type-specific genes. Seurat package was used to normalize count numbers by geometric mean and calculate the fold change and statistical significance, with $p < 0.05$ considered significant. Data were visualized using Python and Cytoscape.

2.3.9 Single Cell RNA Data Analysis

The raw fastq scRNA reads were processed using Cell Ranger software (10x Genomics) and subjected to quality control with FastQC. The resulting output data for the three treatment groups were analyzed with the Scanpy package in Python. To generate an annotated data object, the data across groups were concatenated. Cells with gene counts above 4,000 or below 200 were filtered, as were those with a mitochondrial gene count exceeding 10%. Subsequently, we performed normalization, principal component analysis, variable gene extraction, non-linear dimensional reduction, and clustering to produce Uniform Manifold Approximation and Projection (UMAP) plots and identify cell clusters using cell specific marker genes. To visualize gene expressions between categories of related diet +/- exercise we created a circular heatmap. Circular heatmap features the log2 transformation of the fold changes, calculated as described above. Our heat maps were created using the heatmap.2 program in the 'gplots' package of R (http://cran.r-project.org). Circlize package R was used to generate circular heat map and hierarchical clustering. DESeq was used for normalization. All heat maps shown are row-normalized for presentation purposes.

2.3.10 Statistics

All data are presented as mean ± standard error of the mean (SEM). Cell culture results consisted of 3 independent experiments. GraphPad Prism software (GraphPad Software, La Jolla, CA) was used for statistical analysis. *t*-test or two-way ANOVA with multiple comparisons (genotype and presence or absence of exercise being the two dependent variables) and Tukey *post hoc* tests were performed to determine the statistical significance. *P* values < 0.05 were considered statistically significant.

2.3.11 Study Approval

Animal experiments were performed in compliance with the Institutional Animal Care and Use Committee (IACUC) at the University of California Los Angeles (UCLA), under animal welfare assurance number A3196-01. The Animal Research Committee (ARC) reviewed all animal procedures performed at UCLA. The mice colony was housed in the facilities maintained by the UCLA Department of Laboratory Animal Medicine (DLAM). Mice obtained from external sources were allowed to acclimate for at least one week at UCLA facilities prior to the start of the experiments.

2.4 Results

2.4.1 Pulsatile shear stress (PSS) up-regulates endothelial SCD1 to catalyze lipid metabolites

Following well-defined PSS (TAWSS = 50 dyne·cm^{-2}, and slew rate, $\partial\tau/\partial t = 71$ dyne·cm^{-2}·s^{-1}, at 1 Hz) to HAECs monolayers for 4 h (Figure 2.2 A), untargeted metabolomic analysis demonstrated that the SCD1-catalyzed metabolite oleic acid (a monounsaturated omega-9 fatty acid) was significantly increased ($^*p < 0.05$, PSS vs. static condition, n=4) (Figure 2.2 B, E). However, PSS did not increase the saturated fatty acid precursors palmitic or stearic acid (Figure 2.2 B). PSS also significantly increased linoleic acid (a polyunsaturated omega-6 fatty acid) and its derivative azelaic acid. Both metabolite heatmap and Principal Component Analysis (PCA) demonstrated that PSS-mediated metabolites were separated from the basal levels (Figure 2.2 C, D). PSS also increased the production of glycolytic metabolites, including glucose-6-phosphate and fructose-6 phosphate, as previously reported [71]. Although ECs primarily consume glucose through anaerobic glycolysis [72], they contain the enzymatic machinery for FA oxidation [73]. Consistently, our bioinformatic analysis of compound networks [74] showed interconnections among glycolytic and lipid metabolite nodes in HAECs after PSS exposure (Figure 2.2 F).

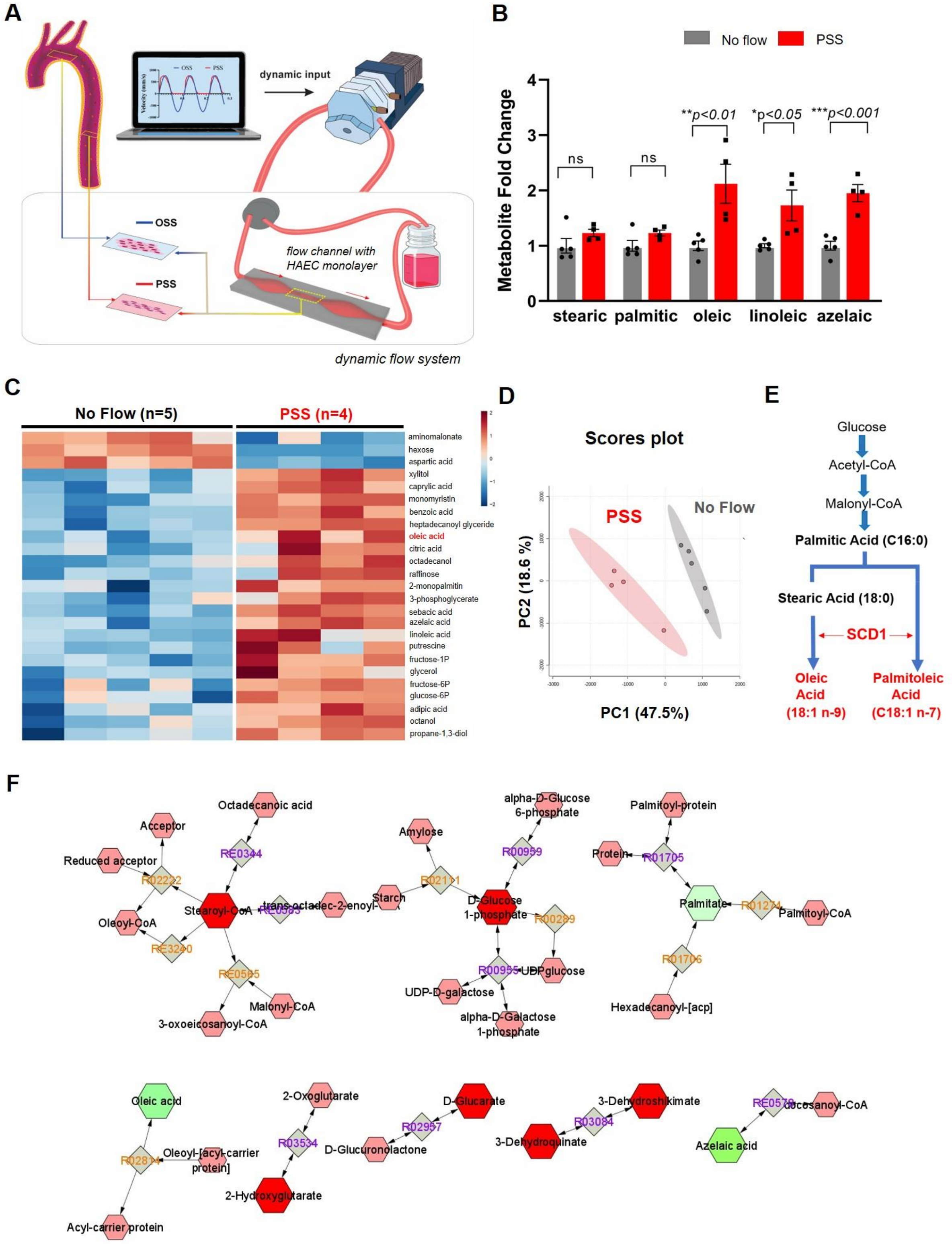
A
dynamic input
OSS
PSS
flow channel with HAEC monolayer
dynamic flow system
B
No flow
PSS
Metabolite Fold Change
ns
ns
**p<0.01
*p<0.05
***p<0.001
stearic
palmitic
oleic
linoleic
azelaic
C
No Flow (n=5)
PSS (n=4)
aminomalonate
hexose
aspartic acid
xylitol
caprylic acid
monomyristin
benzoic acid
heptadecanoyl glyceride
oleic acid
citric acid
octadecanol
raffinose
2-monopalmitin
3-phosphoglycerate
sebacic acid
azelaic acid
linoleic acid
putrescine
fructose-1P
glycerol
fructose-6P
glucose-6P
adipic acid
octanol
propane-1,3-diol
D
Scores plot
PSS
No Flow
PC2 (18.6 %)
PC1 (47.5%)
E
Glucose
Acetyl-CoA
Malonyl-CoA
Palmitic Acid (C16:0)
Stearic Acid (18:0)
SCD1
Oleic Acid (18:1 n-9)
Palmitoleic Acid (C18:1 n-7)
F
Octadecanoic acid
Acceptor
Reduced acceptor
RE0344
R02222
Stearoyl-CoA
RE0583
trans-octadec-2-enoyl-
Oleoyl-CoA
RE3240
RE0565
Malonyl-CoA
3-oxoeicosanoyl-CoA
Amylose
Starch
R02111
alpha-D-Glucose 6-phosphate
R00959
D-Glucose 1-phosphate
R00289
R00955
UDPglucose
UDP-D-galactose
alpha-D-Galactose 1-phosphate
Palmitoyl-protein
Protein
R01705
Palmitate
R01274
Palmitoyl-CoA
R01706
Hexadecanoyl-[acp]
Oleic acid
R02814
Oleoyl-[acyl-carrier protein]
Acyl-carrier protein
2-Oxoglutarate
R03534
2-Hydroxyglutarate
D-Glucuronolactone
R02957
D-Glucarate
3-Dehydroshikimate
R03084
3-Dehydroquinate
RE0578
docosanoyl-CoA
Azelaic acid

Figure 2.2. Pulsatile shear stress (PSS) modulates endothelial metabolome and increases SCD1-catalyzed metabolites. (A) A custom-built dynamic flow system was used to simulate spatial and temporal variations in shear stress in the arterial system. The machine language (Lab View) drives a peristaltic pump to generate pulsatile wave forms. The configuration of flow channel (contraction and extraction) was designed to provide the well-defined pulsatile flow with the specific slew rates ($\partial\tau/\partial t$), time-averaged shear stress (τ_{wave}), frequency (Hz), and amplitude to simulate exercise-augmented PSS. The flow channel was maintained inside the incubator at 37°C with 5% CO_2. A confluent HAEC monolayer was seeded on the glass slides in the flow channel. (B) Metabolite samples were collected from HAECs under the static condition (control or no flow, n=5) or PSS (n=4 at 1 Hz for 4 hours) for the untargeted metabolic analysis. PSS significantly increased the lipid metabolites; namely, oleic, linoleic and azelaic acids ($*p < 0.05$ PSS vs. static condition). (C) The heatmap reveals an increase in both glycolytic and fatty acid metabolites. The data were analyzed after normalization and scaling using the Pareto method. (D) Score plots by the PCA analysis revealed a separation of the representative metabolites. Ellipse represents 90% confidence intervals for the PSS and static groups, respectively. (E) Biosynthesis of MUFA depicts that SCD1 catalyzes the rate limiting step for the conversion of saturated FA (palmitic and stearic) to monounsaturated FA (palmitoleic and oleic). (F) Compound correlation network was generated with Cytoscape software. SCD1-mediated metabolites are interconnected with the glycolytic metabolites. Organic layout was used to organize the network according to major functional classes. The cluster predominantly involved with metabolites and showed significantly changed and are indicated in green nodes (palmitate, oleic acid and azelaic acid). A highly connected network within the metabolites cluster reveals the effect of exercise on mice highlighting the interactions with desaturase metabolism and other pathways.

2.4.2 Exercise-augmented PSS mitigated flow recirculation in the aortic arch.

The moving boundary versus stationary wall simulation was performed on mice in sedentary condition as was described in methods and the results were compared to capture the effect of moving boundary on the flow patterns (Figure 2.5 a, b). Our simulation demonstrated the peak of the velocity magnitude profile proximal to the greater curvature, and low WSS at the lesser curvature that is demonstrated by velocity-colored streamlines and time-averaged wall shear stress contours (Figure 2.5 a, b). We observed flow reversal and recirculation at the lesser curvature of the aortic arch exposing the endothelial cells to oscillatory shear stress especially during systole. To quantify the effect of moving boundary simulation on the results, the aortic arch was divided into 4 sections: greater curvature, ascending aorta, lesser curvature, descending aorta. The oscillatory shear index and time-averaged wall shear stress were compared between these regions in moving-boundary and stationery-wall simulation models (Figure 2.5 c). Our results indicate that considering the motion and contraction of the vessel wall reduces the estimated TAWSS in all the regions. The OSI comparison between the moving boundary and stationary wall simulations shows that OSI increases as a result of applying the motion of the vessel in the model. Overall, both TAWSS and OSI comparisons indicate that in a more realistic simulation (moving boundary), the vessel wall is exposed to a more atheroprone hemodynamics situation.

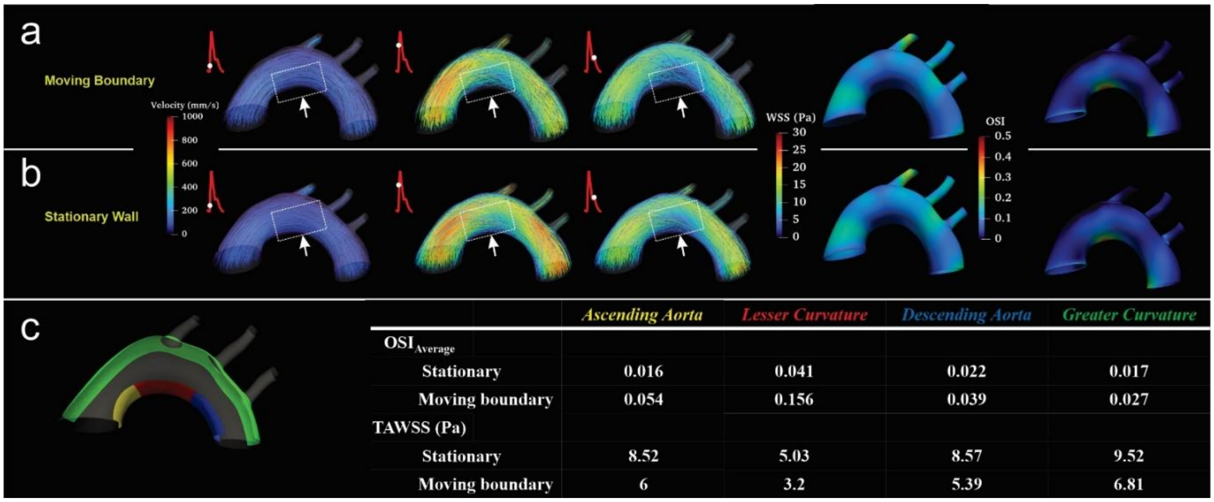

	Ascending Aorta	Lesser Curvature	Descending Aorta	Greater Curvature
$OSI_{Average}$				
Stationary	0.016	0.041	0.022	0.017
Moving boundary	0.054	0.156	0.039	0.027
TAWSS (Pa)				
Stationary	8.52	5.03	8.57	9.52
Moving boundary	6	3.2	5.39	6.81

Figure 2.3. In silico analysis of blood flow in aortic arch in moving boundary versus stationary wall models. 4-D CFD simulation was performed to analyze hemodynamic profiles in the

mouse aorta in response to exercise. (a) velocity-colored streamlines in the moving boundary model at 3 time-points in a cardiac cycle (left), TAWSS contour (middle), and OSI in moving boundary and (b) stationary wall simulations. (C) The comparison between TAWSS and OSI in 4 different regions of the aortic arch. The stationary wall simulation overestimates TAWSS and underestimates OSI in aortic arch of mouse.

Pulse-wave doppler was performed at the proximal section of the descending aorta to validate the results acquired from CFD simulation (Figure 2.4 a). The velocity profile proximal to lesser curvature of the descending aorta shows dicrotic notch and retrograde flow through each cardiac cycle. We defined a probe at a similar location on the stationary wall and moving boundary CFD models to compare the velocity variation in time (Figure 2.4 b, c). Our results show that unlike stationary wall model, moving boundary simulation can capture the dicrotic notch in systole. The secondary peak on the moving boundary velocity profile represents the reflection wave and the time difference between pulse arrival between proximal and distal regions of the aorta.

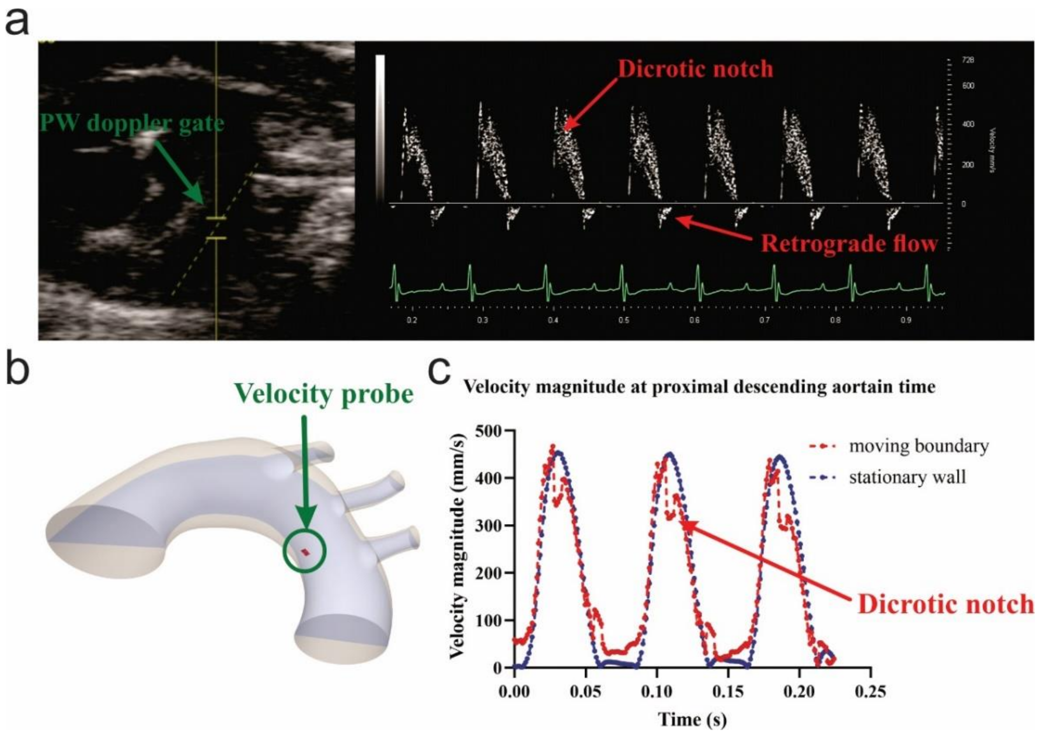

Figure 2.4. A validation study between pulse wave doppler acquired data and CFD simulation (a) Pulse wave doppler performed at lesser curvature of the proximal descending aorta (b) the probe location used for averaging the velocity magnitude profile in CFD models (c) the velocity profile captured using the stationary wall and moving boundary simulations. The moving boundary simulation is able to capture the dicrotic notch and secondary wave in systole.

We further simulated the exercise-augmented blood flow by applying the heart rate and flow rate variation to the model (Figure 2.5). The comparison between sedentary (No EX) and voluntary wheel running conditions indicated an overall increase in TAWSS at the aortic arch when comparing different regions of the aorta. Our results also showed mitigation of the flow recirculation zone at the lesser curvature of the aortic arch in exercise. The comparison between sedentary and exercise models indicated increased OSI levels at the lesser curvature of the aortic arch although exercise reduced OSI in the rest of the regions. While it remains experimentally challenging to acquire real-time hemodynamic profiles, our *in-silico* analysis supports the notion that exercise modulates Pulsatile shear stress to mitigate flow recirculation in the disturbed flow-prone lesser curvature.

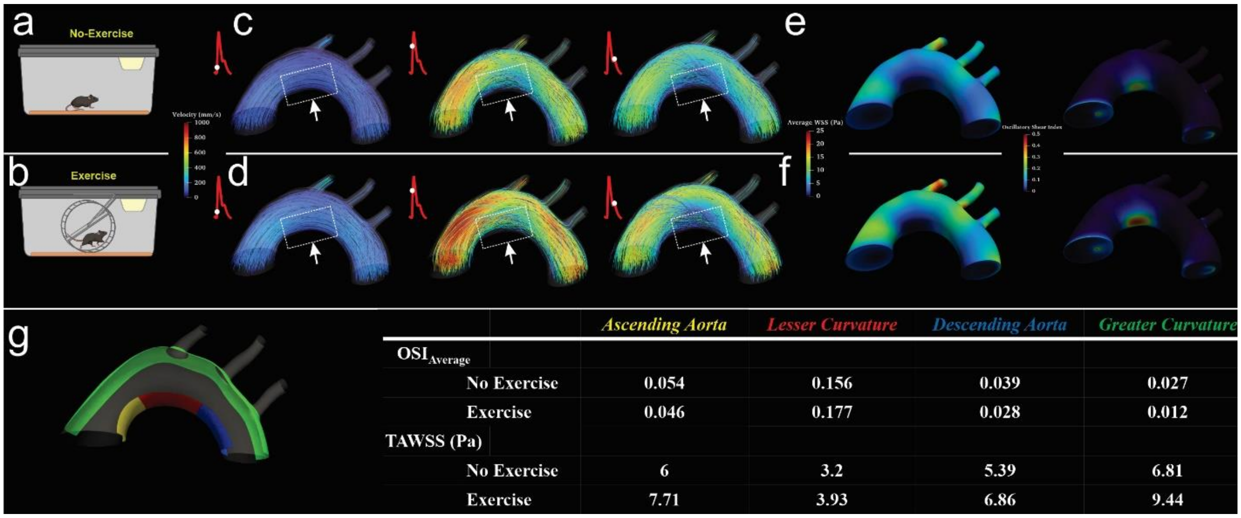

	Ascending Aorta	Lesser Curvature	Descending Aorta	Greater Curvature
$OSI_{Average}$				
No Exercise	0.054	0.156	0.039	0.027
Exercise	0.046	0.177	0.028	0.012
TAWSS (Pa)				
No Exercise	6	3.2	5.39	6.81
Exercise	7.71	3.93	6.86	9.44

Figure 2.5. In silico analysis of exercise-augmented PSS. 4-D CFD simulation was performed to analyze hemodynamic profiles in the mouse aorta in response to exercise. (a, b) Schematic of mouse at sedentary condition (top) and engaging in voluntary wheel running (bottom). (c, d) Velocity-colored streamlines along the aortic arch demonstrating disturbed flow developed at the lesser curvature, whereas exercise-augmented shear stress mitigates flow recirculation at the disturbed flow-prone lesser curvature. (e, f) TAWSS and OSI contours captured over several cardiac cycles were computed and compared between no exercise and voluntary wheel running. Note that pulsatile shear stress develops at the greater curvature of the aortic arch and descending aorta, whereas disturbed flow, including oscillatory shear stress, develops at the lesser curvature. Exercise-augmented pulsatile shear stress mitigates disturbed flow at the lesser curvature. (g) Comparison between OSI and TAWSS across color-coded regions of the lesser and greater aortic curvature, with or without exercise.

2.4.3 Exercise activated endothelial SCD1 in the ER to catalyze lipid metabolites

Wild-type C57BL/6J mice were subjected to voluntary wheel running to recapitulate exercise-augmented PSS (Figure 2.6 A, B). Plasma samples were collected at baseline and after 24 h of exercise. Untargeted metabolomic analysis revealed that OA was markedly increased, while PA exhibited an increasing trend although it did not reach the level of statistical significance (Figure 2.6 C, E). Saturated palmitic and stearic acids were unchanged (Figure 2.6 D). PCA revealed a distinct separation of lipid metabolites after exercise (Figure 2.6 F). Consistent with the finding in PSS-induced HAECs, PSS increased glycolytic metabolites including lactate, fumarate, oxalate, and succinate, as previously reported [71] (Figure S3.1 A).

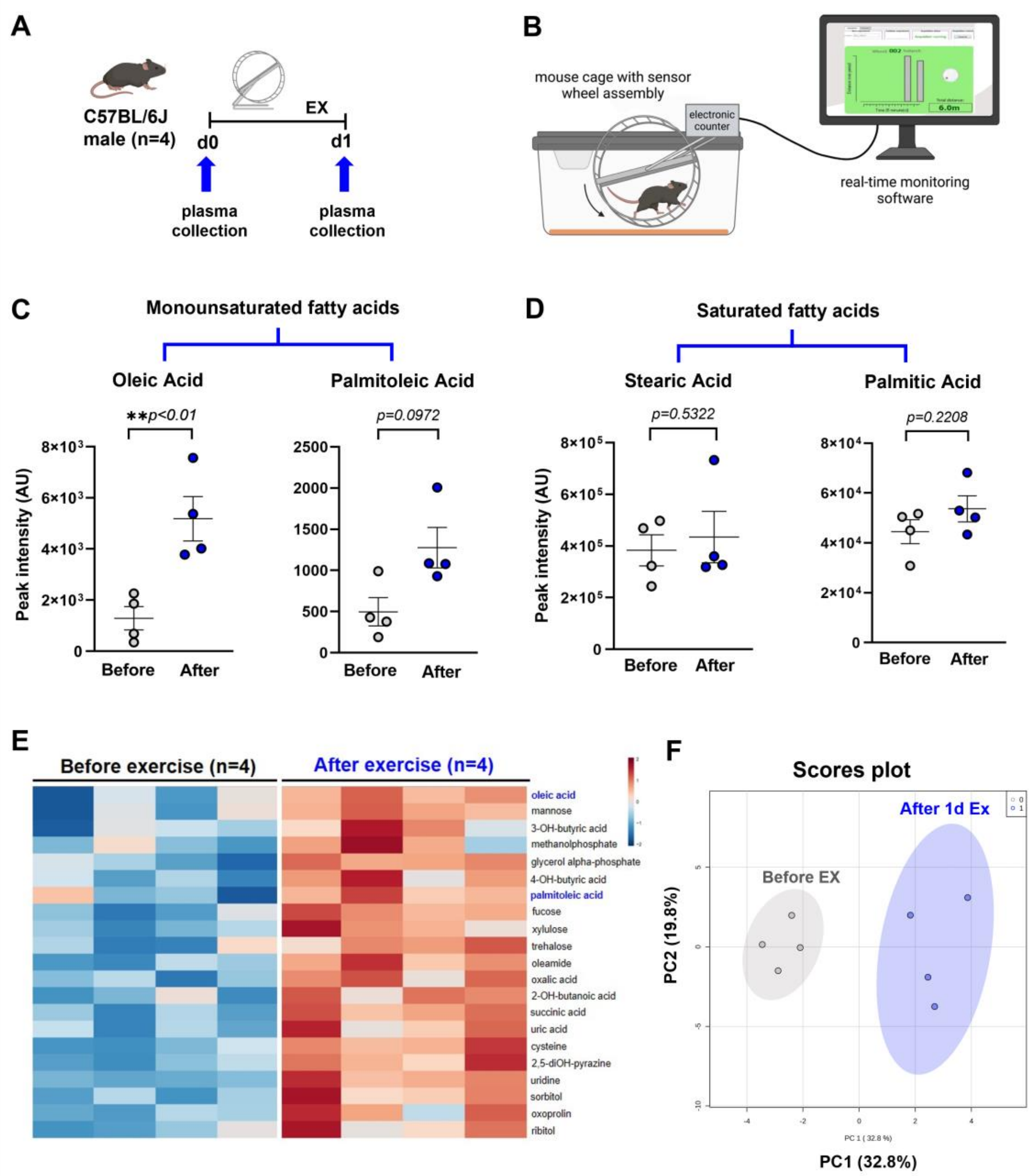

Figure 2.6. Exercise activates SCD1 to catalyze lipid metabolites. (A) A schematic representation of the animal exercise protocol. Plasma was collected from male wild-type C57BL/6J before and after 24 h of voluntary wheel running for metabolomic analysis (n=4 mice for each group). (B) The voluntary wheel running system provided real-time monitoring of rodent running activity (figure generated with Bio render). (C) 24 hours of exercise increased oleic, palmitoleic and linoleic acids; however, the latter two metabolites did not reach statistical significance (oleic acid: ***p* < 0.01 vs. before exercise, n=4). (D) Exercise did not change the

plasma levels of saturated FA stearic and palmitic acid. (E) Heatmap of plasma metabolites before and after exercise reveals that OA was elevated in all 4 mice after normalization and scaling using the Pareto method. (F) Score plots by the principal component analysis support the 90% confidence intervals before and after exercise.

We next performed *in situ* hybridization (RNAScope) with a *Scd1*-specific probe, revealing prominent *Scd1* mRNA expression in the endothelial layer of both the aortic arch and descending aorta after 2 weeks of exercise (Figure 2.7 A-C). *En face* immunostaining of the exposed aortic endothelium demonstrated an increase in the perinuclear expression of SCD1 but was absent in *Scd1*$^{EC-/-}$ mice (Figure 2.7 D, E), supporting the subcellular localization of SCD1 in the ER. Changes in body weight and exercise parameters were quantified for both female and male C57BL/6J mice (Figure S3.1 B). Taken together, our findings support the interpretation that exercise-augmented PSS up-regulates SCD1 in the endothelial ER to catalyze lipid metabolites. Furthermore, our *in vitro* and *in vivo* findings support the previous report that PSS-activated *Scd1* is a *Ppar*γ target gene [60] (see Figure S3.2 A-E).

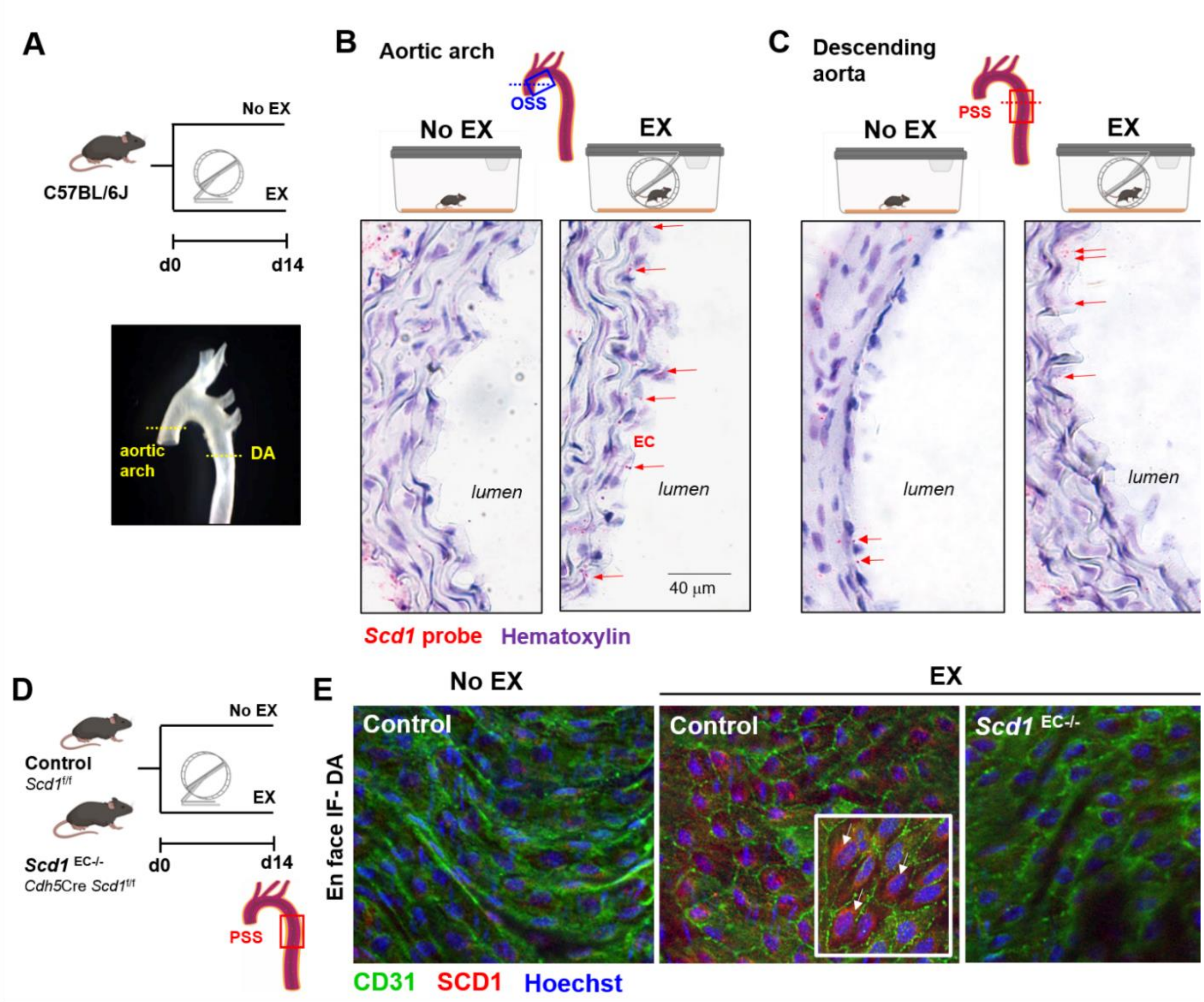

Figure 2.7. Exercise activates endothelial SCD1 in the endoplasmic reticulum (ER). (A) Wild type C57/BL6J mice underwent 14-day voluntary wheel running protocol. The aortas were processed for transversal cryosections at the level of the aortic arch and the descending aorta (DA). (B and C) The *Scd1*-specific probe (RuneScape) demonstrates prominent endothelial staining following 14 days of exercise-induced PSS both in the flow-disturbed aortic arch (B) and the DA (C). Red dots (arrows) indicate the mRNA molecules in the intima layer. *Scd1* was also present in some smooth muscle cells and periaortic adventitia (adv) in both groups. Microphotographs were taken at 63X magnification. (D) The endothelial-specific *Scd1* deleted mice underwent the 14-day exercise protocol. (E) *En face* immunostaining of exposed aortic endothelium reveals that exercise increased the SCD1 expression (red) in the aortic endothelial cells (CD31+, green) (n=3). A higher magnification image (63X: right lower corner insert)

showed perinuclear SCD1 staining (arrows), supporting the subcellular localization of SCD1 in the ER. No staining was observed in the *Scd1* $^{EC-/-}$ mice undergoing exercise.

2.4.4 Endothelial-specific SCD1 deletion abrogates the SCD1-mitigated anti-inflammation and atherosclerosis in the disturbed flow-prone aortic arch

Ldlr$^{-/-}$ mice with or without conditional deletion of the *Scd1* gene upon Cre-mediated recombination were generated under the endothelial-specific promoter Cdh5 (VE-cadherin) (*Ldlr*$^{-/-}$*Scd1*$^{EC\ -/-}$) [65]. Mice received high-fat diet (HFD) for 28 days to promote the development of fatty streak in the aorta [75]. After the first 14 days of HFD, some mice underwent voluntary wheel running for 14 days while continuing on HFD (HFD-EX) (Figure 2.8 A). Body weight gain and exercise data are included in Figure S3.3.

On day 28, quantitative and targeted metabolomic analyses revealed that the basal levels of OA and PA in plasma were reduced in the *Ldlr*$^{-/-}$*Scd1*$^{EC\ -/-}$mice as compared to *Ldlr*$^{-/-}$ alone. After exercise, both OA and PA levels were significantly elevated in the *Ldlr*$^{-/-}$ but not in the *Ldlr*$^{-/-}$*Scd1*$^{EC-/-}$mice (Figure 2.8 B, C, Figure S3.4)**.** This finding confirms that endothelial-specific *Scd1* deletion abrogates exercise-activated lipid metabolites, including OA and PA. In addition, a subset of metabolites was differentially modulated under our experimental conditions (Figure 2.8 D).

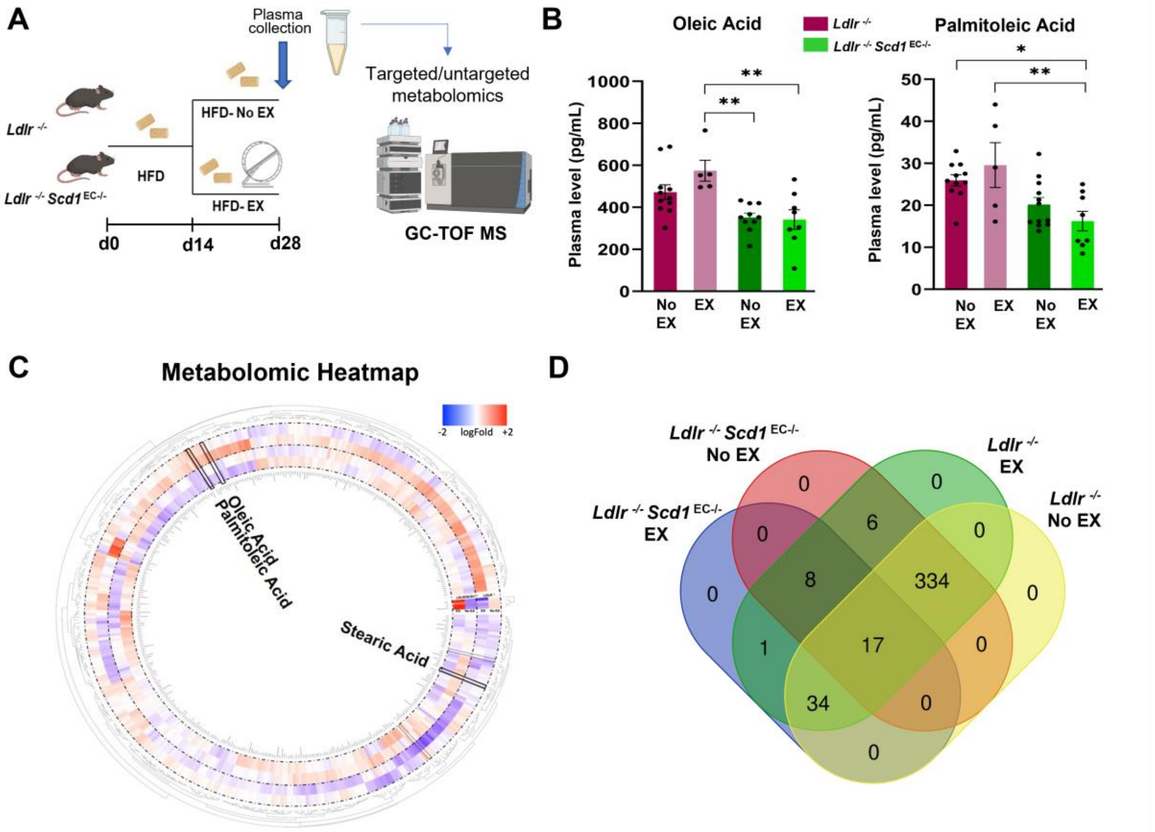

Figure 2.8. Exercise-mediated lipid metabolites, OA and PA, are reduced in mice with endothelial-specific SCD1 deletion. (A) The exercise protocol depicts the *Ldlr*$^{-/-}$ mice that were crossed with *Cdh5Cre*; *Scd1*$^{\text{flox/flox}}$ to generate endothelial-specific SCD1 deletion (*Ldlr*$^{-/-}$*Scd1*$^{\text{EC-/-}}$). Adult mice at 8 weeks received HFD for 14 days. The mice were then divided into exercise (EX) and no exercise (No EX) groups for an additional 14 days of exercise. (B) The absolute plasma concentration of OA was elevated after exercise in the *Ldlr*$^{-/-}$ mice, whereas OA concentration was reduced and remained reduced after exercise in the *Ldlr*$^{-/-}$*Scd1*$^{\text{EC-/-}}$ mice. The plasma concentration of PA also followed the similar trends, suggesting that exercise activates SCD1 to catalyze OA and PA (*$p < 0.05$, $p < 0.01$; n=4-12; each dot represents an individual animal). (C) Circular heatmap of untargeted metabolomic analysis capturing known and unknown ID metabolites highlights changes in OA and PA further supporting that SCD1 deletion resulted in a decrease in both OA and PA, after normalization and scaling using the Pareto method. Circular heatmap was generated with Circus R package. (D) Venn diagram was

generated with webtools Venn, and it summarizes the shared metabolites among different conditions.

Ultrasound-based 4-D CFD simulation revealed disturbed flow along the inner curvature of the aortic arch, whereas pulsatile flow was prominent in the thoracic region of the descending aorta **(**Figure 2.9 A and Figure S3.5). Confocal imaging of the aortic endothelium *en face* after immunostaining with anti-ERG (an endothelial nuclear marker) [76] and VCAM1 (an early atherosclerosis lesion marker) [77] revealed the presence of VCAM1 expression in the disturbed flow-prone inner curvature of the aortic arch in *Ldlr*$^{-/-}$ mice. *Ldlr*$^{-/-}$ mice with endothelial-specific *Scd1* deletion (*Scd1*$^{EC-/-}$) also displayed VCAM1 expression in the inner curvature. However, the 14-day exercise period mitigated levels of VCAM1 expression in *Ldlr*$^{-/-}$, but not in *Ldlr*$^{-/-}$ *Scd1*$^{EC-/-}$ mice (Figure 2.9 B)**.** In the descending aorta, where the endothelium is exposed to PSS, deletion of endothelial *Scd1* led to an increase in VCAM1-positive endothelial cells compared to *Ldlr*$^{-/-}$ mice, and exercise did not mitigate the number of VCAM1 positive endothelial cells (Figure 2.9 C)*.* *In situ* hybridization with a *Scd1*-specific probe corroborated prominent endothelial staining following exercise-induced PSS in the disturbed flow-prone aortic arch of *Ldlr*$^{-/-}$ mice, which is absent in *Ldlr*$^{-/-}$*Scd1*$^{EC-/-}$ mice (Figure 2.9 E). Taken together, exercise-augmented PSS is implicated in activating endothelial SCD1 for atheroprotection in the disturbed flow-prone vasculature.

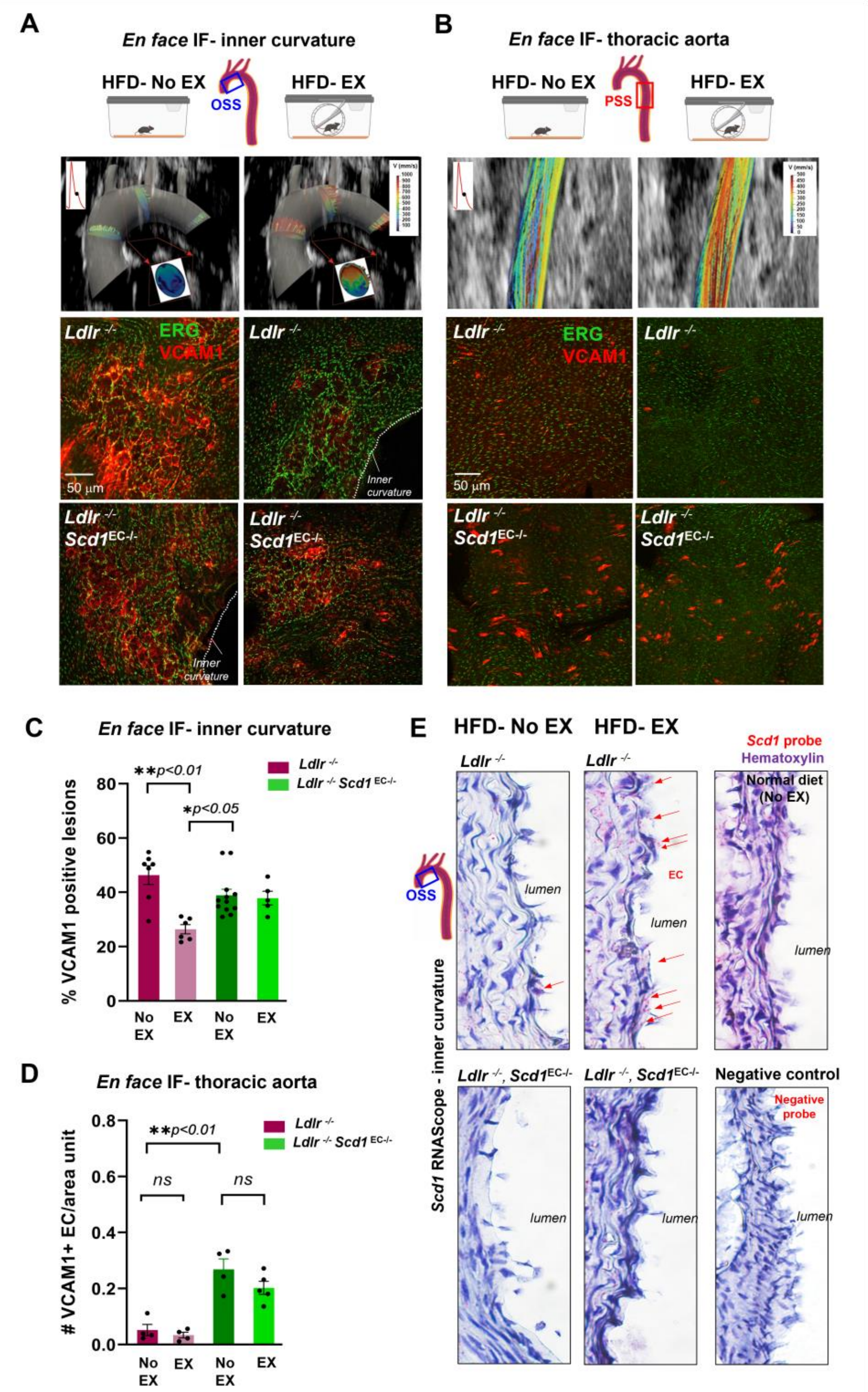

Figure 2.9. Endothelial-specific SCD1 deletion abrogates exercise-mediated anti-inflammatory mediators. (A and B) CFD simulates the spatial and temporal variations in wall shear stress in the aortic arch and descending aorta of a representative wild-type mouse. The ultrasound B-mode was used to reconstruct the 4D shear stress profiles. The cross-sections of the aortic

arch illustrate the high shear stress localized to the greater curvature and low shear stress to the lesser curvature. Exercise-augmented shear stress mitigates disturbed flow at the lesser curvature. The CFD reconstruction over a cardiac a cardiac cycle (t1, t2, and t3) is included in Supplemental Figure 4; only t2 is depicted here. The colored streamlines indicate the CFD-derived velocity profiles along the aortic arch. The representative confocal Z-stack for the maximal projection of en face immunostaining with anti-ERG and anti-VCAM-1 in the inner curvature of the aortic arch and the thoracic region of the descending aorta. In the lesser curvature, the VCAM-1 staining was attenuated following exercise in the Ldlr-/- mice but remained prominent in the Ldlr-/-Scd1EC-/- mice. In the thoracic aorta, the VCAM-1 staining was reduced with or without exercise in the Ldlr-/- mice but were elevated with or without exercise in the Ldlr-/-Scd1EC-/- mice. This finding further supports the interpretation that PSS activates endothelial SCD1 to mitigate arterial inflammation. (C and D) Quantification of en face immunostaining shown in A and B panels, respectively. Each dot corresponds to an individual animal (n=4-12); both the male and female data were pooled together. (E) The SCD1-specific probe (RuneScape) corroborates prominent endothelial staining following exercise-augmented PSS in the disturbed flow-prone aortic arch in Ldlr-/- mice, which is absent in Ldlr-/-Scd1EC-/- mice. Scd1 expression remains unchanged after HFD as compared to normal chow diet. Red dots (arrows) indicate the mRNA molecules in the intima layer. Staining with a negative control probe shows complete absence of red positive dots. Microphotographs were taken at 63X magnification.

2.4.5 SCD1-catalyzed oleic acid mitigates pro-inflammatory and ER stress mediators.

We assessed the effects of OA on cultured HAECs in terms of *Vcam1*, *Icam1*, *Mcp1*, *Esel* (E-selectin) and the *Cxcl8* chemokine mRNA expression (Figure 2.10 A). OA reduced these pro-inflammatory mediators in a dose-dependent manner [77-79]. Also, OA decreased the expression of ER stress-related transcription factors, *Atf3*, *Atf4*, and *Atf6* (Figure S3.6). These changes are consistent with our analysis of total liver gene expression after 14 days of exercise (Figure S3.7). Furthermore, a recombinant adenovirus-based system was developed to overexpress SCD1 in HAECs via the *Cdh5* (CD144) promoter, which was validated by immunofluorescence (IF) and Western Blot. SCD1 overexpression mitigated inflammatory mediators in HAECs, such as *Cxcl8* and its receptor *Cxcr1* and the olfactory receptor 2 (*Or6a2)* [80, 81] (Figure 2.10 B-D).

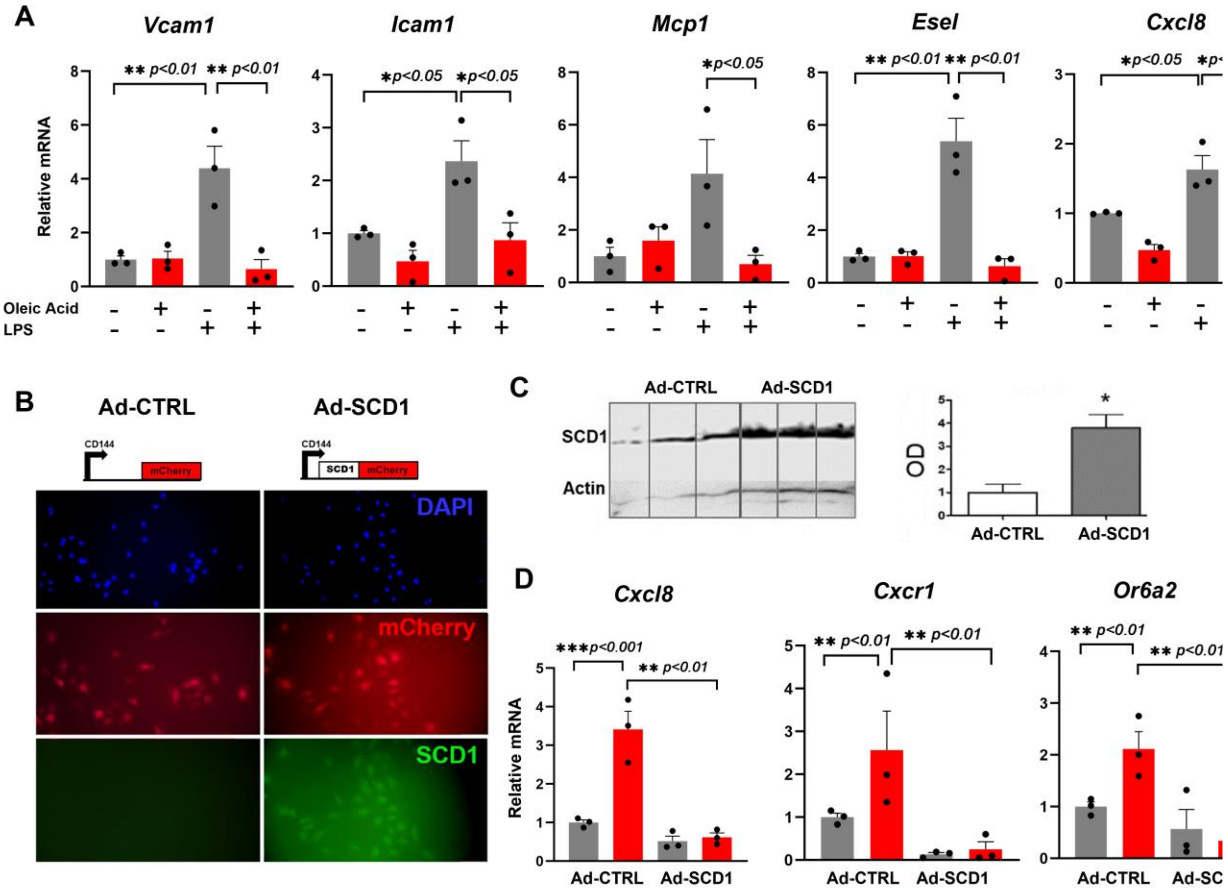

Figure 2.10. Oleic acid treatment or SCD1 overexpression mitigate pro-inflammatory mediators in HAECs. (A) HAECs monolayers were treated for 4 hours with OA at 0.2 mM in the absence or presence of LPS (20 ng/mL) and gene expression levels were analyzed by qRT-PCR. (B) HAECs were infected with adenovirus control (left panels) or SCD1 (right panels) and imaged for mCherry reporter and SCD1 expression. (C) Western Blot was performed and quantified. (D) Ad-SCD1 mitigated the LPS (20 ng/mL)-induced expression (4 hr.) of Cxcl8, Cxcr1 and Or6a2 (n=3, *p<0.05, **p<0.01, ***p<0.001).

2.4.6 *Scd1* and gene interaction networks in response to biomechanical forces through single cell transcriptomic analysis of the mouse aorta

To further assess transcriptomic profiles of exercise-mediated endothelial gene expression in the aorta, we performed single-cell RNA sequencing on aortas from *Ldlr*$^{-/-}$ mice subjected to the following treatments for 4 weeks: 1) normal chow diet; 2) HFD; 3) HFD + EX (Figure 2.11 A). Unbiased clustering analysis of transcriptional profiles identified 7 lineages based on cell-type specific markers (Figure 2.11 B, C, Figure S3.8). 3D Volcano Plot further established *Scd1* as a gene differentially modulated by exercise in the aortic endothelium (Figure 2.11 D). As a corollary, by integrating our endothelial transcriptomic data with a published database [82] using Cytoscape we uncovered potential candidate genes interacting with *Scd1* in ECs, including adiponectin receptor 2 (*Adipor2*) [83], peroxisomal acyl-coenzyme A oxidase 1 (*Acox1*) [84, 85] and insulin receptor substrate 2 (*Irs2*) [86-88] (Figure 2.11 E). Furthermore, gene- metabolite interconnection networks revealed a relationship between *Scd1* and the *Acsl* family of long-chain acyl CoA synthetase genes and acyl-CoA thioesterase genes (*Acot*), which are involved in intracellular lipid metabolism.

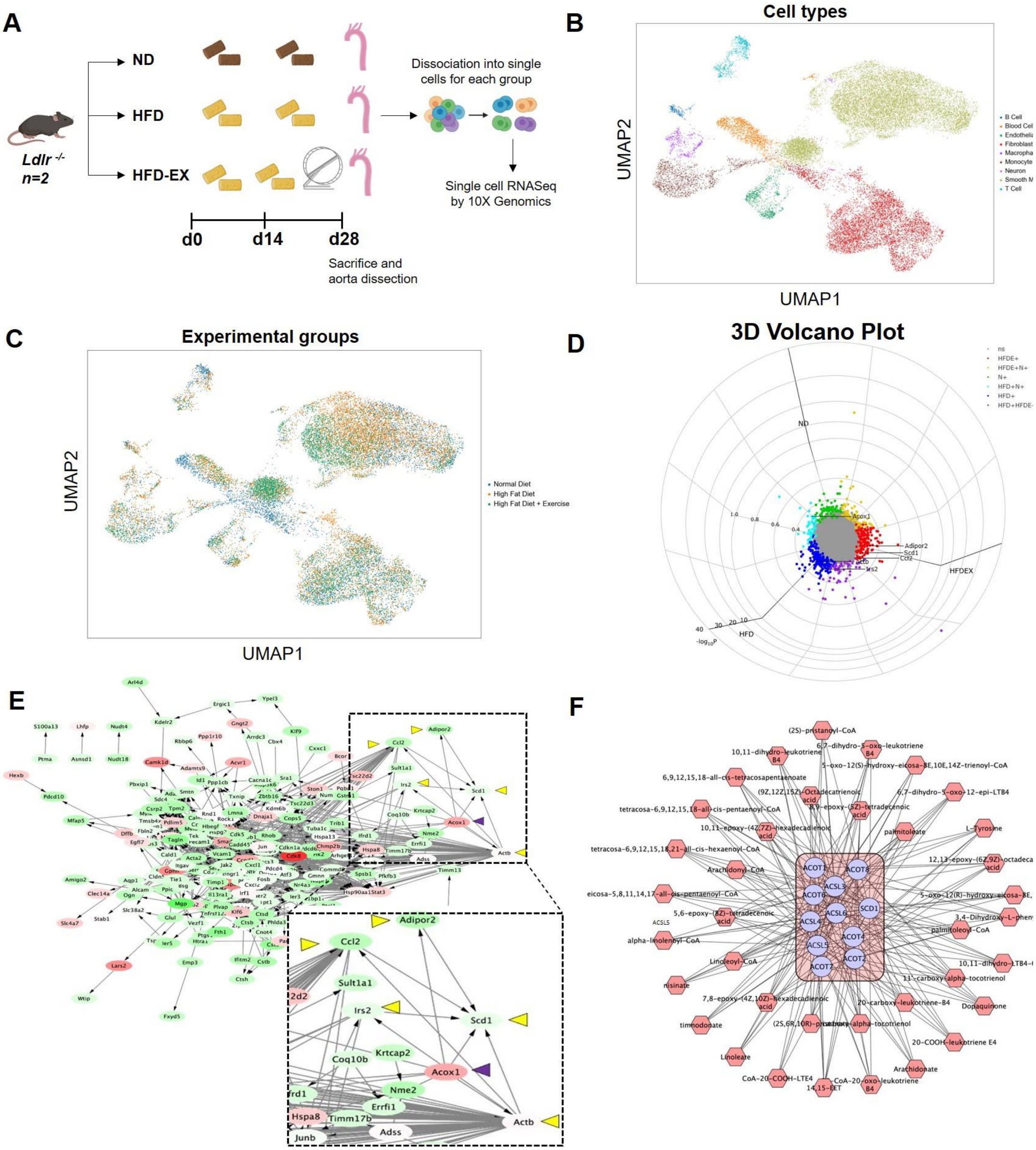

Figure 2.11. Single cell transcriptomics of mouse aorta and network interactions. Schematic diagram of the experimental protocol. *Ldlr*$^{-/-}$ mice (n=2 per group) were subjected to normal chow diet (ND, Control), HFD or HFD plus exercise (HFD-EX) during the last 2 weeks of the treatment. Aortas were collected after 28 days. A total of 20,000 cells were analyzed. (B and

C) Representative UMAP of cellular clusters in the mouse aorta. (D) 3D cylindrical volcano plot of differentially expressed genes comparing ND vs HFD vs HFD-EX was created by using Volcano 3D R package. Vectors for sample mean Z score per gene were projected onto a polar coordinate space analogous to RGB (red-green-blue) color space mapping to HSV (hue-saturation-value) as described in [89]. (E) Gene network generated with Cytoscape software from EC transcriptomics and published database of mechanosensitive genes [82]. (F) Analysis of interaction networks between endothelial transcriptomic and plasma metabolomics data highlighting the connection of *Scd1*, *Acsl* and *Acot* gene families with several exercise-induced metabolites.

Our CFD analysis indicated that the lesser curvature of the aortic arch is exposed to oscillatory shear stress (Figure 2.5) and was confirmed by our immunostaining showing upregulation of Vcam1 (inflammation) and downregulation of Scd1 (cardioprotective) as a result of low magnitude oscillatory shear stress in this region (Figure 2.9). On the other hand, exercise was revealed to play a major role in determining the Scd1 levels either in aortic arch or thoracic aorta (Figure 2.9). We isolated the EC group in our transcriptomics dataset and assessed the extent to which each of these factors contribute to cell clustering. The comparison between EC subclusters (Figure 2.12 a) and treatment groups (Figure 2.12 b, e) reveals that the HFD and EX treatment are not the main factors involved in separation of the cells on the UMAP plot despite observed variations in mechanosensitive gene expressions (Figure 2.11). These results suggests that the separation between endothelial subclusters is due to spatial variations in WSS. By Comparing the Scd1 and Vcam1 gene expressions in different clusters, we observe inverse coexpression in some of the subclusters (subcluster #2, 7, 8) proving confirming the role of local hemodynamic forces in overall transcriptomics of the cells. The comparison between Scd1 and Vcam1 positive cell population plus normalized mean gene expression suggests that the local WSS variation changes both the population of activated cells and mean gene expression (Figure 2.12).

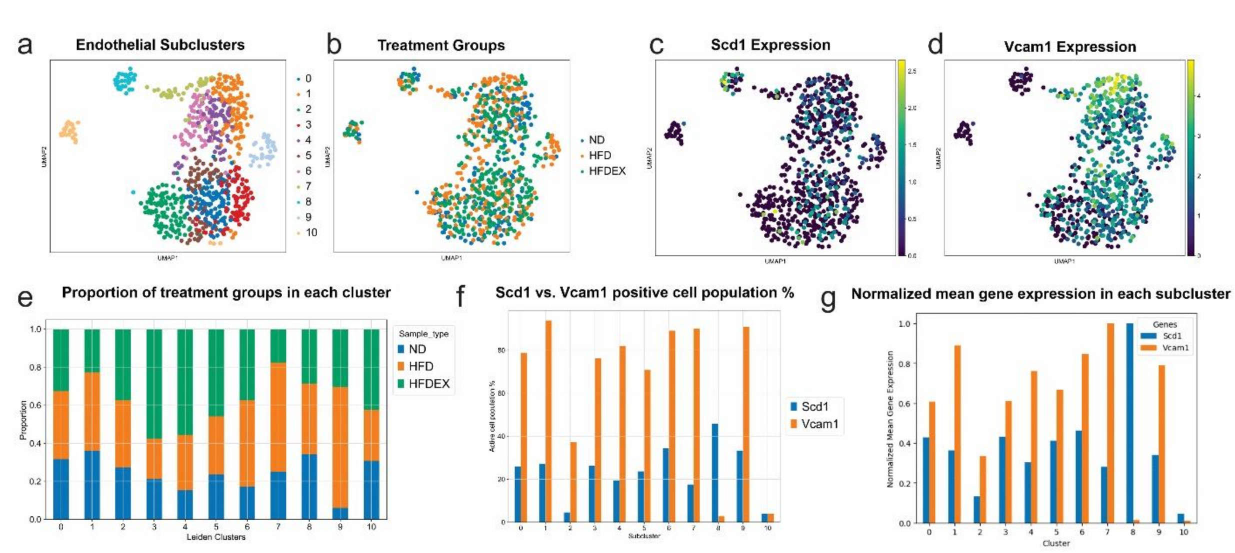

Figure 2.12. scRNA analysis on endothelial subclusters to assess Scd1 and Vcam1 co-expression. (a) Endothelial subcluster divided into 11 distinct groups depending on the gene expression patterns colored by clusters (b) Endothelial cells colored by treatment groups including normal diet , high-fat diet, and high-fat diet + exercise (c) Endothelial cells colored by Scd1 expression and (d) Vcam1 expression levels (e) The proportion of each treatment group in each of the subclusters of the endothelial cells (f) The comparison between the Scd1 and Vcam1 positive cell population in each of the subclusters of the endothelial cells (g) The comparison between Scd1 and Vcam1 mean gene expression levels in each of the subclusters normalized by maximum mean gene expression

2.5 Discussion

Vascular diseases, including coronary artery disease, stroke, and PAD, predispose individuals to develop chronic disability and increase the healthcare burden [90]. Exercise intervention is an effective lifestyle modification to ameliorate cardiometabolic disease, however, the underlying flow-sensitive metabolomic transducers that act to ameliorate disease are not completely known. In this study, we demonstrate how exercise activates SCD1 to catalyze vascular protective lipid metabolites in the disturbed flow-prone region of the aortic arch. By integrating our dynamic flow system, metabolomic analyses, ultrasound imaging to reconstruct computational domain for CFD, and wheel running system, we demonstrated that exercise augments PSS (TAWSS and OSI) to activate endothelial SCD1 in the disturbed flow-prone aortic arch (Figure 2.13). Furthermore, endothelial-specific SCD1 deletion or overexpression established that exercise-activated SCD1 catalyzes the lipid metabolite, oleic acid, to attenuate inflammatory and atherosclerotic mediators in the lesser curvature of the aortic arch.

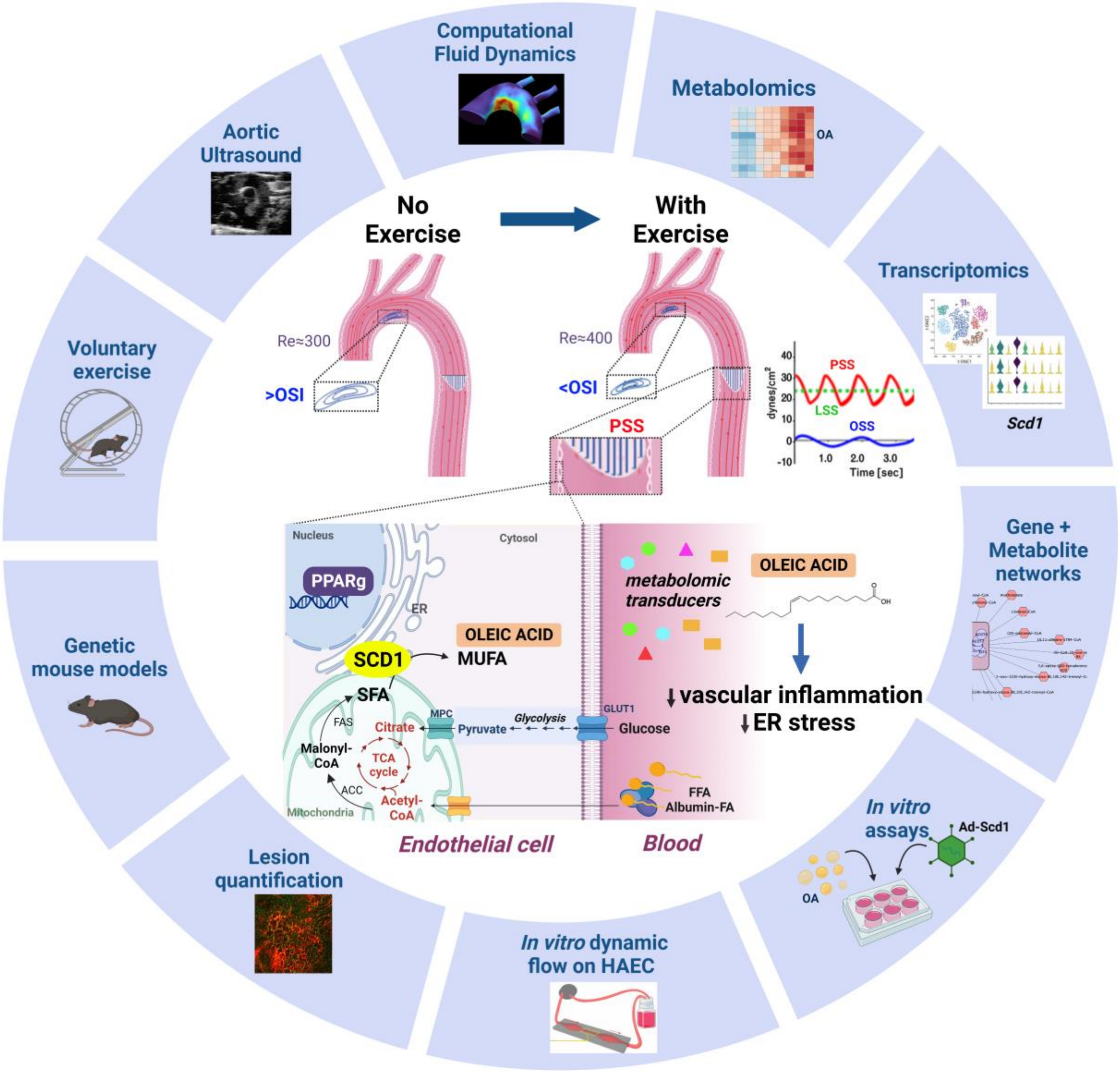

Figure 2.13. Working model for exercise-induced PSS in the aorta and activation of the flow-responsive PPARγ-SCD1 pathway for aortic gastroprotection. Exercise-induced PSS reduces flow recirculation and OSI in the aortic arch. At the cellular level, shear stress-mediated glycolytic flux yields pyruvate as a substrate for FA metabolism. EC can uptake and metabolize either free fatty acids (FFA) or albumin-bound FAs. SCD1 located in the ER membrane adjacent to the mitochondrial membrane is the limiting step in the conversion of SFA into MUFA. The SCD1 product oleic acid reduces NF-κB-induced inflammation and ER stress genes. MPC:

mitochondrial pyruvate carrier; TCA: tricarboxylic acid. ACC: acetyl-CoA carboxylase; FAS: fatty acid synthase; Re; Reynolds number. Figure was generated with Bio render.

Endothelial cells line the lumen of the vasculature and regulate the transport of oxygen and nutrients. Hemodynamic shear stress modulates cell metabolism to maintain endothelial homeostasis [91, 92], and PSS is well-recognized to be atheroprotective, by attenuating pro-inflammatory mediators and NADPH oxidase system [47, 49, 93, 94]. To identify PSS-mediated endothelial metabolites, we seeded the HAECs in our custom-designed in vitro flow system to mimic the spatial and temporal variations in WSS. Our metabolomic analysis showed that PSS increased SCD1-catalyzed fatty acid metabolites in HAECs, and this observation guided us to investigate exercise-activated SCD1 as a metabolomic transducer to mitigate inflammatory mediators and ER stress.

SCD1 is an enzyme anchored in the ER that catalyzes the conversion of saturated long-chain fatty acids, palmitic (16:0) and stearic (18:0), to MUFAs palmitoleic (16:1) and oleic (18:1). The resulting MUFAs are the major components of triglycerides, cholesterol esters, and phospholipids [61, 95]. Using subcellular fractioning, previous studies indicated that SCD1 is localized in the mitochondria-associated membrane (MAM), a specific region of the ER in close proximity to the outer mitochondrial membrane that is enriched in enzymes responsible for phospholipid and triglyceride biosynthesis [96]. SCD1 is expressed in a broad range of tissues and at high levels in the insulin-sensitive hepatocytes and white and brown adipocytes [63, 97]. Other tissue-specific SCD isoforms have also been identified, including SCD2, which is found mainly in the brain [98], SCD3 in the skin and sebaceous gland [99] and SCD4 in the heart [100]. However, endothelial SCD1 has not been explored *in vivo*, primarily because of experimental challenges and low basal expression compared to highly metabolically active tissues.

The expression of SCD isoforms is highly regulated by multiple factors, including diets and hormones [101]. SCD1 is expressed in multiple organs and tissues to catalyze lipid metabolites in association with adipose, cancer cell, and skeletal muscle metabolism, as well as liver and lung fibrosis [102-104]. Global deficiency of SCD1 results in reduced adiposity, increased insulin sensitivity, and resistance to diet-induced obesity [105]. Interestingly, the global deletion of SCD1 in *Ldlr* null mice leads to abnormal lipid metabolism, ER stress, and atherosclerosis [106]. Furthermore, hand grip strength, duration of swimming time to exhaustion, and voluntary vs. forced treadmill wheel running support the notion that SCD1 overexpression increases cardiovascular endurance in mouse models [107].

In this context, we developed the endothelial-specific *Scd1* deletion in *Ldlr* null mice. During exercise, autonomic function elevates both blood pressure (BP) and heart rate (HR); thus, leading to increased blood flow and shear stress [108]. By deploying micro shear stress sensors into the rabbit aorta, we demonstrated a positive correlation between BP/HR and pulsatile shear stress [109]. Accordingly, wild-type mice undergoing 2 weeks of wheel running developed PSS-activated endothelial SCD1 expression, as evidenced by in situ hybridization and *en face* immunostaining of the aortas. This data indicates that exercise-augmented PSS activates endothelial SCD1 expression.

The cardiovascular benefits of exercise have been well-documented to improve endothelial function and ameliorate both vascular inflammation and oxidative stress [110]. Exercise elevates the plasma levels of serum clustering that increases plasticity and reduces inflammation in the cerebrovascular system [45]. Recently, exercise was reported to increase both the human and racehorse plasma metabolite, *N*-lactoyl-phenylalanine (Lac-Phe), which also suppressed feeding and obesity in mice [111].

Despite these salutary effects, regular exercise is limited to certain populations due to physical disabilities and/or socioeconomic limitations [112].The prevalence of sedentary lifestyles remains high in industrialized nations, including the United States. To tackle this problem, the National Institutes of Health launched the Molecular Transducers of Physical Activity Consortium (MoTrPAC) with the aim to integrate large-scale multi-omic analyses with bioinformatics to identify molecular transducers as pharmacologic interventions to mimic or enhance the therapeutic effects of exercise [53]. Several signaling pathways have been identified to mediate exercise's benefits, including IGF1/PI3K/AKT, C/EBPβ/CITED4, PPAR family, PGC1α, AMPK, eNOS/NO, and certain noncoding RNAs [113].

PPARs belong to the nuclear receptor superfamily of ligand-activated transcription factors regulating lipid and glucose metabolism, energy homeostasis and inflammation [114]. Previous studies have demonstrated that shear stress induces PPARα, δ and γ to regulate endothelial function [115, 116]. PPARγ agonists belong to the thiazolidinedione class of drugs such as troglitazone and rosiglitazone that attenuate palmitavte-induced ER stress and apoptosis by activating SCD1 induction in macrophages [117]. PPARγ was shown to protect against IL-1β-mediated endothelial dysfunction through a reduction of oxidative stress responses [118] and is essential for preventing aging-associated endothelial dysfunction [119]. Our flow system revealed that PSS-activated SCD1 expression in HAEC was PPARγ-dependent, consistent with the previous report that laminar shear stress upregulated SCD1 through a PPARγ-specific mechanism [60]. To further demonstrate the PPARγ-dependent endothelial SCD1 expression *in vivo*, we subjected transgenic mice expressing the dominant-negative V290M PPARγ mutation (E-V290M Tg) [62] to voluntary wheel running. Immunostaining for SCD1 was absent in the aortic endothelial cells as compared to the wild-type (Figure S3.2 E), corroborating the PPARγ-dependent SCD1 activation.

Ldlr$^{-/-}$ mice fed with HFD develop vascular lesions in a time-dependent manner and have been widely used to mimic human atherosclerosis. The atherosclerotic lesions develop at susceptible regions associated with low shear stress or disturbed flow, such as the inner curvature and branching points of the aorta [120]. Hemodynamic-driven disruptions of the integrity of the arterial intima drive atherogenic inflammation, associated with increased VCAM1 expression, recruitment of Ly6G-positive neutrophils and subsequent accumulation of erythrocyte-derived iron and lipid droplets, which form the incipient atherosclerotic lesions known as fatty streaks [77]. In our study, VCAM1 expression was prominent in the inner curvature of the aorta in *Ldlr*$^{-/-}$ mice after 4 weeks of HFD but absent in the PSS-mediated descending aorta. However, *Ldlr*$^{-/-}$ mice with endothelial-specific SCD1 deletion developed more pronounced VCAM1 positive areas in the descending aorta. After 14 days of exercise, the VCAM1 positive lesions were attenuated in the *Ldlr*$^{-/-}$ but not *Ldlr*$^{-/-}$*Scd1*$^{EC-/-}$ mice, further supporting the notion that exercise-activated SCD1 mitigates inflammatory mediators.

Diets enriched in saturated fatty acids are linked to increased cardiovascular disease risk, whereas monounsaturated fatty acids have been associated with improved cardiovascular outcomes [121]. OA is the predominant MUFA in the Mediterranean diets, including olive oil as the principal source of fat. There is strong evidence for an association between a Mediterranean-style diets and cardiovascular disease protection [122]. Our *in vitro* data with OA treatment in HAECs support previous reports that OA inhibits liposaccharide (LPS)-induced endothelial oxidation [123-125], reduces NF-κB activation [126], and ameliorates insulin resistance [124]. In our study, both OA treatment or SCD1 overexpression in HAECs reduced *Cxcl8* (interleukin-8), a member of the chemokine family with proinflammatory properties through CXCR1 and CXCR2 receptors [80]. In addition, OA reduced the ER stress-related transcription factors. In this context, SCD1 deficiency predisposes the cells to ER stress which activates the unfolded protein response (UPR) by increasing ATF6 production, ER stress-mediated pathways, including BiP, CHOP, HSP90B1, and XBP1 [127-129]. Endothelial SCD1 overexpression further reduced the *Or6a2* expression, for which the murine ortholog *Olfr2* is expressed in the mouse macrophages to promote atherosclerosis [81]. Despite the beneficial effects of SCD1 overexpression *in vitro* in HAECs, a major hurdle for *in vivo* application of this system is sequestration of adenoviruses in the liver sinusoids [130].

As a corollary, our network analysis of endothelial transcriptomic profiles in response to HFD and exercise-induced biomechanical forces uncovered three candidate genes that interact with *Scd1* activity and deserve further mechanistic investigation. *Adipor2* regulates membrane fluidity by maintaining MUFA levels in HEK293 cells through sustained desaturase gene expression [131]. *Acox1* protects against LPS-driven inflammation [84] and *Irs2* regulates eNOS phosphorylation and glucose uptake by skeletal muscle [86-88].

2.6 Conclusion

Exercise-modulated hemodynamic shear stress (PSS: TAWSS and OSI) activates ER transmembrane SCD1 to catalyze vascular protective lipid metabolites in the disturbed flow-prone aortic arch. While SCD1 is associated with lipid metabolism across multiple tissues, we reveal that endothelial-specific SCD1 ameliorates inflammatory mediators and atherosclerosis in the lesser curvature of the aortic arch.

Overall, our comprehensive integration of genetic mouse models, exercise, CFD, light-sheet plaque assessment and bioinformatic network analysis of genes and metabolites provides new insights into the flow-sensitive endothelial transducer SCD1 and identifies lipid metabolites as therapeutic targets to mitigate cardiometabolic syndromes.

2.7 Supporting Information

2.7.1 Plasma and Tissue Collection

At the end of the experimental period, animals were fully anesthetized with isoflurane (VetFlo Vaporizer, Kent Scientific, Torrington, CT) before performing bilateral thoracotomy. Briefly, blood was collected by cardiac puncture with a 25G needle and heparinized syringe, followed by immediate opening of the right atria and transcardiac perfusion of ice-cold phosphate buffered saline solution (PBS) at a rate of 1 mL/min to wash the vasculature. The heart and entire thoracic aorta were dissected and washed in ice-cold PBS. Aortas were fixed for 1 hour in 4% paraformaldehyde (PFA) and transferred to PBS for further dissection. The upper half of the heart was fixed in 4% PFA overnight at 4°C with gentle rotation, followed by cryoprotection in a sucrose gradient and embedding in Optical Cutting Compound (OCT) for posterior cryosectioning and analysis of the aortic valves. The blood samples were maintained in ice until centrifugation was performed for 5 min at 1,000 r.p.m. Plasma was separated and stored at -80°C for metabolomic analysis. For the exercise group, blood samples were collected from the retroorbital plexus of 8-week-old wild-type C57BL/6J mice at baseline and 24 hours after voluntary exercise (n=5 male mice for each group) and processed as described above.

2.7.2 *En Face* Immunostaining of the Aorta

Thoracic aortas were dissected under a stereomicroscope to eliminate the perivascular adventitial fat; thus, allowing for visualization of the carotid, innominate, and subclavian branches of the aortic arch. The aortas were cut longitudinally and pinned down on Petri dishes filled with a 3 mm coating of PDMS (Sylgard 184 Elastomer Kit, Dow Corning Corporation) using minutien pins of 0.1 mm diameter (Fine Science Tools). Aortas were fixed in the open flat conformation for 2-4 additional hours in 4% PFA and washed with PBS following described procedures (1). After permeabilization and blocking with 3% goat serum (Thermo Fisher, catalog # 50062Z) containing 0.3 % Triton X-100 and 0.1% Tween-20, aortas were incubated in 12-well dishes with anti-ERG rabbit monoclonal antibody (1:200; Abcam #ab92513), anti-VCAM1 rat monoclonal antibody (1:100, BD Biosciences, #550547) or anti-SCD1 rabbit antibody (1:100, Cell Signaling, #2794). Fluorescently labeled appropriate secondary antibodies (Life Science Technologies) were applied at 1:250 dilution. Nuclei were counterstained with Hoescht 33258 (ThermoFisher, #H1398). The aortas were mounted with the endothelial layer facing up on microscopic slides using ProLong Gold Antifade Mounting Media. The images of the inner curvature and descending aorta were captured with 10x, 20x, or 63x objective on a Zeiss LSM710 or LSM 900 confocal microscope with ZEN acquisition software (Carl Zeiss Microscopy). Image processing of maximal projections of the Z-stacks was performed with NIH Fiji software.

2.7.3 Endothelial Cell Culture

Human aortic endothelial cells (HAECs, S305, Cell Applications Inc.) were grown on bovine gelatin (Sigma Aldrich, MO)-coated-plates in humidified incubator at 37 °C and 5% CO_2. Endothelial cell growth media (Cell Applications) was supplemented with 5% fetal bovine serum and penicillin-streptomycin (Life Technologies, NY). HAECs were propagated and used for experiments between passages 3 and 8.

2.7.4 Transfection Assays

At ~50% confluency, FlexiTube^{TM} specific siRNAs targeting scrambled negative control (Scr), Scd1 (si-Scd1) or PPARγ (si-PPARγ) were transfected following the manufacturer's instructions. Lipofectamine^{TM} RNAiMAX (Thermofisher, MA) diluted with Dulbecco's Modified Eagle Medium (DMEM)/10% FBS and Opti-MEM media with reduced serum (Thermofisher, MA) was used for siRNA transfection. In a subset of experiments, HAECs were transfected with scrambled siRNA (Scr) or PPAR-γ (siPPAR-γ) and then were exposed to PSS for 4 hours.

2.7.5 PSS-Exposed HAEC for Western Blots

Confluent monolayers of HAEC cultured on 6-well plates were exposed to unidirectional PSS (6, 12 and 24 hours) using a modified flow device (1). Neutralized MCDB-131 medium (Sigma Aldrich, MO) containing 7.5% sodium bicarbonate solution, 10% FBS and 4% dextran from *Leuconostoc spp* (Sigma Aldrich, MO) was used for PSS exposure. Following exposure to PSS, the center of each monolayer was removed by using a cell scraper to collect only flow-aligned cells from the periphery of the well for RNA or protein analysis.

2.7.6 Western Blots

After exposure to pulsatile shear stress, HAECs were rinsed with phosphate-buffered saline and lysed using RIPA buffer supplemented with protease and phosphatase inhibitors. Protein concentration was measured using the Bio-Rad DC assay and 50 μg of protein was loaded for Western blot with anti-SCD1 antibody (Cell Signaling). Parallel blots were performed with anti-β-tubulin (Millipore, Inc.) for loading normalization. Densitometry was performed to quantify the intensity of the bands.

2.7.7 Fatty Acid Experiments

HAEC monolayers were treated with oleic acid (Sigma, O3008) at 0.2 mM. HAEC monolayers were treated with or without 10 μM of PPARγ agonist Rosiglitazone (Sigma, L2654) for 4 hours. At the end of the experimental period, cells were lysed and processed for RNA extraction.

2.7.8 RNA extraction and Real-Time PCR

Mouse tissues or cell cultures were lysed and processed for RNA extraction using the RNA Miniprep kit (Zymo Research) according to the manufacturer’s instructions and the concentration and purity were assessed with BioDrop spectrophotometer. Total RNA (1-2 µg) were reverse-transcribed into cDNA using 5x All In One Reverse Transcription mix (Applied Biological Materials). Then, 2-5 ng of cDNA were amplified by quantitative PCR with Taq DNA polymerase and specific primers designed using NCBI software. 18s rRNA or GAPDH RNA were used as internal housekeeping control. Amplification reactions were performed, and the fluorescence was monitored in a Real Time PCR System, CFX Connect (Bio-Rad Laboratories). PCR thermal cycle parameters were: 5 minutes 95°C, 30 seconds at 60°C, and 30 seconds at 72°C. Melting curves were used to corroborate primer specificity for the intended templates. Fold expression changes were calculated using the delta-delta Ct method.

2.7.9 Supporting Figures

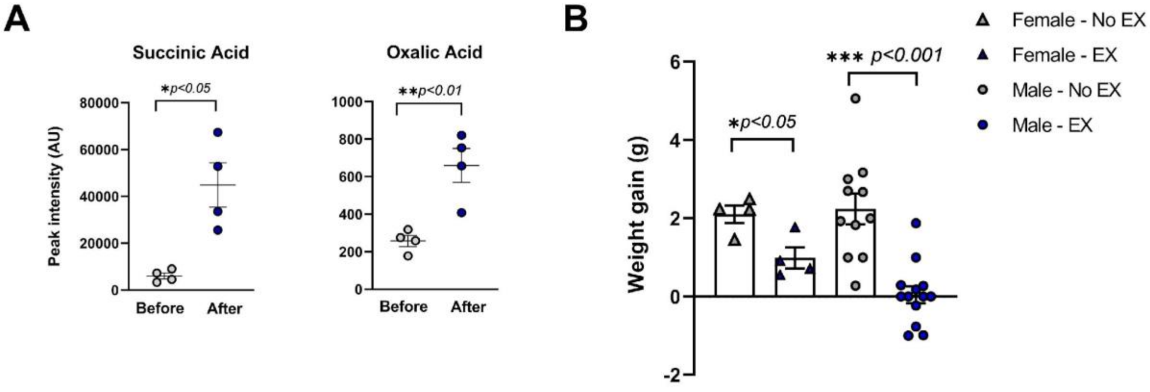

Figure S2.1. (A) Elevated levels of known metabolites succinic acid and oxalic acid, which have previously been shown to be regulated by physical activity. Data are shown as mean ± SEM and analyzed with paired two-tailed *t*-test. (B). Changes in body weight in female and male C57BL/6J mice over 14 days of voluntary wheel exercise (calculated as body weight at Day 14 – initial body weight at Day 0). Each point represents an individual animal. Results are expressed as mean ± SEM and compared using unpaired two-tailed *t*-test for each gender (females: n=4 No Exercise (Ex), N=4 EX; males: n=11 No EX, n=13 EX).

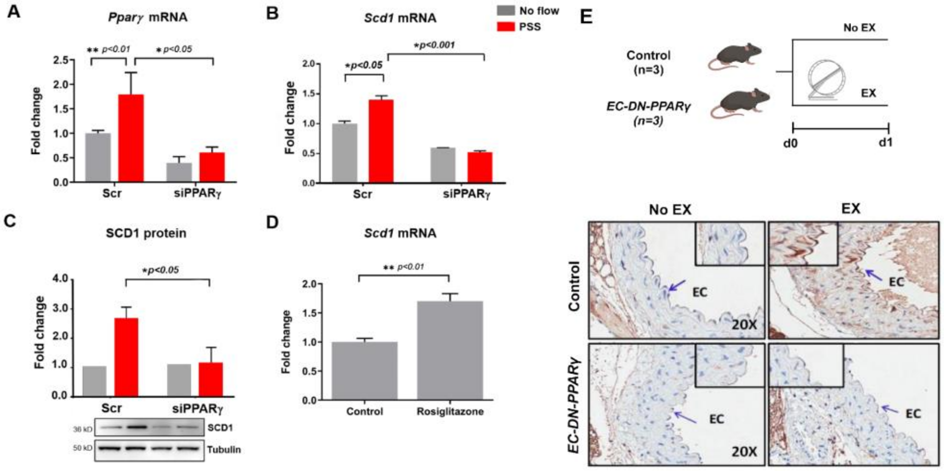

Figure S2.2. PSS-activated SCD1 expression is PPARγ-dependent. (A, B) HAECs were transfected with scrambled (Scr) or PPARγ (si PPARγ) siRNA and then subjected to PSS for 4 hours. (A) PSS increased PPARγ and *SCD1* mRNA. (B) Silencing PPARγ with siRNA completely blocked PSS-induced SCD1 expression. (C) Western Blot with anti-SCD1 antibody demonstrating the decrease in PSS-induced SCD1 protein expression after siPPARγ treatment. (D) HAECs were treated with the PPARγ agonist, Rosiglitazone (10μM), for 4 hours. Rosiglitazone significantly increased SCD1 mRNA expression as compared to the untreated control (*P* < 0.05, n=3), supporting the notion that SCD1 is flow-responsive and is PPARγ-dependent. (E) Wild type C57BL/6J or EC-dominant negative (DN)-PPARγ mice underwent 24-hr voluntary exercise. The representative images reveal the transversal sections of the descending aorta stained with anti-SCD1 antibody. SCD1 staining was prominent in the endothelial cells in WT mice after exercise but was nearly absent in the EC-DN-PPARγ mice (n=3 males). Note that SCD1 is present in the periaortic adipocytes

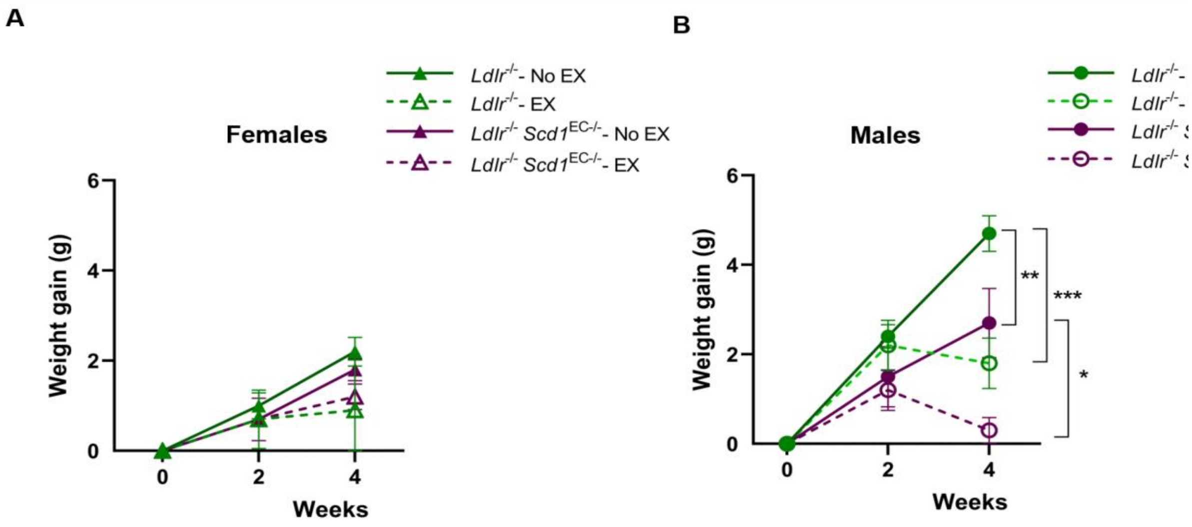

Figure S2.3. Changes in body weight in female (A) and male (B) mice over 4- week treatment with HFD and with or without exercise. Results were analyzed by two-way ANOVA followed by multiple comparisons across time points and experimental groups using Tukey test.

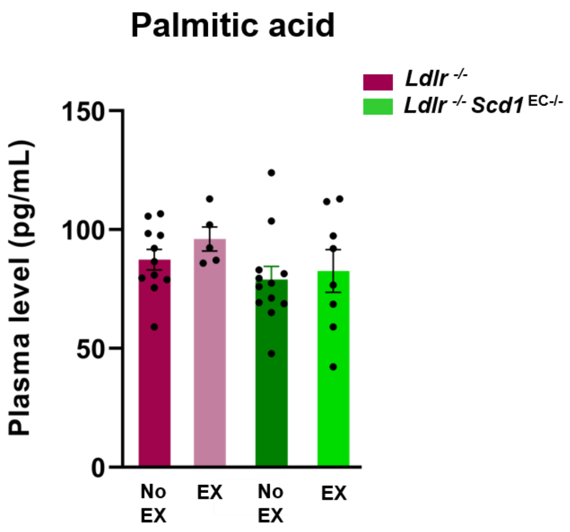

Figure S2.4. The absolute plasma concentration of saturated fatty acids palmitic and stearic in the Ldlr-/- mice and Ldlr-/-Scd1EC-/- mice. (*P > 0.05, n= 5-12; each dot represents an individual animal).

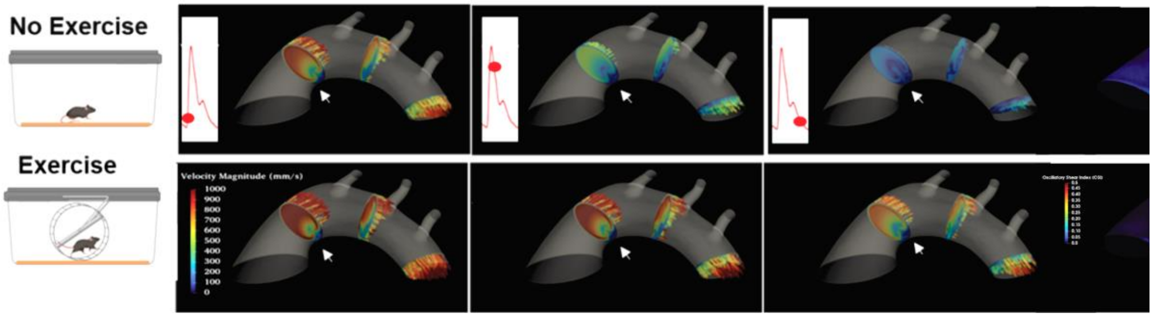

Figure S2.5. Computational fluid dynamics analysis of blood flow in mouse aortic arch under sedentary (top) and exercise (bottom) conditions. The vectors and the flow contours in the cross section are color-coded based on velocity magnitude. Oscillatory shear index contour (right) is compared between the sedentary and exercise groups.

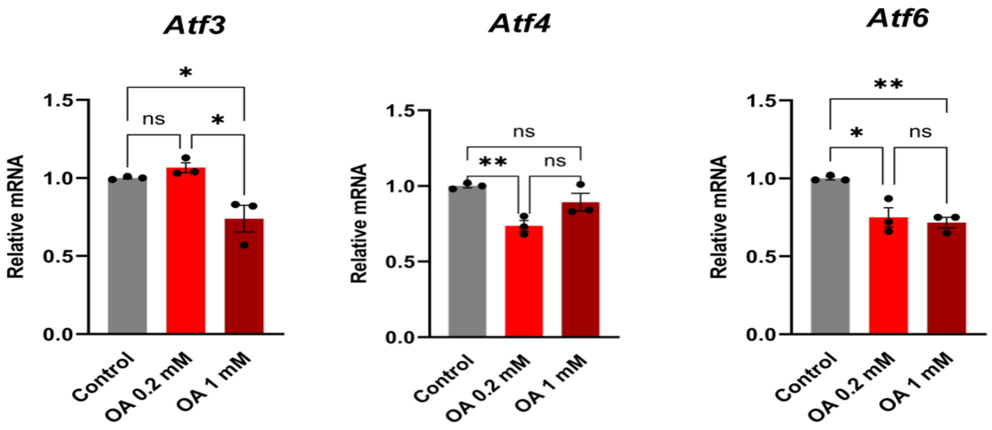

Figure S2.6. OA treatment attenuated the ER stress-related Atf3, 4 and 6 mRNA expression (ns; non-significant; * $p < 0.05$; ** $p < 0.01$; *** $p < 0.001$ between the indicated groups, n=3).

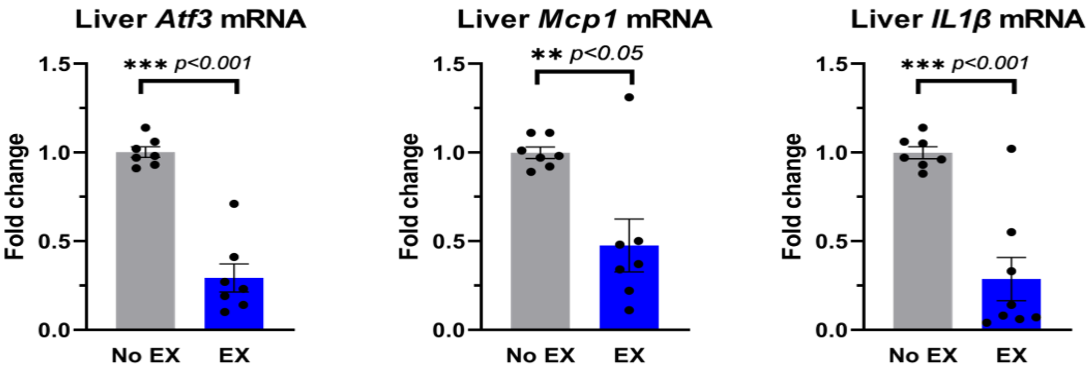

Figure S2.7. Gene expression in the liver of male C57BL/6J mice after 2 weeks of exercise (qPCR). Results were analyzed by unpaired t-test. Each dot represents an individual animal.

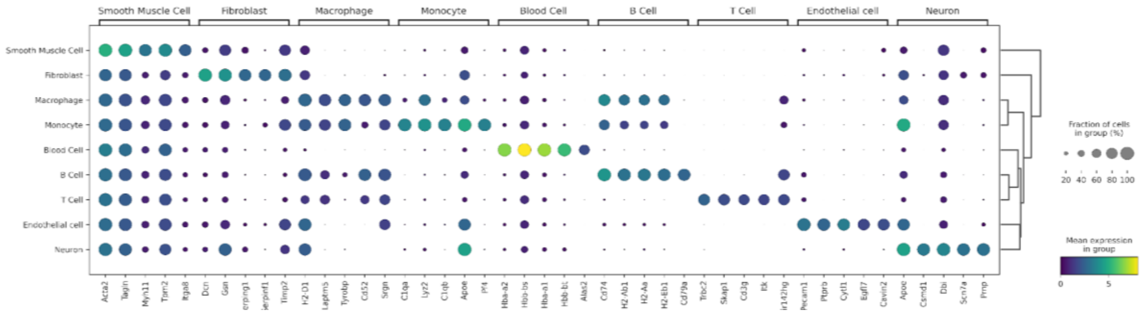

Figure S2.8 Dot plot of major conserved marker genes per cluster. We used several genes in each of the clusters to identify the 9 cell types.

BIBLIOGRAPHY

1. Lee J, Moghadam ME, Kung E, Cao H, Beebe T, Miller Y, Roman BL, Lien C-L, Chi NC, Marsden AL. Moving domain computational fluid dynamics to interface with an embryonic model of cardiac morphogenesis. PloS one. 2013;8(8):e72924.

2. Poelmann RE, Gittenberger-de Groot AC. Hemodynamics in cardiac development. Journal of cardiovascular development and disease. 2018;5(4):54.

3. Lee J, Packard RRS, Hsiai TK. Blood flow modulation of vascular dynamics. Current opinion in lipidology. 2015;26(5):376.

4. Kaski J-C, Crea F, Gersh BJ, Camici PG. Reappraisal of ischemic heart disease: fundamental role of coronary microvascular dysfunction in the pathogenesis of angina pectoris. Circulation. 2018;138(14):1463-80.

5. Omori T, Imai Y, Kikuchi K, Ishikawa T, Yamaguchi T. Hemodynamics in the microcirculation and in microfluidics. Annals of biomedical engineering. 2015;43(1):238-57.

6. Beckman JA, Duncan MS, Damrauer SM, Wells QS, Barnett JV, Wasserman DH, Bedimo RJ, Butt AA, Marconi VC, Sico JJ. Microvascular disease, peripheral artery disease, and amputation. Circulation. 2019;140(6):449-58.

7. Brownrigg JR, Hughes CO, Burleigh D, Karthikesalingam A, Patterson BO, Holt PJ, Thompson MM, de Lusignan S, Ray KK, Hinchliffe RJ. Microvascular disease and risk of cardiovascular events among individuals with type 2 diabetes: a population-level cohort study. The Lancet Diabetes & Endocrinology. 2016;4(7):588-97.

8. Van Der Laan AM, Piek JJ, Van Royen N. Targeting angiogenesis to restore the microcirculation after reperfused MI. Nature Reviews Cardiology. 2009;6(8):515-23.

9. Fei P, Lee J, Packard RRS, Sereti K-I, Xu H, Ma J, Ding Y, Kang H, Chen H, Sung K. Cardiac light-sheet fluorescent microscopy for multi-scale and rapid imaging of architecture and function. Scientific reports. 2016;6(1):1-12.

10. Ding Y, Ma J, Langenbacher AD, Baek KI, Lee J, Chang C-C, Hsu JJ, Kulkarni RP, Belperio J, Shi W. Multiscale light-sheet for rapid imaging of cardiopulmonary system. JCI insight. 2018;3(16).

11. Fei P, Nie J, Lee J, Ding Y, Li S, Zhang H, Hagiwara M, Yu T, Segura T, Ho C-M. Subvoxel light-sheet microscopy for high-resolution high-throughput volumetric imaging of large biomedical specimens. Advanced Photonics. 2019;1(1):016002.

12. Lee J, Fei P, Packard RRS, Kang H, Xu H, Baek KI, Jen N, Chen J, Yen H, Kuo C-CJ. 4-Dimensional light-sheet microscopy to elucidate shear stress modulation of cardiac

trabeculation. The Journal of clinical investigation. 2016;126(5):1679-90.

13. Vedula V, Lee J, Xu H, Kuo C-CJ, Hsiai TK, Marsden AL. A method to quantify mechanobiologic forces during zebrafish cardiac development using 4-D light sheet imaging and computational modeling. PLoS computational biology. 2017;13(10):e1005828.

14. Hsu JJ, Vedula V, Baek KI, Chen C, Chen J, Chou MI, Lam J, Subhedar S, Wang J, Ding Y. Contractile and hemodynamic forces coordinate Notch1b-mediated outflow tract valve formation. JCI insight. 2019;4(10).

15. Souilhol C, Serbanovic-Canic J, Fragiadaki M, Chico TJ, Ridger V, Roddie H, Evans PC. Endothelial responses to shear stress in atherosclerosis: a novel role for developmental genes. Nature Reviews Cardiology. 2020;17(1):52-63.

16. Dolan JM, Kolega J, Meng H. High wall shear stress and spatial gradients in vascular pathology: a review. Annals of biomedical engineering. 2013;41(7):1411-27.

17. Weijts B, Gutierrez E, Saikin SK, Ablooglu AJ, Traver D, Groisman A, Tkachenko E. Blood flow-induced Notch activation and endothelial migration enable vascular remodeling in zebrafish embryos. Nature communications. 2018;9(1):1-11.

18. Chang S-S, Tu S, Baek KI, Pietersen A, Liu Y-H, Savage VM, Hwang S-PL, Hsiai TK, Roper M. Optimal occlusion uniformly partitions red blood cells fluxes within a microvascular network. PLoS computational biology. 2017;13(12):e1005892.

19. Choi W, Kim HM, Park S, Yeom E, Doh J, Lee SJ. Variation in wall shear stress in channel networks of zebrafish models. Journal of The Royal Society Interface. 2017;14(127):20160900.

20. Lee J, Vedula V, Baek KI, Chen J, Hsu JJ, Ding Y, Chang C-C, Kang H, Small A, Fei P. Spatial and temporal variations in hemodynamic forces initiate cardiac trabeculation. JCI insight. 2018;3(13).

21. Baek KI, Packard RRS, Hsu JJ, Saffari A, Ma Z, Luu AP, Pietersen A, Yen H, Ren B, Ding Y. Ultrafine particle exposure reveals the importance of FOXO1/Notch activation complex for vascular regeneration. Antioxidants & redox signaling. 2018;28(13):1209-23.

22. Li R, Beebe T, Jen N, Yu F, Takabe W, Harrison M, Cao H, Lee J, Yang H, Han P. Shear stress–activated Wnt-Angiopoietin-2 signaling recapitulates vascular repair in zebrafish embryos. Arteriosclerosis, thrombosis, and vascular biology. 2014;34(10):2268-75.

23. Ding Y, Lee J, Hsu JJ, Chang C-C, Baek KI, Ranjbarvaziri S, Ardehali R, Packard RRS, Hsiai TK. Light-sheet imaging to elucidate cardiovascular injury and repair. Current cardiology reports. 2018;20(5):1-8.

24. Updegrove A, Wilson NM, Merkow J, Lan H, Marsden AL, Shadden SC. SimVascular: an

open source pipeline for cardiovascular simulation. Annals of biomedical engineering. 2017;45(3):525-41.

25. Lee J, Chou T-C, Kang D, Kang H, Chen J, Baek KI, Wang W, Ding Y, Di Carlo D, Tai Y-C. A rapid capillary-pressure driven micro-channel to demonstrate newtonian fluid behavior of zebrafish blood at high shear rates. Scientific reports. 2017;7(1):1-8.

26. Chen J, Lu X-Y, Wang W. Non-Newtonian effects of blood flow on hemodynamics in distal vascular graft anastomoses. Journal of Biomechanics. 2006;39(11):1983-95.

27. Baek KI, Chang S-S, Chang C-C, Roustaei M, Ding Y, Wang Y, Chen J, Odonnelle R, Chen H, Ashby JW. Vascular Injury Changes Topology of Vessel Network to Adapt to Partition of Blood Flow for New Arteriovenous Specification. bioRxiv. 2020.

28. Hove JR, Köster RW, Forouhar AS, Acevedo-Bolton G, Fraser SE, Gharib M. Intracardiac fluid forces are an essential epigenetic factor for embryonic cardiogenesis. Nature. 2003;421(6919):172-7.

29. Lawson ND, Weinstein BM. In vivo imaging of embryonic vascular development using transgenic zebrafish. Developmental biology. 2002;248(2):307-18.

30. Kluge MA, Fetterman JL, Vita JA. Mitochondria and endothelial function. Circulation research. 2013;112(8):1171-88.

31. Sun X, Feinberg MW. Regulation of endothelial cell metabolism: just go with the flow. Am Heart Assoc; 2015.

32. Wang Y, Zang QS, Liu Z, Wu Q, Maass D, Dulan G, Shaul PW, Melito L, Frantz DE, Kilgore JA. Regulation of VEGF-induced endothelial cell migration by mitochondrial reactive oxygen species. American Journal of Physiology-Cell Physiology. 2011;301(3):C695-C704.

33. De Bock K, Georgiadou M, Carmeliet P. Role of endothelial cell metabolism in vessel sprouting. Cell metabolism. 2013;18(5):634-47.

34. Kumar S, Hedges SB. A molecular timescale for vertebrate evolution. Nature. 1998;392(6679):917-20.

35. Baek KI, Li R, Jen N, Choi H, Kaboodrangi A, Ping P, Liem D, Beebe T, Hsiai TK. Flow-responsive vascular endothelial growth factor receptor-protein kinase c isoform epsilon signaling mediates glycolytic metabolites for vascular repair. Antioxidants & redox signaling. 2018;28(1):31-43.

36. Li R, Baek KI, Chang C-C, Zhou B, Hsiai TK. Mechanosensitive pathways involved in cardiovascular development and homeostasis in zebrafish. Journal of vascular research. 2019;56(6):273-83.

37. Zhang L, Alt C, Li P, White RM, Zon LI, Wei X, Lin CP. An optical platform for cell

tracking in adult zebrafish. Cytometry Part A. 2012;81(2):176-82.

38. Sasson C, Eckel R, Alger H, Bozkurt B, Carson A, Daviglus M, Deedwania P, Kirley K, Lamendola C, Nguyen M, Rajgopal Singh R, Wang T, Sanchez E. American Heart Association Diabetes and Cardiometabolic Health Summit: Summary and Recommendations. J Am Heart Assoc. 2018;7(15):e009271. doi: 10.1161/JAHA.118.009271. PubMed PMID: 30371251; PMCID: PMC6201457.

39. Maass A, Duzel S, Goerke M, Becke A, Sobieray U, Neumann K, Lovden M, Lindenberger U, Backman L, Braun-Dullaeus R, Ahrens D, Heinze HJ, Muller NG, Duzel E. Vascular hippocampal plasticity after aerobic exercise in older adults. Mol Psychiatry. 2015;20(5):585-93. Epub 20141014. doi: 10.1038/mp.2014.114. PubMed PMID: 25311366.

40. Okabe TA, Kishimoto C, Murayama T, Yokode M, Kita T. Effects of exercise on the development of atherosclerosis in apolipoprotein E-deficient mice. Exp Clin Cardiol. 2006;11(4):276-9. PubMed PMID: 18651017; PMCID: PMC2274844.

41. Aengevaeren VL, Mosterd A, Sharma S, Prakken NHJ, Mohlenkamp S, Thompson PD, Velthuis BK, Eijsvogels TMH. Exercise and Coronary Atherosclerosis: Observations, Explanations, Relevance, and Clinical Management. Circulation. 2020;141(16):1338-50. Epub 20200420. doi: 10.1161/CIRCULATIONAHA.119.044467. PubMed PMID: 32310695; PMCID: PMC7176353.

42. Kramer AF, Erickson KI, Colcombe SJ. Exercise, cognition, and the aging brain. J Appl Physiol (1985). 2006;101(4):1237-42. doi: 10.1152/japplphysiol.00500.2006. PubMed PMID: 16778001.

43. Mandolesi L, Polverino A, Montuori S, Foti F, Ferraioli G, Sorrentino P, Sorrentino G. Effects of Physical Exercise on Cognitive Functioning and Wellbeing: Biological and Psychological Benefits. Front Psychol. 2018;9:509. doi: 10.3389/fpsyg.2018.00509. PubMed PMID: 29755380; PMCID: 5934999.

44. Liu Y, Yan T, Chu JM, Chen Y, Dunnett S, Ho YS, Wong GT, Chang RC. The beneficial effects of physical exercise in the brain and related pathophysiological mechanisms in neurodegenerative diseases. Lab Invest. 2019;99(7):943-57. doi: 10.1038/s41374-019-0232-y. PubMed PMID: 30808929.

45. De Miguel Z, Khoury N, Betley MJ, Lehallier B, Willoughby D, Olsson N, Yang AC, Hahn O, Lu N, Vest RT, Bonanno LN, Yerra L, Zhang L, Saw NL, Fairchild JK, Lee D, Zhang H, McAlpine PL, Contrepois K, Shamloo M, Elias JE, Rando TA, Wyss-Coray T. Exercise plasma boosts memory and dampens brain inflammation via clusterin. Nature. 2021;600(7889):494-9. doi: 10.1038/s41586-021-04183-x. PubMed PMID: 34880498.

46. Silacci P, Desgeorges A, Mazzolai L, Chambaz C, Hayoz D. Flow pulsatility is a critical determinant of oxidative stress in endothelial cells. Hypertension. 2001;38(5):1162-6. doi: 10.1161/hy1101.095993. PubMed PMID: 11711515.

47. Hwang J, Ing MH, Salazar A, Lassegue B, Griendling K, Navab M, Sevanian A, Hsiai TK. Pulsatile versus oscillatory shear stress regulates NADPH oxidase subunit expression: implication for native LDL oxidation. Circ Res. 2003;93(12):1225-32. doi: 10.1161/01.RES.0000104087.29395.66. PubMed PMID: 14593003; PMCID: 4433384.

48. Hsiai TK, Cho SK, Wong PK, Ing M, Salazar A, Sevanian A, Navab M, Demer LL, Ho CM. Monocyte recruitment to endothelial cells in response to oscillatory shear stress. FASEB J. 2003;17(12):1648-57. doi: 10.1096/fj.02-1064com. PubMed PMID: 12958171; PMCID: 4108745.

49. Hsiai TK, Cho SK, Reddy S, Hama S, Navab M, Demer LL, Honda HM, Ho CM. Pulsatile flow regulates monocyte adhesion to oxidized lipid-induced endothelial cells. Arterioscler Thromb Vasc Biol. 2001;21(11):1770-6. doi: 10.1161/hq1001.097104. PubMed PMID: 11701464.

50. Ku DN, Giddens DP, Zarins CK, Glagov S. Pulsatile flow and atherosclerosis in the human carotid bifurcation. Positive correlation between plaque location and low oscillating shear stress. Arteriosclerosis. 1985;5(3):293-302. doi: 10.1161/01.atv.5.3.293. PubMed PMID: 3994585.

51. Souilhol C, Serbanovic-Canic J, Fragiadaki M, Chico TJ, Ridger V, Roddie H, Evans PC. Endothelial responses to shear stress in atherosclerosis: a novel role for developmental genes. Nat Rev Cardiol. 2020;17(1):52-63. doi: 10.1038/s41569-019-0239-5. PubMed PMID: 31366922.

52. Hwang J, Saha A, Boo YC, Sorescu GP, McNally JS, Holland SM, Dikalov S, Giddens DP, Griendling KK, Harrison DG, Jo H. Oscillatory shear stress stimulates endothelial production of O2- from p47phox-dependent NAD(P)H oxidases, leading to monocyte adhesion. J Biol Chem. 2003;278(47):47291-8. doi: 10.1074/jbc.M305150200. PubMed PMID: 12958309.

53. Sanford JA, Nogiec CD, Lindholm ME, Adkins JN, Amar D, Dasari S, Drugan JK, Fernandez FM, Radom-Aizik S, Schenk S, Snyder MP, Tracy RP, Vanderboom P, Trappe S, Walsh MJ, Molecular Transducers of Physical Activity C. Molecular Transducers of Physical Activity Consortium (MoTrPAC): Mapping the Dynamic Responses to Exercise. Cell. 2020;181(7):1464-74. doi: 10.1016/j.cell.2020.06.004. PubMed PMID: 32589957; PMCID: 8800485.

54. Lu X, Hu S, Liao Y, Zheng J, Zeng T, Zhong X, Liu G, Gou L, Chen L. Vascular endothelial growth factor B promotes transendothelial fatty acid transport into skeletal muscle via histone modifications during catch-up growth. Am J Physiol Endocrinol Metab. 2020;319(6):E1031-E43. Epub 20200921. doi: 10.1152/ajpendo.00090.2020. PubMed PMID: 32954823.

55. Moessinger C, Nilsson I, Muhl L, Zeitelhofer M, Heller Sahlgren B, Skogsberg J, Eriksson U. VEGF-B signaling impairs endothelial glucose transcytosis by decreasing membrane cholesterol content. EMBO Rep. 2020;21(7):e49343. Epub 20200524. doi:

10.15252/embr.201949343. PubMed PMID: 32449307; PMCID: PMC7332976.

56. Kanda T, Brown JD, Orasanu G, Vogel S, Gonzalez FJ, Sartoretto J, Michel T, Plutzky J. PPARgamma in the endothelium regulates metabolic responses to high-fat diet in mice. J Clin Invest. 2009;119(1):110-24. Epub 20081208. doi: 10.1172/JCI36233. PubMed PMID: 19065047; PMCID: PMC2613459.

57. Fang S, Livergood MC, Nakagawa P, Wu J, Sigmund CD. Role of the Peroxisome Proliferator Activated Receptors in Hypertension. Circ Res. 2021;128(7):1021-39. doi: 10.1161/CIRCRESAHA.120.318062. PubMed PMID: 33793338; PMCID: 8020861.

58. Nicol CJ, Adachi M, Akiyama TE, Gonzalez FJ. PPARgamma in endothelial cells influences high fat diet-induced hypertension. Am J Hypertens. 2005;18(4 Pt 1):549-56. doi: 10.1016/j.amjhyper.2004.10.032. PubMed PMID: 15831367.

59. Butcher LR, Thomas A, Backx K, Roberts A, Webb R, Morris K. Low-intensity exercise exerts beneficial effects on plasma lipids via PPARgamma. Med Sci Sports Exerc. 2008;40(7):1263-70. doi: 10.1249/MSS.0b013e31816c091d. PubMed PMID: 18580406.

60. Qin X, Tian J, Zhang P, Fan Y, Chen L, Guan Y, Fu Y, Zhu Y, Chien S, Wang N. Laminar shear stress up-regulates the expression of stearoyl-CoA desaturase-1 in vascular endothelial cells. Cardiovasc Res. 2007;74(3):506-14. doi: 10.1016/j.cardiores.2007.02.014. PubMed PMID: 17368438; PMCID: 2791953.

61. Ntambi JM, Miyazaki M. Regulation of stearoyl-CoA desaturases and role in metabolism. Prog Lipid Res. 2004;43(2):91-104. doi: 10.1016/s0163-7827(03)00039-0. PubMed PMID: 14654089.

62. Beyer AM, de Lange WJ, Halabi CM, Modrick ML, Keen HL, Faraci FM, Sigmund CD. Endothelium-specific interference with peroxisome proliferator activated receptor gamma causes cerebral vascular dysfunction in response to a high-fat diet. Circ Res. 2008;103(6):654-61. Epub 20080731. doi: 10.1161/CIRCRESAHA.108.176339. PubMed PMID: 18676352; PMCID: PMC2583077.

63. Miyazaki M, Flowers MT, Sampath H, Chu K, Otzelberger C, Liu X, Ntambi JM. Hepatic stearoyl-CoA desaturase-1 deficiency protects mice from carbohydrate-induced adiposity and hepatic steatosis. Cell Metab. 2007;6(6):484-96. doi: 10.1016/j.cmet.2007.10.014. PubMed PMID: 18054317.

64. Mukherjee P, Hough G, Chattopadhyay A, Grijalva V, O'Connor EI, Meriwether D, Wagner A, Ntambi JM, Navab M, Reddy ST, Fogelman AM. Role of enterocyte stearoyl-Co-A desaturase-1 in LDLR-null mice. J Lipid Res. 2018;59(10):1818-40. Epub 20180823. doi: 10.1194/jlr.M083527. PubMed PMID: 30139760; PMCID: PMC6168294.

65. Alva JA, Zovein AC, Monvoisin A, Murphy T, Salazar A, Harvey NL, Carmeliet P, Iruela-Arispe ML. VE-Cadherin-Cre-recombinase transgenic mouse: a tool for lineage analysis and

gene deletion in endothelial cells. Dev Dyn. 2006;235(3):759-67. doi: 10.1002/dvdy.20643. PubMed PMID: 16450386.

66. Lujan HL, DiCarlo SE. Cardiac output, at rest and during exercise, before and during myocardial ischemia, reperfusion, and infarction in conscious mice. Am J Physiol Regul Integr Comp Physiol. 2013;304(4):R286-95. Epub 20130109. doi: 10.1152/ajpregu.00517.2012. PubMed PMID: 23302959; PMCID: PMC3567356.

67. Lujan HL, Janbaih H, Feng HZ, Jin JP, DiCarlo SE. Ventricular function during exercise in mice and rats. Am J Physiol Regul Integr Comp Physiol. 2012;302(1):R68-74. Epub 20111019. doi: 10.1152/ajpregu.00340.2011. PubMed PMID: 22012697; PMCID: PMC3349383.

68. Madhavan S, Kemmerling EMC. The effect of inlet and outlet boundary conditions in image-based CFD modeling of aortic flow. Biomed Eng Online. 2018;17(1):66. Epub 20180530. doi: 10.1186/s12938-018-0497-1. PubMed PMID: 29843730; PMCID: PMC5975715.

69. Vedula V. https://github.com/SimVascular/svFSI 2018. Available from: https://github.com/SimVascular/svFSI.

70. Hsiai TK, Cho SK, Honda HM, Hama S, Navab M, Demer LL, Ho CM. Endothelial cell dynamics under pulsating flows: significance of high versus low shear stress slew rates (d(tau)/dt). Ann Biomed Eng. 2002;30(5):646-56. doi: 10.1114/1.1484222. PubMed PMID: 12108839.

71. Baek KI, Li R, Jen N, Choi H, Kaboodrangi A, Ping P, Liem D, Beebe T, Hsiai TK. Flow-Responsive Vascular Endothelial Growth Factor Receptor-Protein Kinase C Isoform Epsilon Signaling Mediates Glycolytic Metabolites for Vascular Repair. Antioxid Redox Signal. 2018;28(1):31-43. doi: 10.1089/ars.2017.7044. PubMed PMID: 28762754; PMCID: 5695747.

72. Theodorou K, Boon RA. Endothelial Cell Metabolism in Atherosclerosis. Front Cell Dev Biol. 2018;6:82. Epub 20180807. doi: 10.3389/fcell.2018.00082. PubMed PMID: 30131957; PMCID: PMC6090045.

73. Kuo A, Lee MY, Sessa WC. Lipid Droplet Biogenesis and Function in the Endothelium. Circ Res. 2017;120(8):1289-97. Epub 20170124. doi: 10.1161/CIRCRESAHA.116.310498. PubMed PMID: 28119423; PMCID: PMC5392152.

74. Kuo TC, Tian TF, Tseng YJ. 3Omics: a web-based systems biology tool for analysis, integration and visualization of human transcriptomic, proteomic and metabolomic data. BMC Syst Biol. 2013;7:64. Epub 20130723. doi: 10.1186/1752-0509-7-64. PubMed PMID: 23875761; PMCID: PMC3723580.

75. Towler DA, Bidder M, Latifi T, Coleman T, Semenkovich CF. Diet-induced diabetes

activates an osteogenic gene regulatory program in the aortas of low density lipoprotein receptor-deficient mice. J Biol Chem. 1998;273(46):30427-34. doi: 10.1074/jbc.273.46.30427. PubMed PMID: 9804809.

76. Kim S, Park HK, Jung HY, Lee SY, Min KW, Kim WY, Han HS, Kim WS, Hwang TS, Lim SD. ERG Immunohistochemistry as an Endothelial Marker for Assessing Lymphovascular Invasion. Korean J Pathol. 2013;47(4):355-64. doi: 10.4132/KoreanJPathol.2013.47.4.355. PubMed PMID: 24009631; PMCID: 3759635.

77. Franck G, Even G, Gautier A, Salinas M, Loste A, Procopio E, Gaston AT, Morvan M, Dupont S, Deschildre C, Berissi S, Laschet J, Nataf P, Nicoletti A, Michel JB, Caligiuri G. Haemodynamic stress-induced breaches of the arterial intima trigger inflammation and drive atherogenesis. Eur Heart J. 2019;40(11):928-37. doi: 10.1093/eurheartj/ehy822. PubMed PMID: 30541066.

78. Ley K, Huo Y. VCAM-1 is critical in atherosclerosis. J Clin Invest. 2001;107(10):1209-10. doi: 10.1172/JCI13005. PubMed PMID: 11375406; PMCID: PMC209304.

79. Nelken NA, Coughlin SR, Gordon D, Wilcox JN. Monocyte chemoattractant protein-1 in human atheromatous plaques. J Clin Invest. 1991;88(4):1121-7. doi: 10.1172/JCI115411. PubMed PMID: 1843454; PMCID: PMC295565.

80. Gencer S, Evans BR, van der Vorst EPC, Doring Y, Weber C. Inflammatory Chemokines in Atherosclerosis. Cells. 2021;10(2). Epub 20210125. doi: 10.3390/cells10020226. PubMed PMID: 33503867; PMCID: PMC7911854.

81. Orecchioni M, Kobiyama K, Winkels H, Ghosheh Y, McArdle S, Mikulski Z, Kiosses WB, Fan Z, Wen L, Jung Y, Roy P, Ali AJ, Miyamoto Y, Mangan M, Makings J, Wang Z, Denn A, Vallejo J, Owens M, Durant CP, Braumann S, Mader N, Li L, Matsunami H, Eckmann L, Latz E, Wang Z, Hazen SL, Ley K. Olfactory receptor 2 in vascular macrophages drives atherosclerosis by NLRP3-dependent IL-1 production. Science. 2022;375(6577):214-21. Epub 20220113. doi: 10.1126/science.abg3067. PubMed PMID: 35025664.

82. Satta S, Beal R, Smith R, Luo X, Ferris GR, Langford-Smith A, Teasdale J, Ajime TT, Serre J, Hazell G, Newby GS, Johnson JL, Kurinna S, Humphries MJ, Gayan-Ramirez G, Libby P, Degens H, Yu B, Johnson T, Alexander Y, Jia H, Newby AC, White SJ. A Nrf2-OSGIN1&2-HSP70 axis mediates cigarette smoke-induced endothelial detachment: implications for plaque erosion. Cardiovasc Res. 2023. Epub 20230218. doi: 10.1093/cvr/cvad022. PubMed PMID: 36804807.

83. Lu Y, Gao X, Wang R, Sun J, Guo B, Wei R, Jia Y. Adiponectin inhibits proliferation of vascular endothelial cells induced by Ox-LDL by promoting dephosphorylation of Caveolin-1 and depolymerization of eNOS and up-regulating release of NO. Int Immunopharmacol. 2019;73:424-34. Epub 20190529. doi: 10.1016/j.intimp.2019.05.017. PubMed PMID: 31152980.

84. Vamecq J, Andreoletti P, El Kebbaj R, Saih FE, Latruffe N, El Kebbaj MHS, Lizard G, Nasser B, Cherkaoui-Malki M. Peroxisomal Acyl-CoA Oxidase Type 1: Anti-Inflammatory and Anti-Aging Properties with a Special Emphasis on Studies with LPS and Argan Oil as a Model Transposable to Aging. Oxid Med Cell Longev. 2018;2018:6986984. Epub 20180325. doi: 10.1155/2018/6986984. PubMed PMID: 29765501; PMCID: PMC5889864.

85. Huang J, Viswakarma N, Yu S, Jia Y, Bai L, Vluggens A, Cherkaoui-Malki M, Khan M, Singh I, Yang G, Rao MS, Borensztajn J, Reddy JK. Progressive endoplasmic reticulum stress contributes to hepatocarcinogenesis in fatty acyl-CoA oxidase 1-deficient mice. Am J Pathol. 2011;179(2):703-13. Epub 20110612. doi: 10.1016/j.ajpath.2011.04.030. PubMed PMID: 21801867; PMCID: PMC3157234.

86. Kubota T, Kubota N, Kadowaki T. The role of endothelial insulin signaling in the regulation of glucose metabolism. Rev Endocr Metab Disord. 2013;14(2):207-16. doi: 10.1007/s11154-013-9242-z. PubMed PMID: 23589150.

87. Kubota T, Kubota N, Kumagai H, Yamaguchi S, Kozono H, Takahashi T, Inoue M, Itoh S, Takamoto I, Sasako T, Kumagai K, Kawai T, Hashimoto S, Kobayashi T, Sato M, Tokuyama K, Nishimura S, Tsunoda M, Ide T, Murakami K, Yamazaki T, Ezaki O, Kawamura K, Masuda H, Moroi M, Sugi K, Oike Y, Shimokawa H, Yanagihara N, Tsutsui M, Terauchi Y, Tobe K, Nagai R, Kamata K, Inoue K, Kodama T, Ueki K, Kadowaki T. Impaired insulin signaling in endothelial cells reduces insulin-induced glucose uptake by skeletal muscle. Cell Metab. 2011;13(3):294-307. doi: 10.1016/j.cmet.2011.01.018. PubMed PMID: 21356519.

88. Sun X, Lv H, Zhao P, He J, Cui Q, Wei M, Feng S, Zhu Y. Commutative regulation between endothelial NO synthase and insulin receptor substrate 2 by microRNAs. J Mol Cell Biol. 2019;11(6):509-20. doi: 10.1093/jmcb/mjy055. PubMed PMID: 30295821; PMCID: PMC6734486.

89. Lewis MJ, Barnes MR, Blighe K, Goldmann K, Rana S, Hackney JA, Ramamoorthi N, John CR, Watson DS, Kummerfeld SK, Hands R, Riahi S, Rocher-Ros V, Rivellese F, Humby F, Kelly S, Bombardieri M, Ng N, DiCicco M, van der Heijde D, Landewe R, van der Helm-van Mil A, Cauli A, McInnes IB, Buckley CD, Choy E, Taylor PC, Townsend MJ, Pitzalis C. Molecular Portraits of Early Rheumatoid Arthritis Identify Clinical and Treatment Response Phenotypes. Cell Rep. 2019;28(9):2455-70 e5. doi: 10.1016/j.celrep.2019.07.091. PubMed PMID: 31461658; PMCID: PMC6718830.

90. Tsao CW, Aday AW, Almarzooq ZI, Alonso A, Beaton AZ, Bittencourt MS, Boehme AK, Buxton AE, Carson AP, Commodore-Mensah Y, Elkind MSV, Evenson KR, Eze-Nliam C, Ferguson JF, Generoso G, Ho JE, Kalani R, Khan SS, Kissela BM, Knutson KL, Levine DA, Lewis TT, Liu J, Loop MS, Ma J, Mussolino ME, Navaneethan SD, Perak AM, Poudel R, Rezk-Hanna M, Roth GA, Schroeder EB, Shah SH, Thacker EL, VanWagner LB, Virani SS, Voecks JH, Wang NY, Yaffe K, Martin SS. Heart Disease and Stroke Statistics-2022 Update: A Report From the American Heart Association. Circulation. 2022;145(8):e153-e639. Epub 20220126. doi: 10.1161/CIR.0000000000001052. PubMed PMID: 35078371.

91. Zhou J, Li YS, Chien S. Shear stress-initiated signaling and its regulation of endothelial function. Arterioscler Thromb Vasc Biol. 2014;34(10):2191-8. Epub 20140529. doi: 10.1161/ATVBAHA.114.303422. PubMed PMID: 24876354; PMCID: PMC4169328.

92. Brown AJ, Teng Z, Evans PC, Gillard JH, Samady H, Bennett MR. Role of biomechanical forces in the natural history of coronary atherosclerosis. Nat Rev Cardiol. 2016;13(4):210-20. Epub 20160129. doi: 10.1038/nrcardio.2015.203. PubMed PMID: 26822720.

93. Frangos JA, Huang TY, Clark CB. Steady shear and step changes in shear stimulate endothelium via independent mechanisms--superposition of transient and sustained nitric oxide production. Biochem Biophys Res Commun. 1996;224(3):660-5. doi: 10.1006/bbrc.1996.1081. PubMed PMID: 8713104.

94. Li R, Jen N, Wu L, Lee J, Fang K, Quigley K, Lee K, Wang S, Zhou B, Vergnes L, Chen YR, Li Z, Reue K, Ann DK, Hsiai TK. Disturbed Flow Induces Autophagy, but Impairs Autophagic Flux to Perturb Mitochondrial Homeostasis. Antioxid Redox Signal. 2015;23(15):1207-19. doi: 10.1089/ars.2014.5896. PubMed PMID: 26120766; PMCID: 4657520.

95. Buhman KK, Chen HC, Farese RV, Jr. The enzymes of neutral lipid synthesis. J Biol Chem. 2001;276(44):40369-72. Epub 20010905. doi: 10.1074/jbc.R100050200. PubMed PMID: 11544264.

96. Man WC, Miyazaki M, Chu K, Ntambi J. Colocalization of SCD1 and DGAT2: implying preference for endogenous monounsaturated fatty acids in triglyceride synthesis. J Lipid Res. 2006;47(9):1928-39. Epub 20060602. doi: 10.1194/jlr.M600172-JLR200. PubMed PMID: 16751624.

97. Zou Y, Wang YN, Ma H, He ZH, Tang Y, Guo L, Liu Y, Ding M, Qian SW, Tang QQ. SCD1 promotes lipid mobilization in subcutaneous white adipose tissue. J Lipid Res. 2020;61(12):1589-604. Epub 20200925. doi: 10.1194/jlr.RA120000869. PubMed PMID: 32978274; PMCID: PMC7707166.

98. Ntambi JM, Buhrow SA, Kaestner KH, Christy RJ, Sibley E, Kelly TJ, Jr., Lane MD. Differentiation-induced gene expression in 3T3-L1 preadipocytes. Characterization of a differentially expressed gene encoding stearoyl-CoA desaturase. J Biol Chem. 1988;263(33):17291-300. PubMed PMID: 2903162.

99. Zheng Y, Prouty SM, Harmon A, Sundberg JP, Stenn KS, Parimoo S. Scd3--a novel gene of the stearoyl-CoA desaturase family with restricted expression in skin. Genomics. 2001;71(2):182-91. doi: 10.1006/geno.2000.6429. PubMed PMID: 11161812.

100. Miyazaki M, Jacobson MJ, Man WC, Cohen P, Asilmaz E, Friedman JM, Ntambi JM. Identification and characterization of murine SCD4, a novel heart-specific stearoyl-CoA desaturase isoform regulated by leptin and dietary factors. J Biol Chem. 2003;278(36):33904-11. Epub 20030618. doi: 10.1074/jbc.M304724200. PubMed PMID: 12815040.

101. AM A, Syed DN, Ntambi JM. Insights into Stearoyl-CoA Desaturase-1 Regulation of Systemic Metabolism. Trends Endocrinol Metab. 2017;28(12):831-42. Epub 20171028. doi: 10.1016/j.tem.2017.10.003. PubMed PMID: 29089222; PMCID: PMC5701860.

102. Lai KKY, Kweon SM, Chi F, Hwang E, Kabe Y, Higashiyama R, Qin L, Yan R, Wu RP, Lai K, Fujii N, French S, Xu J, Wang JY, Murali R, Mishra L, Lee JS, Ntambi JM, Tsukamoto H. Stearoyl-CoA Desaturase Promotes Liver Fibrosis and Tumor Development in Mice via a Wnt Positive-Signaling Loop by Stabilization of Low-Density Lipoprotein-Receptor-Related Proteins 5 and 6. Gastroenterology. 2017;152(6):1477-91. doi: 10.1053/j.gastro.2017.01.021. PubMed PMID: 28143772; PMCID: 5406249.

103. Li ZZ, Berk M, McIntyre TM, Feldstein AE. Hepatic lipid partitioning and liver damage in nonalcoholic fatty liver disease: role of stearoyl-CoA desaturase. J Biol Chem. 2009;284(9):5637-44. Epub 20090101. doi: 10.1074/jbc.M807616200. PubMed PMID: 19119140; PMCID: PMC2645822.

104. Liu HH, Xu Y, Li CJ, Hsu SJ, Lin XH, Zhang R, Chen J, Chen J, Gao DM, Cui JF, Yang XR, Ren ZG, Chen RX. An SCD1-dependent mechanoresponsive pathway promotes HCC invasion and metastasis through lipid metabolic reprogramming. Mol Ther. 2022;30(7):2554-67. Epub 20220328. doi: 10.1016/j.ymthe.2022.03.015. PubMed PMID: 35358687; PMCID: PMC9263248.

105. Ntambi JM, Miyazaki M, Stoehr JP, Lan H, Kendziorski CM, Yandell BS, Song Y, Cohen P, Friedman JM, Attie AD. Loss of stearoyl-CoA desaturase-1 function protects mice against adiposity. Proc Natl Acad Sci U S A. 2002;99(17):11482-6. Epub 20020812. doi: 10.1073/pnas.132384699. PubMed PMID: 12177411; PMCID: PMC123282.

106. MacDonald ML, van Eck M, Hildebrand RB, Wong BW, Bissada N, Ruddle P, Kontush A, Hussein H, Pouladi MA, Chapman MJ, Fievet C, van Berkel TJ, Staels B, McManus BM, Hayden MR. Despite antiatherogenic metabolic characteristics, SCD1-deficient mice have increased inflammation and atherosclerosis. Arterioscler Thromb Vasc Biol. 2009;29(3):341-7. Epub 20081218. doi: 10.1161/ATVBAHA.108.181099. PubMed PMID: 19095997; PMCID: PMC2873333.

107. Jiang G, Li Z, Liu F, Ellsworth K, Dallas-Yang Q, Wu M, Ronan J, Esau C, Murphy C, Szalkowski D, Bergeron R, Doebber T, Zhang BB. Prevention of obesity in mice by antisense oligonucleotide inhibitors of stearoyl-CoA desaturase-1. J Clin Invest. 2005;115(4):1030-8. Epub 20050310. doi: 10.1172/JCI23962. PubMed PMID: 15761499; PMCID: PMC1062893.

108. Niebauer J, Cooke JP. Cardiovascular effects of exercise: role of endothelial shear stress. J Am Coll Cardiol. 1996;28(7):1652-60. doi: 10.1016/S0735-1097(96)00393-2. PubMed PMID: 8962548.

109. Jen N, Yu F, Lee J, Wasmund S, Dai X, Chen C, Chawareeyawong P, Yang Y, Li R, Hamdan MH, Hsiai TK. Atrial fibrillation pacing decreases intravascular shear stress in a New Zealand white rabbit model: implications in endothelial function. Biomech Model Mechanobiol.

2013;12(4):735-45. doi: 10.1007/s10237-012-0437-0. PubMed PMID: 22983703; PMCID: 3548016.

110. Hong J, Park E, Lee J, Lee Y, Rooney BV, Park Y. Exercise training mitigates ER stress and UCP2 deficiency-associated coronary vascular dysfunction in atherosclerosis. Sci Rep. 2021;11(1):15449. Epub 20210729. doi: 10.1038/s41598-021-94944-5. PubMed PMID: 34326395; PMCID: PMC8322067.

111. Li VL, He Y, Contrepois K, Liu H, Kim JT, Wiggenhorn AL, Tanzo JT, Tung AS, Lyu X, Zushin PH, Jansen RS, Michael B, Loh KY, Yang AC, Carl CS, Voldstedlund CT, Wei W, Terrell SM, Moeller BC, Arthur RM, Wallis GA, van de Wetering K, Stahl A, Kiens B, Richter EA, Banik SM, Snyder MP, Xu Y, Long JZ. An exercise-inducible metabolite that suppresses feeding and obesity. Nature. 2022;606(7915):785-90. Epub 20220615. doi: 10.1038/s41586-022-04828-5. PubMed PMID: 35705806.

112. Ball K, Carver A, Downing K, Jackson M, O'Rourke K. Addressing the social determinants of inequities in physical activity and sedentary behaviours. Health Promot Int. 2015;30 Suppl 2:ii18-9. Epub 20150407. doi: 10.1093/heapro/dav022. PubMed PMID: 25855784.

113. Chen H, Chen C, Spanos M, Li G, Lu R, Bei Y, Xiao J. Exercise training maintains cardiovascular health: signaling pathways involved and potential therapeutics. Signal Transduct Target Ther. 2022;7(1):306. Epub 20220901. doi: 10.1038/s41392-022-01153-1. PubMed PMID: 36050310; PMCID: PMC9437103.

114. Evans RM, Barish GD, Wang YX. PPARs and the complex journey to obesity. Nat Med. 2004;10(4):355-61. doi: 10.1038/nm1025. PubMed PMID: 15057233.

115. Liu Y, Zhu Y, Rannou F, Lee TS, Formentin K, Zeng L, Yuan X, Wang N, Chien S, Forman BM, Shyy JY. Laminar flow activates peroxisome proliferator-activated receptor-gamma in vascular endothelial cells. Circulation. 2004;110(9):1128-33. Epub 20040816. doi: 10.1161/01.CIR.0000139850.08365.EC. PubMed PMID: 15313948.

116. Wang YL, Chen CT, Tung CS, Tsai MC. Laminar shear stress upregulates the expression of PPARs in vascular endothelial cells under high free fatty acid-induced stress. Exp Ther Med. 2021;21(5):438. Epub 20210226. doi: 10.3892/etm.2021.9855. PubMed PMID: 33747175; PMCID: PMC7967849.

117. Ikeda J, Ichiki T, Takahara Y, Kojima H, Sankoda C, Kitamoto S, Tokunou T, Sunagawa K. PPARgamma Agonists Attenuate Palmitate-Induced ER Stress through Up-Regulation of SCD-1 in Macrophages. PLoS One. 2015;10(6):e0128546. doi: 10.1371/journal.pone.0128546. PubMed PMID: 26061913; PMCID: 4464548.

118. Mukohda M, Stump M, Ketsawatsomkron P, Hu C, Quelle FW, Sigmund CD. Endothelial PPAR-gamma provides vascular protection from IL-1beta-induced oxidative stress. Am J Physiol Heart Circ Physiol. 2016;310(1):H39-48. Epub 20151113. doi:

10.1152/ajpheart.00490.2015. PubMed PMID: 26566726; PMCID: PMC4796462.

119. De Silva TM, Li Y, Kinzenbaw DA, Sigmund CD, Faraci FM. Endothelial PPARgamma (Peroxisome Proliferator-Activated Receptor-gamma) Is Essential for Preventing Endothelial Dysfunction With Aging. Hypertension. 2018;72(1):227-34. Epub 20180507. doi: 10.1161/HYPERTENSIONAHA.117.10799. PubMed PMID: 29735632; PMCID: PMC6002945.

120. Ma Y, Wang W, Zhang J, Lu Y, Wu W, Yan H, Wang Y. Hyperlipidemia and atherosclerotic lesion development in Ldlr-deficient mice on a long-term high-fat diet. PLoS One. 2012;7(4):e35835. Epub 20120425. doi: 10.1371/journal.pone.0035835. PubMed PMID: 22558236; PMCID: PMC3338468.

121. Martinez-Gonzalez MA, Sayon-Orea C, Bullon-Vela V, Bes-Rastrollo M, Rodriguez-Artalejo F, Yusta-Boyo MJ, Garcia-Solano M. Effect of olive oil consumption on cardiovascular disease, cancer, type 2 diabetes, and all-cause mortality: A systematic review and meta-analysis. Clin Nutr. 2022;41(12):2659-82. Epub 20221010. doi: 10.1016/j.clnu.2022.10.001. PubMed PMID: 36343558.

122. Yubero-Serrano EM, Lopez-Moreno J, Gomez-Delgado F, Lopez-Miranda J. Extra virgin olive oil: More than a healthy fat. Eur J Clin Nutr. 2019;72(Suppl 1):8-17. doi: 10.1038/s41430-018-0304-x. PubMed PMID: 30487558.

123. Carluccio MA, Massaro M, Bonfrate C, Siculella L, Maffia M, Nicolardi G, Distante A, Storelli C, De Caterina R. Oleic acid inhibits endothelial activation : A direct vascular antiatherogenic mechanism of a nutritional component in the mediterranean diet. Arterioscler Thromb Vasc Biol. 1999;19(2):220-8. doi: 10.1161/01.atv.19.2.220. PubMed PMID: 9974401.

124. Perdomo L, Beneit N, Otero YF, Escribano O, Diaz-Castroverde S, Gomez-Hernandez A, Benito M. Protective role of oleic acid against cardiovascular insulin resistance and in the early and late cellular atherosclerotic process. Cardiovasc Diabetol. 2015;14:75. Epub 20150610. doi: 10.1186/s12933-015-0237-9. PubMed PMID: 26055507; PMCID: PMC4475625.

125. Lee DM, Sevits KJ, Battson ML, Wei Y, Cox-York KA, Gentile CL. Monounsaturated fatty acids protect against palmitate-induced lipoapoptosis in human umbilical vein endothelial cells. PLoS One. 2019;14(12):e0226940. Epub 20191231. doi: 10.1371/journal.pone.0226940. PubMed PMID: 31891641; PMCID: PMC6938355.

126. Harvey KA, Walker CL, Xu Z, Whitley P, Pavlina TM, Hise M, Zaloga GP, Siddiqui RA. Oleic acid inhibits stearic acid-induced inhibition of cell growth and pro-inflammatory responses in human aortic endothelial cells. J Lipid Res. 2010;51(12):3470-80. Epub 20100917. doi: 10.1194/jlr.M010371. PubMed PMID: 20852092; PMCID: PMC2975719.

127. von Roemeling CA, Marlow LA, Wei JJ, Cooper SJ, Caulfield TR, Wu K, Tan WW, Tun

HW, Copland JA. Stearoyl-CoA desaturase 1 is a novel molecular therapeutic target for clear cell renal cell carcinoma. Clin Cancer Res. 2013;19(9):2368-80. Epub 20130430. doi: 10.1158/1078-0432.CCR-12-3249. PubMed PMID: 23633458; PMCID: PMC3644999.

128. Aljohani A, Khan MI, Syed DN, Abram B, Lewis S, Neill LO, Mukhtar H, Ntambi JM. Hepatic Stearoyl-CoA desaturase-1 deficiency-mediated activation of mTORC1- PGC-1alpha axis regulates ER stress during high-carbohydrate feeding. Sci Rep. 2019;9(1):15761. Epub 20191031. doi: 10.1038/s41598-019-52339-7. PubMed PMID: 31673045; PMCID: PMC6823547.

129. Romero F, Hong X, Shah D, Kallen CB, Rosas I, Guo Z, Schriner D, Barta J, Shaghaghi H, Hoek JB, Mesaros C, Choi AM, Snyder NW, Summer R. Lipid Synthesis Is Required to Resolve Endoplasmic Reticulum Stress and Limit Fibrotic Responses in the Lung. Am J Respir Cell Mol Biol. 2018;59(2):225-36. doi: 10.1165/rcmb.2017-0340OC. PubMed PMID: 29465261; PMCID: 6096342.

130. Alemany R, Suzuki K, Curiel DT. Blood clearance rates of adenovirus type 5 in mice. J Gen Virol. 2000;81(Pt 11):2605-9. doi: 10.1099/0022-1317-81-11-2605. PubMed PMID: 11038370.

131. Ruiz M, Stahlman M, Boren J, Pilon M. AdipoR1 and AdipoR2 maintain membrane fluidity in most human cell types and independently of adiponectin. J Lipid Res. 2019;60(5):995-1004. Epub 20190319. doi: 10.1194/jlr.M092494. PubMed PMID: 30890562; PMCID: PMC6495173.